RBC 2012

Relax-Be snooping-Carpe diem
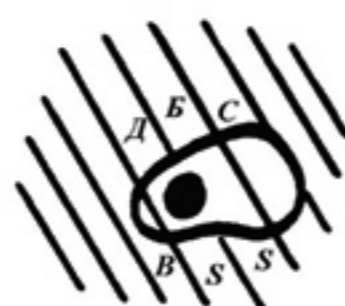
Regional Biophysics Conference 2012
Kladovo-Belgrade, Serbia
September 03-07, 2012

PROCEEDINGS

Organized by Biophysical Society of Serbia

EBSA
Biophysics in Europe

IUPAB
CONNECTING THE
WORLD OF BIOPHYSICS

ESN
EUROPEAN SOCIETY FOR
NEUROCHEMISTRY

CMJ
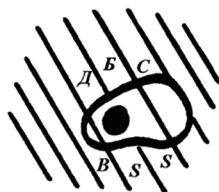CROATIAN MEDICAL JOURNAL

Relax-Be snooping-Carpe diem

Regional Biophysics Conference 2012
Kladovo-Belgrade, Serbia
September 03-07, 2012

PROCEEDINGS

Organized by Biophysical Society of Serbia

European Biophysical Societies' Association (EBSA)

International Union for Pure and Applied Biophysics

Ministry of Education and Science, Serbia

European Society for Neurochemistry

Croatian Medical Journal

RBC 2012 Principal organizer
Biophysical Society of Serbia

President:
Professor Pavle Andjus, Institute of Physiology and Biochemistry, Faculty of Biology, University of Belgrade

Secretary
Dr Miroslav Živić, Institute of Physiology and Biochemistry, Faculty of Biology, University of Belgrade

Steering Committee
Dr Pavle Andjus
Dr Miroslav Živić
Dr Ksenija Radotić, Institute for Multidisciplinary Research, Belgrade
Dr Joanna Zakrzewska, Institute of General and Physical Chemistry, Belgrade
Dr Miloš Mojović, Facuty of Physical Chemistry, University of Belgrade, Belgrade

RBC 2012 Organizing Committee
Pavle Andjus, Chair
Goran Bačić
Joanna Zakrzewska
Ksenija Radotić
Miroslav Živić
Miloš Mojović
Nataša Todorović
Ana Popović-Bjelić
Marina Stanić

RBC 2012 Scientific advisory board
Peter Pohl (Austia)
Georg Pabst (Austia)
Vesna Svetličić (Croatia)
Sanja Tomić (Croatia)
Laszlo Zimanyi (Hungary)
Péter Závodszky (Hungary)
László Mátyus (Hungary)
Mauro Dalla Serra (Italy)
Giorgio M. Giacometti (Italy)
Silvia Morante (Italy)
Pavle Andjus (Serbia)
Goran Bačić (Serbia)
Miroslav Zivić (Serbia)
Marjeta Šentjurc (Slovenia)
Janez Štrancar (Slovenia)
Milan Brumen (Slovenia)
Tibor Hianik (Slovakia)
Pavol Miskovsky (Slovakia)

The RBC is a series of biennial symposia intended to bring together biophysics researchers from Austria, Croatia, Hungary, Italy, Serbia, Slovenia and Slovakia and also includes internationally renowned guest speakers. The first such meeting took place in March 2005 in Terme Zrece, Slovenia. The language of the conference is English.

http://rbc2012.biofizikasrbija.com/

Table of contents:

3

4

MODELING OF ORGANIC BIOCOMPOUNDS

Stevan Armaković[1]
Sanja J. Armaković[2]
Igor J. Šetrajčić[1]
Jovan P. Šetrajčić[1,3]

[1] *University of Novi Sad, Faculty of Sciences, Department of Physics, Trg Dositeja Obradovića 4, 21000 Novi Sad, Vojvodina, Serbia,*
[2] *University of Novi Sad, Faculty of Sciences, Department of Chemistry, Biochemistry and Environmental Protection, Trg Dositeja Obradovića 3, 21000 Novi Sad, Vojvodina, Serbia,*
[3] *Academy of Sciences and Arts of Republic of Srpska, Bana Lazarevića 1, 78000 Banja Luka, Republic of Srpska, B&H.*

5

Abstract

In this paper we report the results of our research using computer modeling approach for organic compounds that are important for biophysical processes. Electronic subsystem responsible for a large range of properties of organic molecules and quantum structures of medium size can be explored on a computer in a relatively inexpensive level of theory using various available software packages, so allowing the use of relatively standard desktop computers. Among others, it is possible to calculate those quantities that are very sensitive to structural changes, such as NMR parameters, making them perfect for the purpose of comparing similar or in some way perturbed systems. Study presented here involves three well-known but not theoretically investigated enough, the active component of β-blockers: acebutolol, metoprolol and atenolol. Beside these, we also present results of boron disubstituted sumanene. Molecular bowl sumanene is model compound of fullerenes and nanotubes, synthesized in the last decade. Stability analysis and aromaticity calculations of active components of β-blockers confirmed their high stability and medium aromatic nature. Concerning boron disubstituted sumanene, quartic function of bowl depth does not only well describe the change of inversion barrier with bowl depth, but also describe well the change of nucleus independent chemical shifts with bowl depth.

Introduction

In this study we are showing how it is possible to use available software codes to confirm stability of investigated structures as well as to calculate important NMR parameters, such as chemical shielding and chemical shifts. In our work we investigated active components of three well known β-blockers: metoprolol, acebutolol and atenolol. The stability of the mentioned structures was tested in the photo-degradation processes with or without the presence of catalysts with proposed some possible intermediers [1]. Main results of research we conducted for these structures were published in [2]. Lately, we used similar approach to investigate isomers of sumanene where two carbon atoms were substituted by two boron atoms.

Material and methods

For geometry optimizations of active components of β-blockers we used Hartree-Fock (HF) method with 6-31G(d) basis set. The structures are optimized by implementation of the WinGamess code, revision 09 [3]. NMR parameters, chemical shift and chemical shielding, were calculated within GIAO method at the same level of theory.

For boron disubstituted sumanene Density functional theory calculations were performed by means of the hybrid, non-local exchange and correlation functional of Becke-Lee, Parr and Yang (B3LYP). For all calculations concerning boron disubstituted sumanene we used Gaussian 03 [4].

Section S1: Molecular biophysics

Results and discussion

Data on the HOMO and LUMO* energies came with the geometrical optimization. Obtained HOMO-LUMO energies were used to calculate stability – HOMO-LUMO gap, and within Koopmans theorem, chemical hardness, . In Fig. 1 are given values of parameters that describe stability and reactivity.
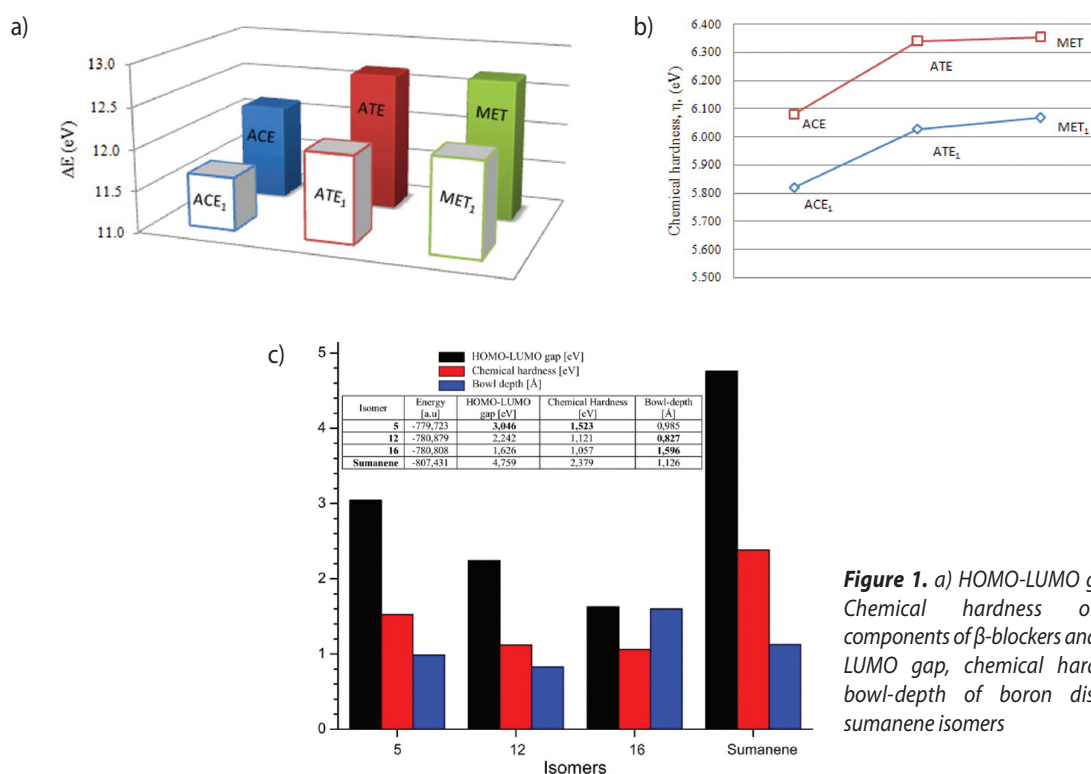
Figure 1. a) HOMO-LUMO gap and b) Chemical hardness of active components of β-blockers and c) HOMO-LUMO gap, chemical hardness and bowl-depth of boron disubstituted sumanene isomers

In Fig. 1, ACE1, ATE1 and MET1 indicate degradation products of mentioned structures as indicated on Scheme 1. These parameters are important as a measure of stability and sensitivity of organic compounds and for predicting reactivity or sensitivity in the general case.

Chemical hardness has been used as an electronic property to characterize the relative stability of molecules. Hardness is interpreted as the resistance toward change in number of electrons. According to the principle of maximum hardness, the hardness of a system becomes maximal at equilibrium geometries, and the stability is directly related to the higher values of hardness. Obtained results concerning chemical hardness are given in the insert of Fig. 1c (table).

According to molecular electrostatic potential we were able to suggest initial degradation products of investigated structures, Scheme 1.

Scheme 1.
Initial degradation products and NICS values
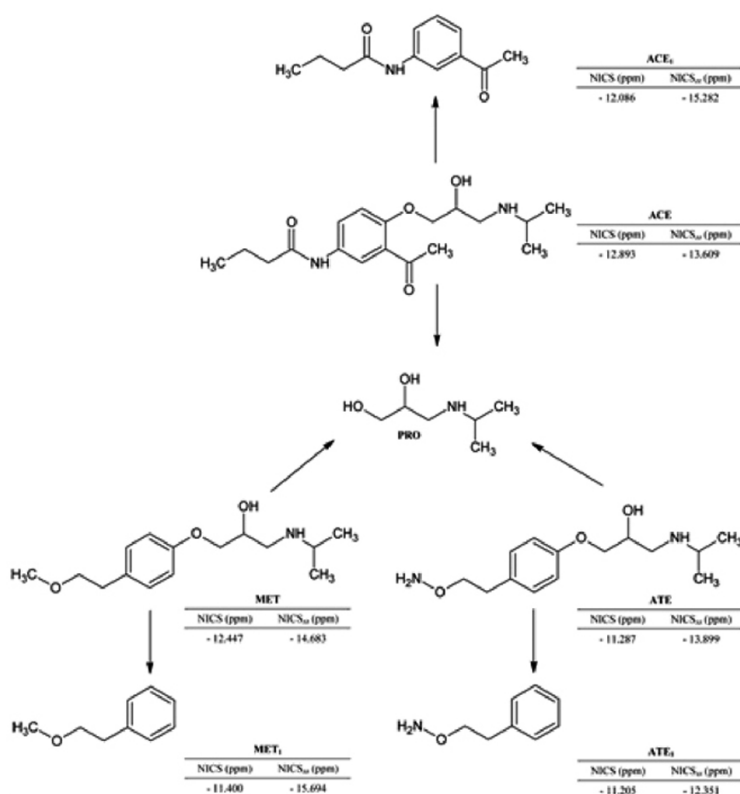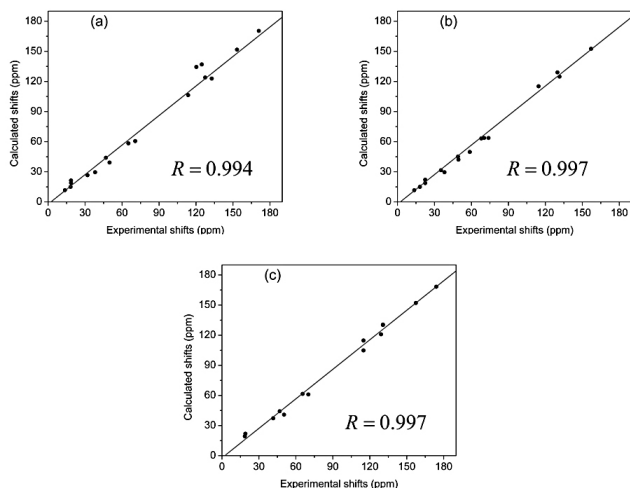
Figure 3. *Correlation of experimental and theoretical CS parameters. a) Acebutolol, b) Metoprolol and c) Atenolol. R is correlation coefficient*
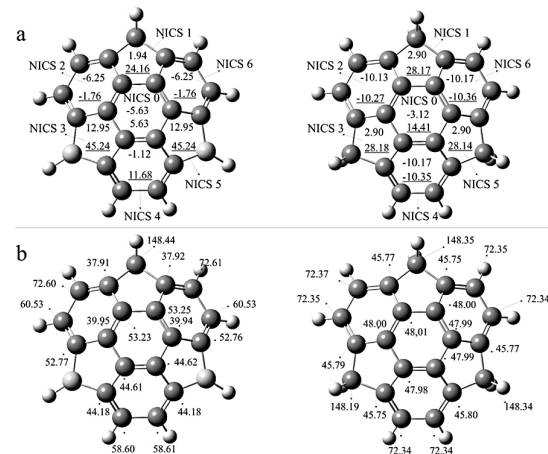
Figure 4. *Chemical shielding of isomer 5 compared with regular sumanene a) NICS and NICSzz (underlined), b) Chemical shielding*

NICS[**] are very important parameters because they are closely related to the energetic, structural and magnetic properties of molecules.

In Fig. 3 are presented results concerning correlation between calculated and experimental chemical shifts (CS) of active components of β-blockers. There is strong evidence that used level of theory is adequate for calculation of nmr parameters.

The same approach, but on higher level of theory was used for calculation of NMR parameters for investigated isomers of boron disubstituted sumanenes. In Fig. 4, results for the most stable isomer concerning chemical shielding and NICS are given.

7

Conclusions

Obtained results for stability, aromaticity and spectroscopic data indicate that HF/6-31Gd level of theory is valid for investigation of middle sized organic molecules such as active components of β-blockers. On the other hand, results obtained for the bowl to bowl inversion barrier of sumanene, indicate that DFT/6-31Gd level of theory is valid for investigation of relatively smaller molecular bowl-like systems.

Acknowledgment

References

1. Abramović B, Kler S, Šojić D, Laušević M, Radović T, Vione D. 2011, J Hazard Mater 198:123–132.
2. Armaković S., Armaković S. J., Šetrajčić J. P., Šetrajčić I. J., 2012, J Mol Model, article in press
3. Schmidt MW, et al (1993) GAMESS VERSION = 12 JAN 2009 (R3). J Comput Chem 14:1347–1363.
4. Frisch MJ, et al (2004) Gaussian, Inc., Wallingford CT.

_____

*   HOMO and LUMO highest occupied molecular orbital and lowest unoccupied molecular orbital

** NICS Nucleus-independent chemical shift

EPITOPE LOCATION IN ORDERED AND DISORDERED STRUCTURAL REGIONS OF TUMOR-ASSOCIATED ANTIGEN EBNA 1

Mirjana D. Pavlović[1]
Davorka R. Jandrlić[2]
Jovana B. Simić-Krstić[2]
Nenad S. Mitić[3]

[1] Institute of General and Physical Chemistry, University of Belgrade Studentski trg 12/V, Belgrade, Serbia
[2] University of Belgrade, Faculty of Mechanical Engineering, Kraljice Marije 16, Belgrade, Serbia
    University of Belgrade, Faculty of Mathematics, Studentski trg 16/IV, Belgrade, Serbia

Abstract

Epstein-Barr virus (EBV) nuclear antigen 1 (EBNA 1) is expressed in latency I, II and III states of EBV-associated cancers and is possibly associated with autoimmune diseases. Predicted and experimentally determined promiscuous HLA-II-binding and CD4+ T cell-inducing epitopes are located in the structured (ordered) part of the EBNA 1 antigen (residues 475-552), while nonimmunogenic part 403-428 appartains to the disordered region and is a potential molecular recognition element. As B-cell epitope 398-404, on the borderline of the region 403-428, was found to elicit a lupus like disease in rabbits, it could be speculated that this epitope possibly elicit autoimmune process and epitope spreading through its involvement in a molecular complex.

Introduction

The overexpression in cancer and spontaneous immune response demonstrated against certain tumor-associated antigens (TAA), imply that they are possible targets for vaccine trials and they are also often found to contain long disordered protein regions (1). Epstein-Barr virus (EBV)-associated malignancies involve the latent cycle and can be distinguished by the patterns of latent viral gene expression. EBV nuclear antigen 1 (EBNA 1) is expressed in latency I, II and III states of EBV-associated cancers (2) and is possibly associated with autoimmune diseases (3).

Material and methods

For epitope prediction NetMHCPan-2.0 (4) and NetMHCiiPan-1.0 (5) methods were used. For predicting disordered regions VSL2 (6), PONDR VL-XT (7) and PONDR- FIT (8) were applied. The Kyte-Doolittle hydrophobicity scale (9) was applied for prediction of hydropathy profile. We have developed EPDIS (EPitope in DISorder) application (presented in Fig. 1.), which integrates all of the mentioned methods and offers graphical interface. We also have used ANCHOR program which predicts binding regions located in disordered proteins. ANCHOR seeks to identify segments in a generally disordered region that cannot form enough favorable intrachain interactions, but have the capability to energetically gain by interacting with a globular partner protein (10).

Results and discussion

CD4+ T cells against promiscuous immunodominant HLA-II epitopes, localized in the EBNA 1 region 475-552 (2), have been generated, but not against epitopes in the region 403-428, predicted and evaluated as immunologically subdominant for 12 DRB alleles (2), as presented for DRB1_0101, Fig.1 C. Region 475-552 is a part of the structured (ordered) domain, while region 403-428 appertains to the potential disorder-to-order transition element (identified in a PONDR VL-XT prediction score as a short, well pronounced dip, Fig. 1 A), and as molecular binding site (according to ANCHOR predictor, data
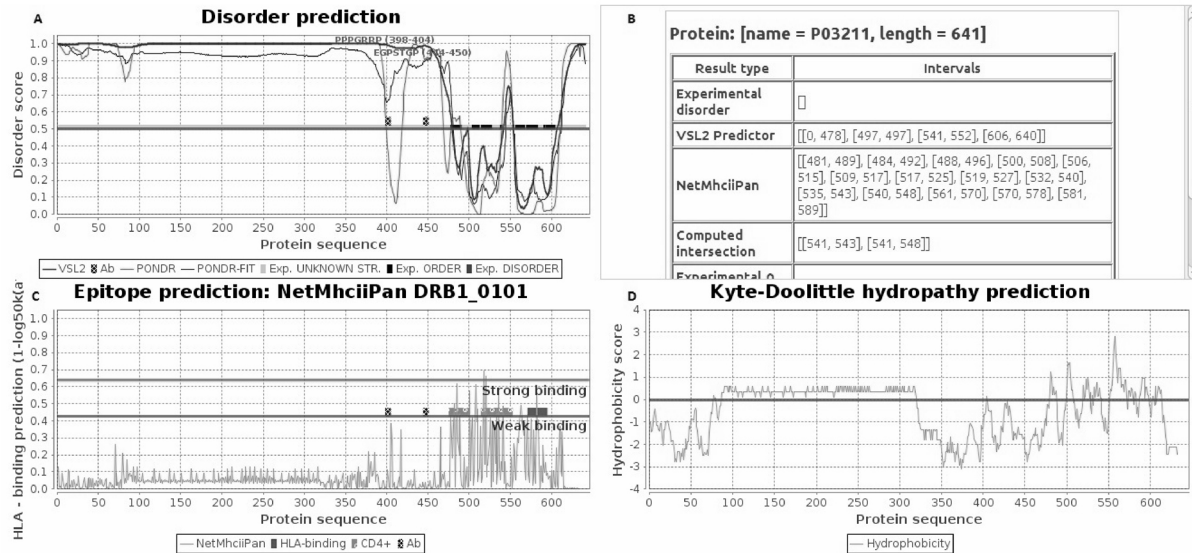
Figure 1. *Epstein-barr virus protein EBNA 1 (UniProt Acc No: P03211). The application displays data on A: disorder prediction, obtained using VSL-2B, PONDR-VL-XT and PONDR-FIT predictors. Secondary structure prediction is from (http://www.uniprot.org/). B: predicted: disorder regions and epitopes, experimental results and intersections. C: HLA-II nonamer epitope prediction, using NetMHCIIPan method. Epitopes: 475-500, 514-539, 529-552 and 571-594 were determined as high-affinity HLA-DRB1*0101 binding ( ) and/or CD4+ T cells-inducing ( ) (2). Epitopes: 398-404 (3) and 444-450 (11) were experimentally determined as antibody-binding ( ). D: Kyte-Doolittle hydropathy plot of a protein sequence, using a window of nine amino acids.*

not shown). The boundaries of the prevalently hydrophilic region 403-428, are recognized by antibodies (Ab), Fig. 1A/C/D. Epitope 444-450 (EGPST**G**P) of EBNA1 (11), Fig. 1. A/C is recognized by a mouse monoclonal Ab 2B4. This Ab also interacts with homologous peptide 94-100 (EGPST**S**P), located in the disorder-to-order transition element of MAGE-A4 cancer/testis antigen, similar to that of EBNA 1, Fig. 2. A/C. Epitope 398-404 (PPPGRPP) of EBNA 1 was found to elicit a lupus like disease in rabbits (3), which is of great interest since the authors cite that EBV may be an etiological agent of lupus autoimmunity. EBV infections might lead to an autoimmune response caused by mimicry of peptide PPPG**M**RPP (repeated within the carboxyl terminus of Sm B/B' autoantigen) with epitope PPPGRPP of EBNA 1. The response is initially directed against sequence PPPG**M**RPP in Sm B/B' protein,

Figure 2. *Human MAGE-A4 protein (UniProt Acc No: P43358.1) A: Disorder/order prediction, obtained using VSL2B, PONDR VL-XT and PONDR-FIT predictors; B: predicted: disorder regions and epitopes, experimental results and intersections. C: HLA-II nonamer epitope prediction, using NetMHCiiPan methods for the HLA DRB*1401 allele. Epitopes (280-299 and 284-293), were experimentally determined as weak-affinity HLA DRB1*1403 binding and CD4+, Th1 cells-inducing ( ). Epitope 94-100 was ( ) detected by monoclonal antibody 2B4, directed against EBNA1 antigen from Epstein-Barr virus (11). D: Kyte-Doolittle hydropathy plot of a protein sequence, using a window of nine amino acids.*

followed by the secondary determinans in the Sm particle. Based on Sm B/B' and several other nuclear systemic autoantigens, Carl et al. hypothesized (12) that epitope spreading, a common mechanism in autoimmunity, initiates with antibodies directed against epitopes in ordered regions of antigen and then moves towards epitopes in disordered regions of the same or different antigen, which are not cross-reactive with the initiating peptide. It was suggested that participation in a molecular complex could be one of the main causes of autoantigenicity.

If residues 403-428 of EBNA1 happen to be the part of molecular-binding region, peptide 398-404, could be an epitope, possibly involved in a molecular complex and structurally available (or disavailable) upon ligand-binding, which may influence its antigenicity.

Acknowledgements

10

References

1. Iakoucheva, L. M., Brown, C. J., Lawson, J. D., Obradovic, Z. and Dunker, A. K. et al., 2002, J. Mol. Biol., 323: 573-584.
2. Depil, S., Moralès, O., Castelli, F. A., Delhem, N., François, V., Georges B., Dufossé F, Morschhauser F, Hammer J, Maillère B, Auriault C, Pancré, 2007, V. J. Immunother., 30: 215-226
3. James J. A., Scofield, R. H., Harley J. B., 1997, Ann N Y Acad Sci, 815:124-127.
4. NetMhcPan program: http://www.cbs.dtu.dk/services/NetMHCpan
5. NetMhcIIPan program: http://www.cbs.dtu.dk/services/NetMHCIIpan-1.0
6. VSL2 predictor: http://www.ist.temple.edu/disprot/predictorVSL2.php
7. PONDR VL-XT predictor: http://www.pondr.com
8. PONDR-FIT predictor: http://www.disprot.org/pondr-fit.php
9. Kyte, J., Doolittle, R., J. Mol. Biol., 1982, 157: 105-132.
10. ANCHOR, Meszaros, B., Simon., I., Dosztanyi, Y., 2009, PLOS comp. biol., 5, e1000376.
11. Hennard, C., Pfuhl, T., Buettner, M., Becker, K.-F., Knofel, T., Middeldorp, J., Kremmer, E., Niedobitek, G., Grasser, F. A., 2006, J. Pathol. 209: 430–435.
12. Carl, P. L., Temple, B. R. S. and Cohen, P. L., 2005, Arthritis Res & Ther., 7 (6): R1360-R1374

T-CELL EPITOPE CLUSTERING IN DIFFERENT STRUCTURAL REGIONS OF CANCER/TESTIS ANTIGEN PROTEINS

Nenad S. Mitić[1]
Mirjana D. Pavlović[2]
Davorka R. Jandrlić[3]
Saša N. Malkov[1]

[1] University of Belgrade, Faculty of Mathematics, Studentski trg 16/IV, Belgrade, Serbia
[2] Institute of General and Physical Chemistry, University of Belgrade, Studentski trg 12/V, Belgrade, Serbia
[3] University of Belgrade, Faculty of Mechanical Engineering, Kraljice Marije 16, Belgrade, Serbia

P R O C E E D I N G S

Abstract

T-cell epitope predictions of Human Leukocyte Antigens class I and class II (HLA-I, HLA-II)- binding epitopes, revealed that epitopes, binding to alleles of both HLA-I and HLA-II class, were more frequent in ordered than in disordered regions of 642 proteins from various taxonomic groups. Epitopes belonging to ordered protein regions were also found to be prevalently hydrophobic. The comparison between predicted and experimentally evaluated epitopes of 10 immunogenic cancer/testis antigens (CTA), revealed that majority of epitopes, presented by different HLA-I and HLA-II alleles, are localized in ordered protein regions.

11

Introduction

Cancer/testis antigens (CTA) were found to contain long unstructured (disordered) regions (1). CTA are potential cancer-vaccines candidates, because of their aberrant expression in several types of cancer, while normal expression is restricted to testicular germ cells, which do not express HLA-I antigens. Some of CTA are also normally found in ovary and placenta. The localization of T-cell epitopes in the antigen 3D structure may influence their processing and presentation (2) or immunogenicity of potential epitope could depend only of its amino acid content (3). We have compared epitope frequency, affinity of binding to HLA class I or class II alleles and epitope hydrophobicity within predicted ordered and disordered protein regions. The data on predicted and experimentally found epitope localization and immunodominant CD4+ or CD8+ response, reported for several CTA, were compared.

Experimental

Database contained 642 proteins, mainly (477) from DisProt database (4). For HLA-I or HLA-II epitope prediction, NetMHCpan-2.0 (5) and NetMHCIIpan-1.0 (6) methods were used. For predicting disordered regions VSL2 (7), PONDR VL-XT (8) and PONDR-FIT (4) were applied. The Kyte-Doolitle hydrophobicity scale (9) was applied for prediction of hydropathy profile. We have developed EPDIS (EPItope in DISorder) application (Fig. 1), which integrates all of the mentioned methods and offers graphical interface.

Results and discussion

The number of nonamer epitopes in ordered protein regions was 2.84 times higher than in disordered regions for HLA-I alleles and 3.60 times higher for HLA-II alleles. The same trend, (order/disorder ratio: 2.64 for HLA-I and 3.34 for HLA-II alleles), remains after normalization of epitope number on 100 AA (epitope frequency), as presented in Table 1.
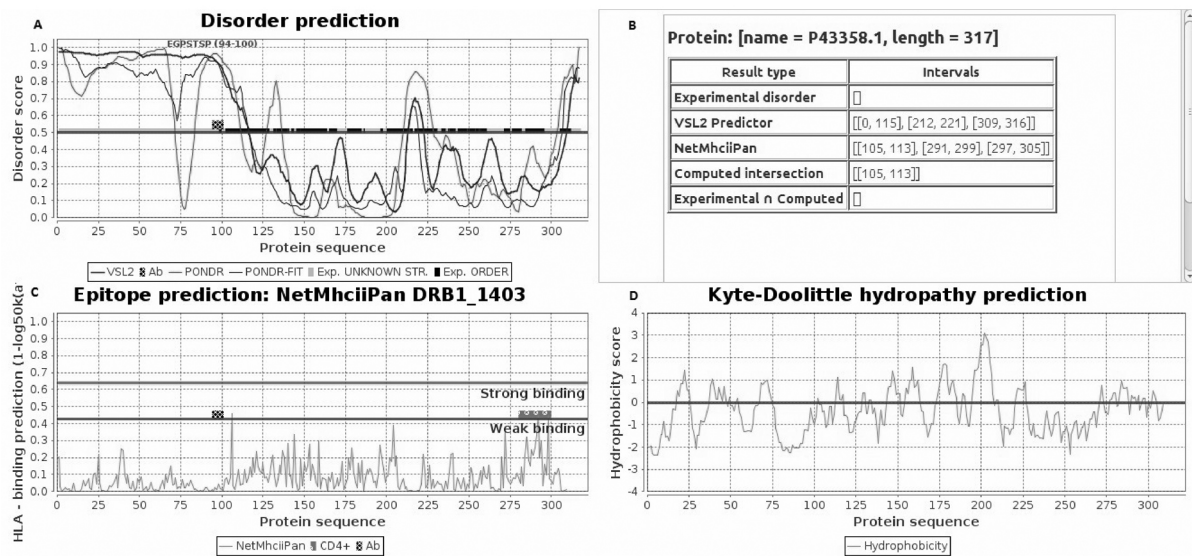
Section S1: Molecular biophysics
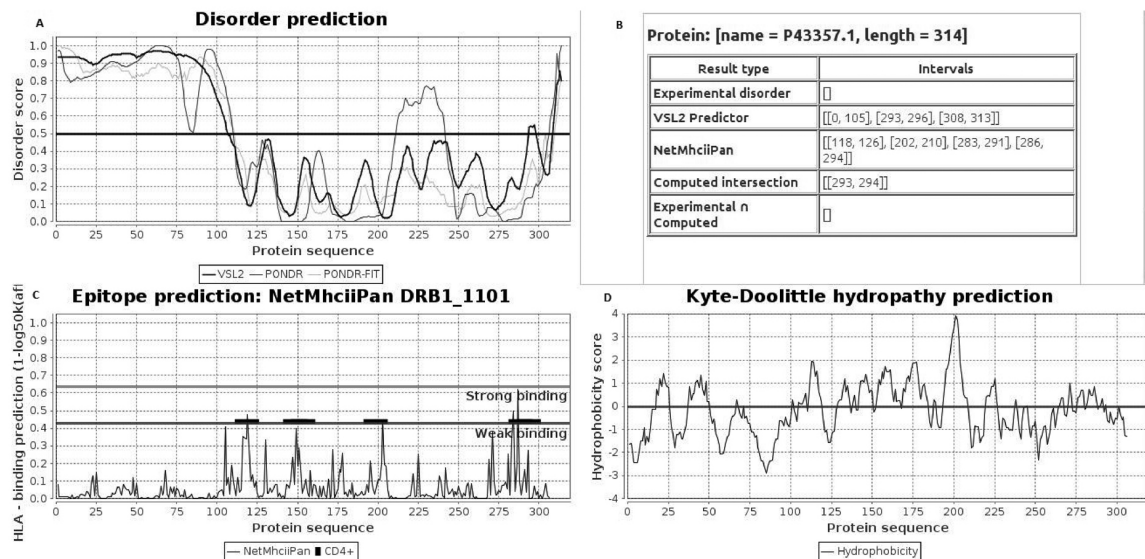
Figure 1. *Human MAGE-A3 protein (UniProt Acc No: P43357.1). A: disorder/order prediction, according to VSL-2B, PONDR-VL-XT and PONDR-FIT predictors. B: predicted: disorder regions and epitopes, experimental results and intersections. C: HLA-II nonamer epitope prediction, using NetMHCpan method for HLA-DRB1*1101 allele. Epitopes, designated as (▮), were experimentally found to induce CD4+ T cells. D: Kyte-Doolitle hydopathy plot of protein sequence, using a window of nine amino acids.*

HLA	Region type	HLA binding level	Epitopes/ 100 AA	HER*
HLA1	D	SB	88.38	Hydrophilic
		WB	398.19	Hydrophilic
	N	SB	91.05	Hydrophilic
		WB	406.17	Hydrophilic
	O	SB	266.1	Hydrophobic
		WB	1017.83	Hydrophobic
HLA2	D	SB	11.68	Hydrophobic
		WB	201.81	Hydrophilic
	N	SB	15.11	Hydrophobic
		WB	241.02	Hydrophobic
	O	SB	44.04	Hydrophobic
		WB	668.77	Hydrophobic

* If the number of hydrophobic epitopes in region is over 50%, the HER is considered as hydrophobic, otherwise as hydrophilic.

Table 1. *Number of week (WB)- and strong (SB)-binding epitopes/100 AA (epitope frequency) and hydropathy of epitopes in regions (HER) in disorder (D), ordered (O) and disordered/ordered-boundary regions (N) for HLA-I and HLA-II class alleles.*

The same conclusion holds when proteins were grouped according to main taxonomic categories (archaea, bacteria, eukarya, and viridae) (data not shown). It is evident from Table 1 that epitopes, belonging to ordered protein regions are always prevalently hydrophobic (for both HLA-I and HLA-II alleles). The results are in accordance with HLA-I supertype binding motifs (10) and hydrophobic N-terminal positions of the HLA-II class binding peptides (11). Epitope frequency in ordered and disordered protein regions was analysed in 19 immunogenic CTA, mostly from MAGE-A, NY-ESO and SSX families that have been previously studied for cellular immune response (12). Majority of predicted epitopes, presented by HLA-I and HLA-II molecules, are localized in ordered protein regions. In long disordered protein sequences epitopes are frequently flanking potential disorder-to-order

transition elements. These results were found to correspond with the localization of experimentally determined epitopes of 10 CTA, for which sufficient experimental data were found. Experimentally evaluated epitopes were presented by different HLA-I and HLA-II alleles. For example, the CD4+ response to naturally processed HLA-II-presented epitopes from cancer/testis antigen MAGE-A3 was found to be promiscuous for several DRB1 alleles (13), and localized in the central, ordered region of MAGE-A3 antigen, comprising amino acids 107-293, as presented for HLA-DRB1*1101 allele, Fig. 1.

Conclusion

Using disorder and epitope predictions we have found that both HLA-I and HLA-II epitopes were more frequent in ordered than in disordered regions of 642 proteins. Predicted epitopes were correlated with experimentally found ones in several cancer/testis anigens, which may be helpful in mapping potential cancer-vaccine candidate peptides.

Acknowledgements

References

1. Rajagopalan K., Mooney S. M, Parekh., N., Getzenberg R. H., Kulkarni P. A., J. Cell. Biochem. 2011, 112:3256–3267.
2. Carmicle S., Steede N. K., Landry S. J., Mol. Immunol., 2007, 44:1159–1168.
3. Weaver J. M., Lazarski C. A., Richards K. A., Chaves F. A., Jenks S. A., Menges P. R., Sant A. J., J. Immunol. 2008, 181(5):3039-48.
4. Disprot database: http://www.disprot.org
5. NetMhcPan program: http://www.cbs.dtu.dk/services/NetMHCpan
6. NetMhciiPan program: http://www.cbs.dtu.dk/services/NetMHCIIpan-1.0
7. VSL2 and PONDR-FIT predictors: http://www.disprot.org/predictors.php
8. PONDR VL-XT predictors: http://www.pondr.com
9. Kyte J., Doolittle, R., J. Mol. Biol., 1982, 157:105-132.
10. Sidney, J., Peters, B., Frahm, N., Brander, C., Sette, A., BMC Immunol., 2008, 22: 9:1.
11. Halling-Brown, M., Shaban R., Framton D., Sansom C. E., Davies M., Flower D., Dufflied M., Titball R. W., Brusic V., Moss D. S., Mol. Immunol., 2009, 46:2699-2705.
12. http//www.cancerimmunity.org/peptidedatabase/tumorspecific.htm
13. Consogno G., Manici S., Facchinetti V., Bachi A., Hammer J., Conti-Fine B.-M., Rugarli C., Traversari C., Protti M. P., Blood, 2003, 101:1038-44.

APPLICATION OF FIXED SIZE WINDOW FACTOR ANALYSIS (FSW-FA) IN PROCESSING FLUORESCENCE SPECTRA OF BIOACTIVE EXTRACTS

Boris Pejin[1][*]
Predrag Conić[2]
Aleksandar Savić[1]
Yong Kien-Thai[3]
Aleksandar Hegediš[1]
Ivo Karaman[4]
Mladen Horvatović[4]
Ksenija Radotić[1][**]

[1] *Department of Life Sciences, Institute for Multidisciplinary Research, University of Belgrade, Serbia*

[2] *Faculty of Physical Chemistry, University of Belgrade, Serbia*

[3] *Institute of Biological Sciences, Faculty of Science, University of Malaya, Malaysia*

[4] *Department of Biology and Ecology, Faculty of Science, University of Novi Sad, Serbia*

[*] *brspjn@gmail.com*

[**] *xenia@imsi.rs*

Abstract

As part of our ongoing study on the chemistry of the moss *Rhodobryum ontariense* and the bryozoan *Hyalinella punctata* intended to be applied in pharmacy, the fluorescent components of their bioactive extracts were preliminary screened by spectrofluorimetry and statistically analysed by fixed size window factor analysis (FSW-FA). This method has shown to be an elegant tool for rapid screening of differences among various samples, in particular for observing of different fluorophores in biologically important samples.

Introduction

Pejin *et al.* have recently investigated biological activity of the moss *Rhodobryum ontariense* and the bryozoan *Hyalinella punctata* for the first time. It has been found that systolic, diastolic and mean arterial pressure as well as cardiac output are significantly lowered in the group of spontaneously hypertensive rats (n=7) treated intravenously with *R. ontariense* lyophilised water extract (100 mg/kg b.w. dissolved in 0.2 ml of saline) [1]. On the other hand, *H. punctata* methanolic extract expresses a potent cytotoxic activity (IC_{50} value 24.13 μg/ml) against the tumor cell line MCF-7 [2]. The methanolic extract of *R. ontariense* and the water extract of *H. punctata* have also shown promising properties such as antimicrobial and radioprotective activity, respectively. The aim of this study was to aply fluorescence spectroscopy combined with statistical spectral analysis (FSW-FA) for rapid preliminary screening of different fluorophores in the aforementioned bioactive extracts.

Material and methods

The sample of *R. ontariense* originated from the Fraser's Hill (Malaysia, August 2011). Air-dried parts of *R. ontariense* (2 g) were ground and extracted thrice with methanol and hot water for 30 min at room temperature, respectively. The extracts were filtered and concentrated by lyophilisation to give the residues which was stored at -20 °C for further use. The colonies of the freshwater bryozoan *Hyalinella punctata* (Hancock, 1850) were collected in Belgrade (the river Danube, Serbia) in November 2011. After careful cleaning from contaminants, the bryozoan sample was lyophilised. The dried parts of *H. punctata* were ground (2g) and extracted thrice with methanol and hot water for 30min at room temperature, respectively. The extracts were evaporated to dryness and stored at - 20⁰C until further use.

Fluorescence spectra were collected using a Fluorolog-3 spectrofluorimeter (Jobin Yvon Horiba, Paris, France) equipped with a 450 W xenon lamp and a photomultiplier tube. The 1-cm optical path length quartz cuvette was used. The slits on the excitation and emission beams were fixed at 5nm each. The spectra were corrected for dark counts. In each measurement, five scans with 0.1 second-integration time, were averaged. The extracts were dissolved either in methanol or deionised water for measurements. The emission spectrum of the solvent (water or methanol) was subtracted. All measurements were performed at controlled temperature of + 25ºC by means of a Peltier element. For each a series of emission spectra were measured by varying excitation wavelengths with 10 nm steps. In order to include all geometric characteristics of an emission spectrum into modeling, initial excitation wavelength was set in such a way that recording of emission spectra started 30 - 40 nm before the sharp rise in emission [3].

Decomposition of the series of emission spectra for each of the samples was performed using fix size window factor analysis (FSW-FA) [4]. As a result of the analysis, the total number of components in an integral spectrum was obtained.

Results and Discussion

The excitation-emission matrix for the analyzed sample is shown in Fig. 1.
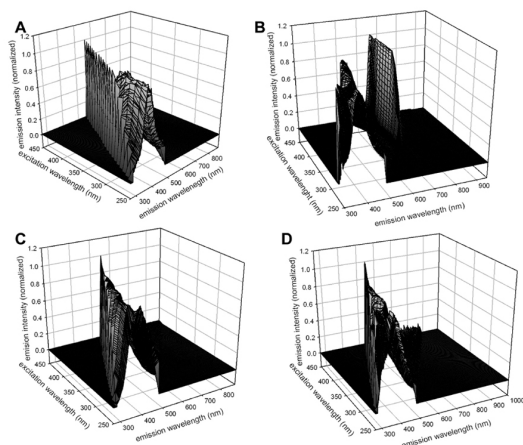
Figure 1. Excitation-emission matrix of the emission spectra (Figure 2) of A (water extract of R. ontariense), B (methanolic extract of R. ontariense), C (water extract of H. punctata), and D (methanolic extract of H. punctata)

Objective of factor analysis is to decompose matrix **A** to source matrix **S** which contains extracted components (fluorophores) and **C** the matrix of coefficients of linear combinations (**A=SC**). Since the emission spectra were recorded by increment of excitation wavelength of 10 nm, fixed size window factor analysis (FSW-FA) was applied, and two factors were extracted in each pass. Overlapping factors were excluded from the further analysis. The analysis of the emission spectra has shown 13 and 15 components in the spectra of water and methanolic extracts, respectively, of the moss; the 12 and 15 components have been found in the spectra of water and methanolic extracts, respectively, of the bryozoan species (Fig. 2).
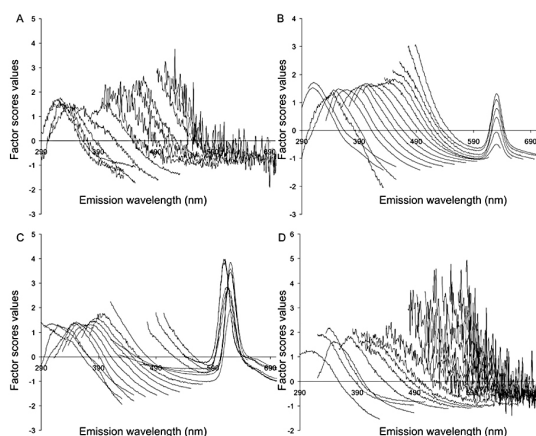
Figure 2. the spectral components of the emission spectra (Figure 2) of A (water extract of R. ontariense), B (methanolic extract of R. ontariense), C (water extract of H. punctata), and D (methanolic extract of H. punctata)

Section S1: Molecular biophysics

The results indicate that combination of fluorescent spectroscopy and appropriate statistical analysis of the spectra can be used as a tool for rapid and economic method for preliminary screening of various biological samples, such as bioactive extracts and their fractions [5]. Indeed, such results may be used as an input for further more detailed studies by other methods (e.g. LC-MS).

16

References

1. B. Pejin, S. Newmaster, M. Sabovljevic, Z. Miloradovic, J. Grujic-Milanovic, M. Ivanov, N. Mihailovic Stanojevic, Dj. Jovovic, V. Tesevic, V. Vajs, J. Hypertens., 2011, 29, e315.
2. B. Pejin, S. Stosic-Grujicic, G. Bogdanovic, A. Hegedis, I. Karaman, I. Stojanovic, I. Nikolic, V. Kojic, M. Horvatovic, K. Radotic, Dig. J. Nanomater. Bios., 2012, submitted.
3. A. Kalauzi, D. Mutavdžić, D. Djikanović, K. Radotić, M. Jeremić, J. Fluoresc., 2007, 17, 319-329.
4. S. Šašić, A. Antić-Jovanović, M. Kuzmanović, M. Jeremić, Analyst, 1999, 124, 1481-1487.
5. D. Mutavdžić, J. Xu, G. Thakur, R. Triulzi, S. Kasas, M. Jeremić, R. Leblanc, K. Radotić, Analyst, 2011, 136, 2391-2396.

EXPRESSION OF PROTEIN A – BETA-LACTAMASE FUSION PROTEIN FOR DETECTION OF BIVALENT ANTI-TNT ANTIBODIES

Mladen Simonović
Aleksandra Radulović
Spasenka Gajinov
Stanislava Gorjanović
Branislav R. Simonović

Institute of General and Physical Chemistry, University of Belgrade, Belgrade, Serbia

Abstract

For detection of bivalent antibodies a fusion protein of protein A and beta-lactamase was constructed and expressed. The performing of immunoassays was based on the immobilizing of immunoglobulines on the solid surface to verify the specificity of detection reagents and sensitivity of enzyme.

Introduction

All immunoassays need an amplifying system for detection of signal in the current immunoreaction. This system allows the qualitative or quantitative analysis of the component of interest. The commonly used amplifiers are enzymes, which enhance the sensitivity of reaction by converting their substrates into detectable products. In this work, the fusion protein proteinA-beta lactamase was used as an amplifying system with optical detection of signal. The enzyme beta lactamase was chosen because it consists of only one peptide chain and is relatively small (263 aminoacids, 29 kDa). As substrate for beta lactamase nitrocephin was used (1).

17

Material and methods

Standard molecular biology techniques: PCR, ligation, restriction, DNA dephosphorylation, agarose gel-electrophoresis, DNA extraction from agarose gels, classic plasmid preparation, alcohol precipitation, DNA quantification, etc. were done according to the standard protocols (2).

Standard techniques in protein biochemistry: PAGE, protein determination, Western blot, IMAC (immobilized metalion affinity chromatography) etc. were generally done according to the standard protocols (2).

ELISA: The 96-wells plate was covered over night at 4°C with a strong diluted mixture of IgG (50 µg/ml). As negative control in each assay the wells were covered with BSA. After the washing procedure (three times both with cold PBS and TPBS) the wells were blocked with BSA for 45 min at room temperature. After identical washing process the fusion protein ProteinA-beta-lactamase in the concentration of 10-60 µg/ml was incubated for 1 h at the room temperature on a rocker platform. After the same washing process nitrocephin was added for detection and incubated for 5 minutes at room temperature on a rocker platform. The signal was measured in the ELISA-reader at 492 nm. Two alternative assays were done as described in Results.

Results and Discussion

As a starting material for the cloning and procaryotic expression the vector pET26b(+) was chosen. The strategy was so planed, that the gene for proteinA (891 bp) should be cloned in front of beta-

lactamase. Behind beta-lactamase had to stay HisTag (for detection and purification) together with stop-codon. The insertion of genes for ProteinA and beta-lactamase was verified by PCR.

Expression was performed at 25°C and IPTG (Isopropyl β-D-1-thiogalactopyranoside) concentration of 0.5 mM. The presence of the protein was verified in both periplasmic and cell extract using immunoblot (Fig. 1). After purification from dialysed periplasmic extract using NiNTA matrix, the fusion protein of 62 kDa was analysed in SDS-PAGE.
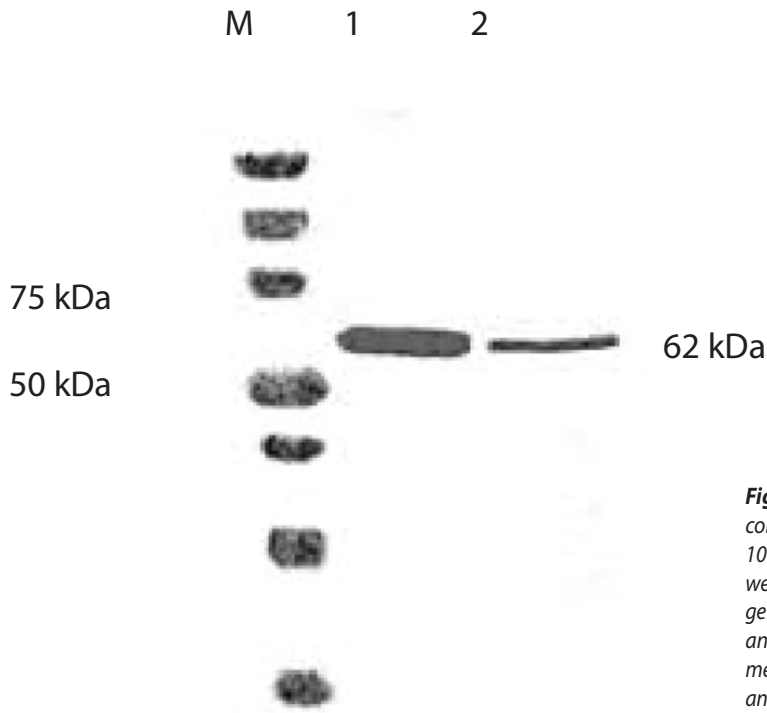
Figure 1. Analysis of periplasmic and cell extract containing the fusion protein proteinA-beta-lactamase. 10 μl of protein marker (M) and 15 μl of protein probe were separated under reducing conditions on 12%-SDS gel. The presence of the protein was verified in the cell (1) and periplasmic (2) extract after transferring on PVDF-membrane in immunoblot using detection with murine anti-His-IgG (1:2500) and anti-mouse-IgG-AP conjugate (1:2500).

Enzymatic activity of this fusion construct was visually identified in the purified form (60 μg/ml) using the substrate nitrocephin. In order to prove its functionality as immunoglobuline binding and detecting reagent three types of ELISA were done all with a mixture of IgG molecules as covering agents. In the first ELISA, detection of IgGs was made with nitrocephin direct after 1 h incubation of proteinA-beta-lactamase. In the second one, after 1 h incubation of proteinA-beta-lactamase two more incubation steps were performed: with anti-his antibodies as the primary and anti-mouse-IgG-HRP conjugate as the secondary antibody. The detection was done with a HRP substrate ABTS (2,2'-azino-bis(3-ethylbenzothiazoline-6-sulphonic acid)). And finally, in the third ELISA the additional incubation steps were done with the rabbit polyclonale anti-beta-lactamase serum (1° antibodies) and anti-rabbit-IgG-HRP conjugate (2° antibody). In none of three ELISA any signal was detected.

All three ELISA assays were repeated with anti-TNT-IgG antibodies (3) as covering agents under the same conditions in order to establish an assay for the detection of TNT-derivatives (4). Also here no measurable signal could be detected.

Conclusion

Immunoreagent proteinA-beta-lactamase was produced in periplasma in the moderate expression yield. The expression rate was 1 μg per ml of culture. During the characterization of this fusion protein in ELISA for detection of IgG-molecules the reactivity of beta-lactamase was not demonstrated because of its small sensitivity. Also, the performed ELISA were two and four component systems, where the dissociation of immunoreagents hanging on each other was strong favored and no binding stability could occur. The modification of this fusion protein could be done by introducing other enzymes instead of beta-lactamase, which have a larger turnover number, such as alkali phosphatase

or horseradish peroxidase. An alternative enhancement of sensitivity could be reached in the assay with the fluorescent substrate for beta-lactamase (5).

References

1. R. Guay et al, 1980. IRCS Med Sci., 8, 209.
2. Ausubel, F.M., 1996. Current protocols in molecular biology. Wiley Intersci., New York.
3. M. Simonovic, S. Milosevic-Zlatanovic, M. Vrvic, B. Simonovic, 2008, J. Serb. Chem. Soc., 73(2), 139-145.
4. M. Simonovic, S. Milosevic-Zlatanovic, N. Milosavic, M. Vrvic, B. Simonovic 2009, Chemical Papers, 63(4), 391-398.
5. Zlokarnik, G., Negulescu, P.A., Knapp, T.E., Mere, L., Burres, N., Feng, L., Whitney, M., Roemer, K., Tsein, R.Y., 1998. Science, 279, 84-88.

EFFECT OF HBO TREATMENT ON EXPRESSION OF SOD2 AFTER CORTICAL STAB INJURY IN RATS

Ana Parabucki[1]
Iva Bozic[1]
Mirjana Stojiljkovic[1]
Tomislav Jovanovic[2,3]
Irena Lavrnja[1]
Ivana Bjelobaba[1]
Danijela Savic[1]
Predrag Brkic[2]
Sanja Pekovic[1]

[1] Department of Neurobiology, Institute for Biological Research "Sinisa Stankovic", University of Belgrade, Serbia
[2] Institute of Medical Physiology "Richard Burian", School of Medicine, University of Belgrade, Serbia,
[3] Centre for Hyperbaric Medicine, Belgrade, Serbia
aparabucki@ibiss.bg.ac.rs

Abstract

Despite the amount of work that has been done in order to better understand traumatic brain injury (TBI), currently there is no effective treatment. Substantial amount of evidence has been published indicating that treatment with hyperbaric oxygen (HBOT) can interfere with the processes that are following TBI and modify its consequences. However, the exact mechanisms by which HBOT exerts its positive effects are still elusive. Since antioxidant enzymes are activated in response to TBI, the aim of the present study was to evaluate the effect of HBOT on superoxide dismutase 2 (SOD2) expression pattern after TBI. Based on the obtained results we have concluded that beneficial effects of HBOT on recovery after brain injury may be in part due to reduction of oxidative stress via restoring SOD2 expression to physiologic level.

Introduction

TBI is among the most disabling injuries and, therefore, represents major health problem worldwide. It involves primary and secondary injury. First one is due to mechanical damage and triggers a cascade of events known as secondary injury, which represents chronic disease process and main target for potential therapies (1). As a part of secondary cascade, oxidative stress, among other events, is a prominent one (2). It has been shown that reactive oxygen species (ROS), if exceed the capacity of the anti-oxidative defenses, lead to oxidative stress and cellular damage after brain trauma (3). First line of defense against ROS is in the place where it all begins - mitochondria. SOD2, located in the mitochondrial inner membrane and matrix, is a critical antioxidant enzyme that catalyzes the dismutation of superoxide radical to oxygen and hydrogen peroxide. In different brain pathologies, the induction of SOD2 varies and this depends on type of the injury (4). Furthermore, most data point out the neuroprotective role of SOD2 in brain injury (5).

Despite the amount of work that has been done in order to better understand TBI, it still lacks an adequate therapy. In the past decade HBOT became often used medical tool, and it appears to be a good therapeutic solution for a variety of conditions (6). HBOT is a therapeutic approach where the patient is exposed to 100% oxygen at pressures higher than ambient. This leads to an increased blood oxygen level, which than can penetrate to ischemic areas more deeply than under normobaric conditions (7).

Since definitive established mechanisms of HBOT action are still deficient we investigated the possibility that enhancement of antioxidative enzymes may underline the positive impact of HBOT on

recovery after TBI. Therefore, in the present study we examined the temporal effect of HBOT on gene and protein expression pattern of SOD2 after cortical stab injury (CSI) using Quantitative real-time PCR and Western blotting.

Material and methods

CSI was conducted on ten-weeks-old male Wistar rats as previously described (8). One hour after the surgery, some of the operated rats were exposed to 100% oxygen according to the following HBOT protocol (9): 10min compression, 2.5 atmospheres absolute (ATA), for 60min., 10 min. decompression, once daily for 3 or 10 days. Animals were randomly organized into following groups (n=5): control (C)- intact rats; control HBOT (C+O$_2$)- intact rats subjected to the HBOT protocol; sham group (S)- the animals that underwent surgical procedure without skull opening, sacrificed 3 and 10 days post injury (dpi); sham HBOT group (S+O$_2$)- the animals that underwent sham surgery and were subjected to the HBOT protocol; lesion group (L)- the animals that passed CSI and were sacrificed 3 or 10 dpi, and lesion HBO group (L+O$_2$) – CSI rats subjected to the HBO protocol for 3 or 10 days. Quantitative real-time PCR (RTQ-PCR) was conducted using SYBR Green technology and analyzed on AbiPrism 7000 (Applied Biosystems). Primer sequences used for SOD2 were cagatcatgcagctgcacca (f) and tcagtgcaggctgaagagca (r) and for β-tubulin agattactgccctggctcct (f) and acatctgctggaaggtggac (r). Western Blot (WB) analysis was performed by standard protocol. Membranes were incubated with rabbit polyclonal anti-SOD2 antibody (Abcam). After incubation with donkey anti-rabbit IgG horseradish peroxidase conjugated secondary antibody (Santa Cruz Biotechnology), visualization was performed on X-ray films (Kodak) with the use of chemiluminescence. For each blot, β-tubulin (Invitrogen) was used as a loading control.

Results and Discussion

Since SOD2 is the first line of defense against ROS it can be induced by various insults in the CNS, hence there is large body evidence on this enzyme expression and function after brain insult (4). Accordingly, our results confirmed that SOD2 protein expression is increased after CSI for 2.5-fold at 3 dpi, which at later time point (10 dpi) was reduced to half of this value (Fig.1.B). It can be assumed that this is, most likely, a response to elevated ROS after injury (4). RTQ-PCR analysis has revealed that, compared to control, CSI remarkably reduced SOD2 mRNA levels at 3 dpi (for 60%) and 10 dpi (for 30%), (Fig. 1C).
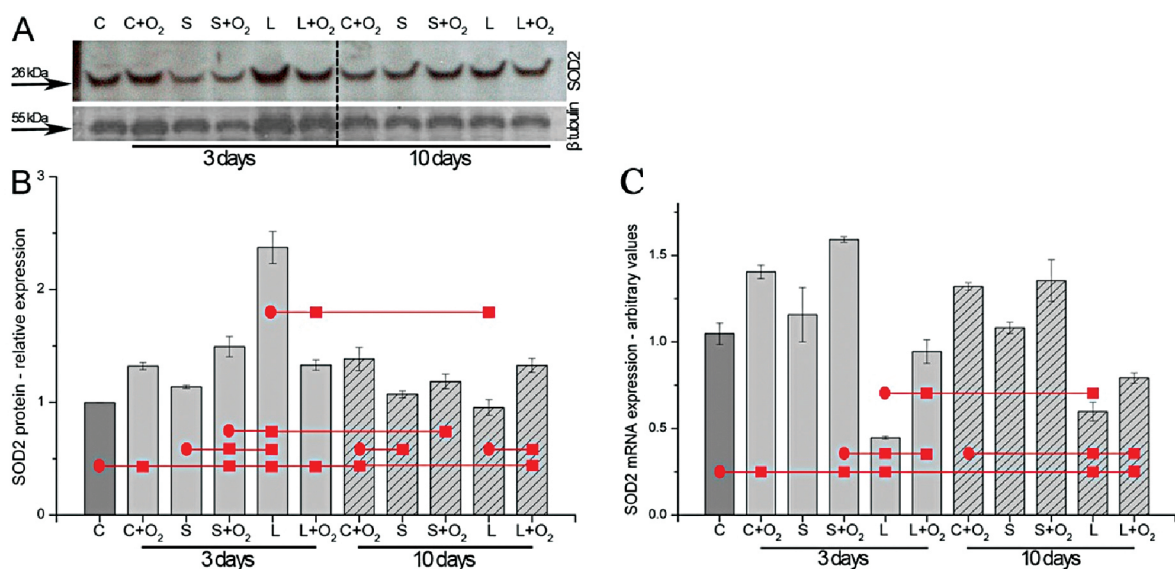
Figure 1. SOD2 proteins and mRNA expression. A. Representative immunoblots for SOD2 and β-tubulin. The SOD2 antibody shows one immunoreactive band at 26 kDa. B. Relative optical densities for SOD2 immunoreactive bands (n=6). C. SOD2 mRNA expression on RTQ-PCR. All values are calculated in comparison to the control group as mean±SEM. Values of p<0.05 were considered as statistically significant, denoted as: •, referent group and ■, group that is being compared.

Section S2: Neurobiophysics

This incongruent expression between SOD2 mRNA and protein emphasize the importance of investigation of post-transcriptional regulatory mechanisms involved, which can be unveiled only through integrated analyses of both proteins and mRNAs.

Oxygen is one of the most commonly used therapeutic agents. Inattentive use of oxygen at high partial pressures (pO2) can cause damage due to its toxic potential. This eventually led to skepticism regarding use of HBOT (10), but also to a ⬜numerous research studies on this subject. Therefore, the main focus of our work has been directed towards impact of HBOT on time-dependent changes of SOD2 expression after brain injury. WB and RTQ-PCR analysis revealed that HBOT induces a slight increase in SOD2 expression in $C+O_2$ and $S+O_2$ groups at 3 and 10 dpi, which is probably a consequence of hyperoxic challenge.

Our results concur with earlier findings, where it was demonstrated that pretreatment with HBO increases SOD2 expression, which than has a protective effect in ischemia (11). Interestingly, we have observed that HBOT applied after SCI restores SOD2 levels to almost control values at 3 and 10 dpi, on both mRNA and protein level (Fig. 1.B, C). Freiberger and colleagues previously published similar observation in the model of brain ischemia (12), but we are first to show the effect of HBOT on oxidative status observed through prism of SOD2 expression after brain injury. It has been shown that HBOT increases pO_2 in the brain tissue and restores mitochondrial redox potential (13). In our recently published paper we have reported that HBOT can intensify neuroplastic responses by promoting axonal sprouting and synapse remodeling, which contributes to the recovery of locomotor performances in rats (9). Considering aforesaid, we propose that this recovery after TBI might be in part due to appropriately applied HBOT which maintained low ROS levels by restoring SOD2 expression.

Acknowledgments

22

References

1. Masel B.E. 2010, J. Neurotrauma, 27: 1529-40
2. Werner C. 2007, Br J Anaesth., 99: 4-9
3. Smith S.L. 1994, J. Neurotrauma, 11(4): 393-404
4. Bidmon H.J. 1998, Stroke, 29: 203-211
5. Keller J.N. 1998, J. J Neurosci., 18: 687-697
6. Lei H. 2011, Med. Gas. Res., 92: 1519-21
7. Wang G.H. 2010, J. Neurotrauma, 27: 1733-43
8. Nedeljkovic N., 2006, Cell Biol. Int., 30(6): 541-6
9. Brkic P. 2012, Brain Inj., Epub ahead of print
10. Bitterman, H. 2009, Crit. Care, 13: 205
11. Wada K. 2000, Acta Neurochir. Suppl., 76: 285-90
12. Freiberger J.J. 2006, Brain Res., 1075: 213-22
13. Rockswold S. 2007, Neurol. Res., 29(2): 162-72

CYCLIC VOLTAMMETRY IN DIAGNOSIS OF ALS

Tihana Mudrinić[1]
Zorica Mojović[1]
Dušan Jovanović[1]
Aleksandar Ignjatović[2]
Miloš Mojović[2]
Goran Bačić[2]

[1] University of Belgrade, Institute of Chemistry, Technology and Metallurgy, Department of Catalysis and Chemical Engineering, Njegoševa 12, 11000 Belgrade, Serbia
[2] Faculty of Physical Chemistry, University of Belgrade, Studentski trg 12–16, 11000 Belgrade, Serbia

Abstract

The diagnosis of amyotrophic lateral sclerosis (ALS) based on ALS functional rating scale-revised (ALSFRS-R) scores is often shown to be unreliable and false. On the other hand, magnetic resonance imaging (MRI) studies of a brain of ALS patients showed the presence of iron deposits in the precentral gyruses of gray matter (PGGM) and also the potential leakage of iron to cerebro-spinal fluid (CSF) through compromised blood-brain barrier. The aim of this study was to determine if there is a specific feature in CSF that distinguishes patients with ALS from the control subjects. CSF obtained from ALS patients and normal controls were analyzed using the technique of cyclic voltammetry. The results show that, at the potential of 1.1 - 1.2 V vs. Ag/AgCl electrode, the plateau appeared and the potential of oxygen evolution was shifted toward more positive values for the ALS patients. These voltammogram features were not present for the control patients showing this technique to be promising candidate for evaluating new biomarkers for ALS.

Introduction

ALS is neurodegenerative disease which includes progressive degeneration of the motor neurons leading to weakness and atrophy. Although it is far from being curable [1], ALS is treatable, but reliable biomarkers are needed to follow up effects of potential drugs. Developing of ALS is most probably linked to the cell malfunctions and disturbed metabolism of reactive oxygen and nitrogen species which causes motor neuron cell damage [2,3]. As the chemical composition of CSF shows shortage of antioxidants and iron-binding proteins, CSF is highly exposed to Fenton-like chemistry reactions. Since nervous tissue spontaneously generates and releases H_2O_2 into the CSF [4,5], it is of primary interest to understand the iron metabolism of neural tissues. Iron deposits in the motor cortex and other brain regions of ALS patients have been observed two decades ago using MRI [6] and subsequently confirmed in number of studies indicating that preconditions for free radical reactions related to Fenton chemistry have been fulfilled. However, attempts to somehow quantify the free or helated iron content in CSF of ALS patients and correlate those results with ALSFRS-R scores, has proved to be rather difficult task [7]. Furthermore, the diagnosis of ALS based on the ALSFRS-R scores is often shown to be unreliable and false. Given that the redox activity of iron is related to the presence of specific ligands [8,9], there was a need for developing a new experimental approach which could expose the existence of ligands which could form a redox-active iron complexes in the CSF of ALS patients. In this paper, the technique of cyclic voltammetry was applied to determine if there is a specific feature in voltammogram of CSF that distinguishes patients with ALS from the control subjects.

Material and methods

Patients For this study, CSF of patients diagnosed with sporadic ALS was used. The ALSFRS-R scores were obtained from the participants who were informed that their CSF was to be used for our research

and provided written consent. The ALS group consisted of 32 males and 17 females. The control group consisted of 6 patients with other neurological disorders: tension headaches, lumbar disc herniations and migraines. CSF samples (1.5 ml) were obtained after an overnight bed-rest and fasting, by lumbar puncture. Samples were centrifuged (5000 g, 10 min at 4°C) and rapidly frozen and stored at - 80° C.

Method The electrochemical investigation was performed in a three-electrode all glass cell. A platinum rotating disc electrode was used as a working electrode. The reference electrode was Ag/AgCl in 1M KCl, while a platinum foil served as a counter electrode. The supporting electrolyte was 0.9 % NaCl. The device used for the electrochemical measurements was 757 VA Computrace Metrohm. The measurements were performed at potential rate of 50 mV/s, and rotation rate of 1000 rpm.

Results and Discussion

The results show that, at potential of 1.1 - 1.2 V vs. Ag/AgCl electrode, for the ALS patients, the plateau appeared and the potential of oxygen evolution was shifted toward more positive values (Fig. 1a). The plateau in cathodic sweep was better resolved then in anodic sweep. These voltammogram features were not present for the control patients (Fig. 1b). The measurements were performed for 49 samples of ALS patients and 6 control patients. The cathodic current response at 1.1 V varied in the range of 1.4 - 4 mA. However, the obtained results could not be correlated with ALSFRS-R scores. Furthermore, some patients with high ALSFRS-R scores had high current response and vice versa.
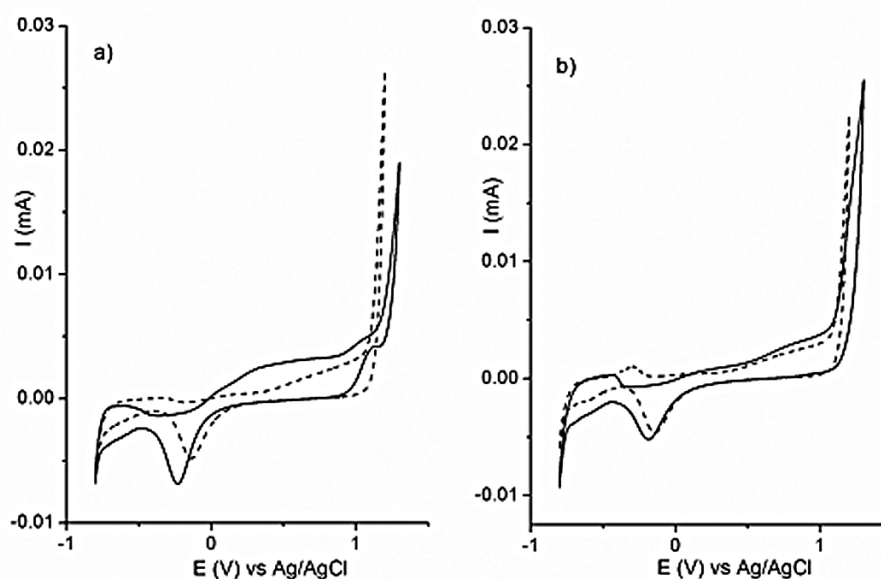
Figure 1. Cyclic voltammogram in 0.9 % NaCl without (dashed line) and with (solid line) CSF for a) ALS patient and b) control patient.

The present problem is the identification of the specie that causes the obtained response. Some preliminary results indicate that this specie could be some Fe^{2+}/Fe^{3+} binding protein or ligand. Since the signal disappeared from cyclic voltammogram upon addition of Fe^{2+}/Fe^{3+} ions in the solution, the calibration could be preformed allowing the estimation of the concentration of the unknown entity in the CSF sample (results not shown). Control measurements were performed to exclude the possibility that plateau derives form Fe^{2+}, Fe^{3+}, Ascorbate or Ascorbyl radical, which are shown to be present in CSF. The recordings performed on different polarization rate and rotation rate indicated that process of oxidation-reduction of this specie is reversible and controlled by mass transport.

Conclusions

Early diagnosis of ALS is difficult task because it may appear similar to several other neurological diseases. Up to date, the diagnosis of ALS is based on excluding other conditions using diagnostic

techniques like electromyography, nerve conduction studies, MRI, blood and urine tests and muscle biopsy. Possible reasons for developing ALS are still unknown and current studies suspect several possible causes such as gene mutation, disorganized immune response or chemical imbalance (especially related to the level of glutamate in CSF). However, we imply that the emergion of Fenton-like chemistry suitable environment in the CSF of ALS patients may be the main cause for ALS outbreak and progression. Accordingly, it is of primary interest to understand iron metabolism of neural tissues especially considering the presence of chelator agents that are likely to be responsible for possible formation of various redox active iron complexes, promoting the production of short-lived free radicals (especially ${}^{\bullet}OH$) in the Fenton chemistry of the CSF. The cyclic voltammetry is fast and inexpensive technique and appear to be promising candidate for evaluating new biomarkers for ALS. Up to date, there are no reports on using cyclic voltammetry for evaluating the presence of metal complexes or ligands in CSF of ALS patients. We have shown that cyclic voltammograms of CSF of ALS patients have distinguishing feature in comparison to CSF of control patients and suspect that this difference could derive from the existence of various chelator agents, ligands or complexes. However, further extensive investigations are necessary to confirm this hypothesis by detecting specific chemical features which are responsible for this observation.

Acknowledgment

References

1. R. G. Miller, Amyotrophic Lateral Sclerosis, New York, Demos Medical Publishing, 2005.
2. J. P. Julien, J. M. Beaulieu, J. Neurol. Sci., 2000, 180, 7 – 14.
3. P.J. Shaw, P.G. Ince, J. Neurol., 1997, 244, S3 – 14.
4. B. Halliwell, J. M. C. Gutteridge, eds. Free Radicals in Biology and Medicine. Oxford: Oxford University Press 2007.
5. D. Liu, J. Wen, J. Liu, L. Li, FASEB J., 1999, 13, 2318 – 28.
6. H. Oba, T. Akaki, H. Ohtomo, Radiology, 1993, 189, 843-6.
7. A. Ignjatović, Z Stević, D. Lavrnić, A. Nikolić-Kokić, D. Blagojević, M. Spasić, I. Spasojević, Amyotroph Lateral Sc., 2012, 13, 357-362.
8. D. B. Kell, BMC Med. Genet. 2009, 2, 2.
9. D. B. Kell. Arch Toxicol. 2010, 84, 825 – 89.

ION CHANNELS IN CYTOPLASMIC DROPLETS MEMBRANE FROM FUNGUS PHYCOMYCES BLAKESLEEANUS

Strahinja Križak[1]
Ljiljana Nikolić[2]
Nataša Todorović[2]
Marina Stanic[1]
Milan Žižic[1]
Željko Vučinić[1]
Miroslav Živić[3]

[1] Institute for Multidisciplinary Research, University of Belgrade, Kneza Višeslava 1, 11030 Belgrade, Serbia
[2] Institute for Biological Research "Sinisa Stankovic", University of Belgrade, Despota Stefana 142, 11000 Belgrade, Serbia
[3] University of Belgrade - Faculty of Biology, Studentski trg 16, 11000 Belgrade, Serbia

Abstract

Whole cell and single channel patch-clamp recordings were obtained from membrane of cytoplasmic droplets of *Phycomyces blakesleeanus*. A channel with slow rectification of outward currents carried by Cl^- ions is most prominent in whole cell mode. Single channel recordings revealed the presence of at least 3 types of ion channels.

26

Introduction

Ion channels in membranes from filamentous fungi are poorly characterized since obtaining high quality membrane seals of hyphal cell membrane is improbable due to the difficulties in removal of the cell wall completely (1). We developed model system of *Phycomyces blakesleeanus* cytoplasmic droplets which rapidly form membranes *de novo*, corresponding to hyphal plasma membrane, thus bypassing the problems of the cell wall residues (1,2).

Material and methods

A wild type strain of the fungus *Phycomyces blakesleeanus* (Burgeff) NRRL1555(-) was used in this study. The fungi was grown in conditions described previously (3). Stage IVb sporangiophores were the source of cytoplasmatic droplets. The tips of the sporangiophores were immersed in a solution isoosmotic to the cytoplasm (bath solution) and cut in the elongation zone. After excision, the released cytoplasm formed many cytoplasmic droplets. Bath solution contained (in mM): KCl 125, $CaCl_2$ 1, $MgCl_2$ 2, Hepes 10, sucrose 165, pH 7.0 (KOH), osmolarity 495 mOsm. Cytoplasmatic droplets were placed in a recording chamber and incubated in the bath solution. It was shown that (2,4) after 10-15 s cytoplasmic droplets de novo synthesized their membranes that structurally and functionally correspond to the cell membrane of intact hypha.

For whole-cell patch-clamp recordings (5) patch pipettes were pulled from borosilicate glass capillaries (WPI, Berlin, Germany) using P-97 horizontal Flaming-Brown puller (Sutter Instruments Co, USA). Pipette resistance was 5-6 MΩ when filled with (in mM): KCl 125, EGTA 10, Hepes 10, $MgCl_2$ 2, sucrose 205, pH 7, 550 mOsm. In experiments with K-gluconate, KCl was replaced equimolarly with K-gluconate in both, extracellular and pipette solution. Prepared vesicles were placed in the recording chamber on the stage of an inverted Zeiss Axiovert 10 microscope and patch-clamp recordings were

performed using an AM Systems 2400 amplifier and Clampex 10 software (Molecular Devices, USA) at room temperature. Current signals were low-passed filtered at 2 kHz and digitized at 50 kHz using a Digidata 1200 interface (Molecular Devices, USA). Stimulation protocol consisted of series of voltage steps in 20 mV increments (-150mV to +70mV) from holding voltage of -50mV. Whole droplet membrane capacitance and membrane and access resistance were measured by Membrane Resistance mode in Clampex 10.0. The series resistance compensation was not applied. Analysis was performed in Clampfit 10.0 (Molecular Devices, USA).

Ion channel activity was measured in inside-out configuration of patch–clamp technique. The borosilicate glass capillaries (0.86 mm i.d.; Clark Electro-medical Instruments, Berkshire UK), were pulled on a vertical puller (Stoelting Co., Wood Dale, IL). After filling the micropipettes with an internal solution with the same composition as the bathing solution, the resistance of microelectrodes was 10 – 20 MΩ. Continuous recordings and ramp protocols (-120 mV to +120 mV in 240 ms and -60 mV to +60 mV in 500 ms) were used. Acquisition was performed at a frequency of 3 kHz by EPC9 patch-clamp amplifier (HEKA Elektronik GmbH,Germany) controlled by an EPC9 SCREEN (HEKA) acquisition program on an Atari Mega ST-4 minicomputer. Single channel recordings were analyzed by the half-threshold technique (5), using TAC software (Bruxton Corporation, Seattle, WA).

Results and Discussion

This is the first report of a patch clamp recording in a whole cell configuration from *P. blakesleeanus* vesicles. Whole-cell recordings showed presence of both inward and outward currents in the presence of symmetrical KCl concentration, n=5 (Fig. 1a, 1b, left panels).
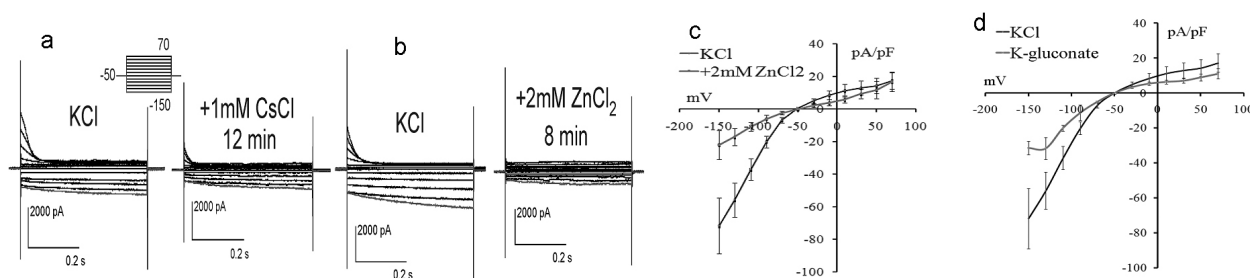

Figure 1. Whole-cell voltage activated currents in the cytoplasmic droplets membrane. Stimulation protocol is shown in inset. 1a and 1b. Representative examples of recordings of families of currents. Left panels: recording in control conditions (in KCl). Right panels: recording with hyperosmotically added ion channels blockers, from the same whole-cell patch as shown on the left. 1a. CsCl blocks inward currents. 1b. ZnCl2 block. 1c and 1d. Voltage dependence of current densities, obtained by dividing amplitude of the current by capacitance of membrane. Values shown are mean±SE. 1c I-V curves in 2mM ZnCl2 and in control conditions showing marked block of inward currents. 1d. I-V curves in K-gluconate, same control curve as in 1c shown for comparison.

Notable property of whole-cell currents was rather slow activation of inward currents at -150 mV. Even more pronounced is the presence of a "shoulder" at the beginning of response to depolarization step, presumably demonstrating very slow process of channel block responsible for rectification of outward currents. In preliminary experiments the addition of 1 mM CsCl partially blocked inward currents (by 30% at -130mV) while weak block could be observed on outward currents demonstrating presence of potassium channel activity (Figure 1a). Addition of 2 mM $ZnCl_2$ induced block of both inward and outward currents (70% at -130mV), showing the presence of an anion channel with CLC-2-like properties (6), n=2, Figure 1b. From Figure 1c. it can be observed that rectification of whole cell currents is lost in 2mM $ZnCl_2$, and also a 'shoulder' in outward currents is no longer visible, suggesting that the prominent feature of slow rectification is correlated with an anionic conductance. Next, Cl- ions from symmetrical solutions were exchanged for gluconate, and a reduction of currents was observed (Figure 1d). Our preliminary data with block of currents in symmetrical K-gluconate by 2mM $ZnCl_2$ suggest that anionic CLC-2-like channels present on *P. blakesleeanus* droplets membrane permeate gluconate although less than Cl- ions (data not shown).
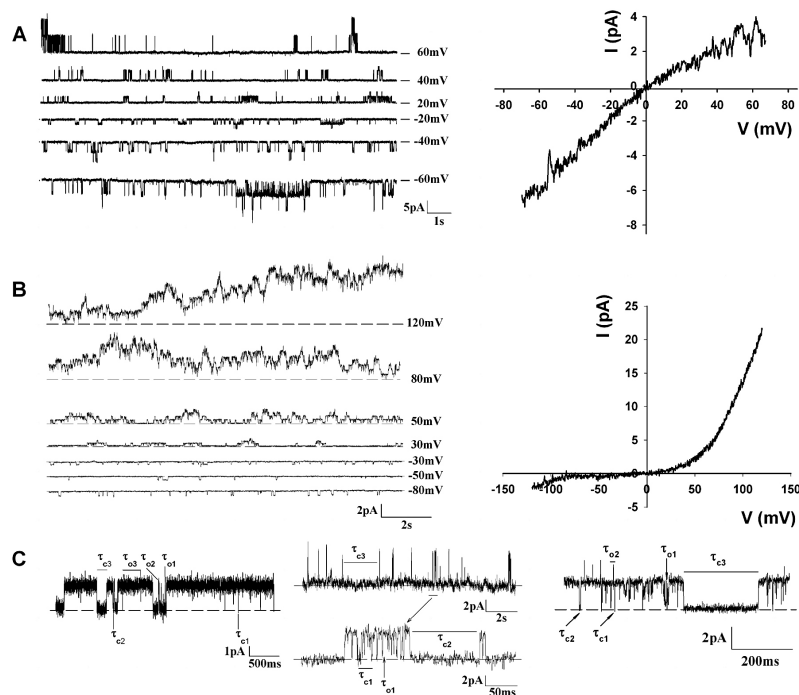
Figure 2. *Inside-out single-channel recordings from cytoplasmic droplet membrane of P. blakesleeanus. A) Current recordings of large conduntace channel (112pS) at different holding potentials indicated on the right (left) and open-channel current responses obtained by applying rapid voltage ramps (from -60 to 60 mV in 240 ms) showing small invard rectification (right). The trace shown is the mean of 80 scans; before the average was formed, leak subtraction was performed and closing events that occurred during a scan were removed. B) Current recordings of small conductance (10 pS) anionic outward rectifier (ORAC) at different holding potentials indicated on the right (left) and open-channel current responses obtained by applying rapid voltage ramps (from -120 to 120 mV in 240 ms) showing strong outward rectification (right). The trace shown is the mean of 80 scans; before the average was formed, leak subtraction was performed and closing events that occurred during a scan were removed. C) Continuous recordings at 50mV, 120mV and -50mV holding potentials respectively from left to right of three discintive types of 40pS channel(s) activity. Open and closed events which duration corresponds to the characteristic dwell times (for dwell times values see Table 1) are marked with arrows or bars and corresponding dwell time symbol.*

Single-channel investigation of the same droplets membranes in inside-out configuration of patch-clamp method showed the presence of three predominant channel types. Channel with large conductance (112 pS) and weak inward rectification was present in 68% patches when recorded in the presence of ATP (Figure 2A). Small conductance (10 pS) anionic outward rectifier (ORAC) was present in 40% patches (Figure 2B). A channel(s) with 40pS conductance with three distinct types of channel activity, none with rectification properties, was present in 88% patches (Figure 2C). The single-channel properties of three types of channel activity of 40pS amplitude, possibly representing several different ion channels, are presented in Table 1.

	t_{o1}	t_{o2}	t_{o3}	t_{c1}	t_{c2}	t_{c3}
Activity type I	1.8±0.3ms 33±4%	27±11ms 25±5%	298±15ms 42±6%	2.1±0.4ms 63±9%	27±6ms 33±1%	246±66ms 4±1%
Activity type II	5.2±0.4ms 100%	/	/	1.2±0.1ms 81±2%	21±4ms 6±1%	6±0.5ms 13±2%
Activity type III	1.4±0.3ms	16±1ms 45±7%	/ 55±7%	0.8±0.1ms	17±9ms 82±4%	421±99ms 14±2% 4±1%

Table1. *Dwell times and fractional occupancies for 40pS conductance ion channel activity types*

In summary, we show that ion currents, when recorded in the whole-cell configuration, in the membrane of cytoplasmic droplets of *P. blakesleeanus* are dominated by a CLC-2 like anionic rectifier while a fraction of current is carried through potassium channels also. Single-channel conductance with closest resemblance to the whole-cell anionic current is ORAC, although that correlation remains to be further established.

Acknowledgements

References

1. Živić, M., Popović, M., Živanović, B., and Vučinić, Ž. (2005). Ann. N.Y. Acad. Sci. 1048: 491-495.
2. Živić, M., Popović, M., Todorović, N., and Vučinić, Ž. (2009). Eukaryotic Cell, 8: 1439–1448.
3. Živanović, B., K. Köhler, P. Galland, and M. Weisenseel. 2001. Electro Magnetobiol. 20: 343-362.
4. Zaichkin, E.I., Orlova, S.A. and Fikhte, B.A. (1975). Doklady Academii Nauk SSSR 225: 1187-1189.
5. Hamill, O. P., Marty, A., Neher, E., Sakmann, B. and Sigworth F. (1981). Pflügers Archiv 319: 85-100.
6. Taylor A., Brownlee C. (2003). Plant Physiol.131: 1391-400.

ELECTROPHYSIOLOGICAL PHENOTYPE OF CULTURED RAT MICROGLIA IN RESTING VS. LPS-ACTIVATED STATE AND THE EFFECT OF RIBAVIRIN

N. Todorovic[1]
D. Savic[1]
M. Zivic[2]
I. Lavnja[1]
A. Parabucki[1]
I. Bozic[1]
S. Pekovic[1]
M. Stojiljkovic[1]

[1]   Institute for Biological Research "Sinisa Stankovic", University of Belgrade, Serbia
[2]   Department of Physiology and Biochemistry, University of Belgrade-Faculty of Biology, Serbia

Abstract

Pure cell cultures of untreated microglia and microglia in activated state (stimulated with 25ng/ml LPS for 48h) were used for whole-cell patch clamp recording. Outward current density in LPS treated microglia was measured to be significantly larger than in control cells, and same was true for cell size measured as cell capacitance. We performed preliminary study of effect of ribavirin, a drug under investigation for its immunomodulatory potential, on microglial electrophysiological properties. LPS+ribavirin-treated cells did not differ from ribavirin-treated cells in current densities, suggesting that ribavirin treatment might modulate electrophysiological properties of microglia.

Introduction

Microglia, the resident immune cell type in the central nervous system, besides its protective role, exerts the proinflammatory action in chronic inflammatory conditions such as in multiple sclerosis. Recently, the pure culture of microglia (97% of cells) has been used as *in vitro* model system for assessment of immunosuppressive action of ribavirin (10 µM) on microglia activated by low concentration (25 ng/ml) lipopolysacharide (LPS), demonstrating reduction of NO release and reversal of activated cell morphology. Ribavirin (1-β-D-ribofuranosyl-1,2,4-triazole-3-carboxamide) is clinically used inhibitor of inosine 5'-monophosphate dehydrogenase, the rate-limiting enzyme of *de novo* GTP biosynthesis. Ribavirin is clinically approved for antiviral action, while several animal studies demonstrated its immunosuppressive potential in the animal model of multiple sclerosis[1,2]. We performed patch-clamp measurements to characterize electrophysiological properties of microglia cells in the same *in vitro* model of pure culture in: control, LPS-treated, ribavirin-treated and (ribavirin+LPS)-treated cells.

Material and methods

Substance used were lipopolysaccharide (LPS) from *Escherichia coli* 026:B6 (Sigma-Aldrich Chemie GmbH, Germany); Ribavirin (RBV, MP Biomedicals, LLC, Illkirch, France)

Cell Culture The preparation of microglia from rat cortex up to 3 days postpartum was described previously[3a] (Giulian and Baker, 1986). The cultures were kept in Dulbecco's Modified Eagle's Medium (Gibco, InvitrogenCo, CA, USA) with 10% FCS and 1% pen/strep (both PAA Laboratories GmbH, Austria). The medium was changed every 2–3 days. After 10–14 days, microglial cells were detached from the astrocyte layer and pelleted from the medium by centrifugation (3000 rpm 5 min). The

supernatant was kept as astrocyte-conditioned medium (ACM). For morphological analysis and electrophysiology cells were plated at 4×10^4 on glass cover slip circles (14 mm) in 35-mm dishes with 2 ml ACM.

Treatment of microglia Cells plated as described were kept in cell culture incubator at 37°C for 48, unless stated otherwise, in 4 groups: Control (no treatment); LPS (in the presence of 25 ng/ml LPS); RBV (in the presence of 10 μM RBV); LPS+RBV (in the presence of 25 ng/ml LPS and 10 μM RBV) and than used for electrophysiology.

Electrophysiology Electrophysiological recordings were obtained in the whole-cell configuration of the patch-clamp technique. Patch pipettes were pulled from borosilicate glass capillaries (WPI, Berlin, Germany) using P-97 horizontal Flaming-Brown puller (Sutter Instruments Co, USA). Pipette resistance was 4-7 MΩ when filled with intracellular solution composed of (in mM): 144 KCl, 2 $MgCl_2$, 5 EGTA, 10 HEPES, pH 7.2 (290 mOsm). Extracellular solution contained (in mM): 140 NaCl, 4 KCl, 2 $MgCl_2$, 2 $CaCl_2$, 10 HEPES, 5 glucose, pH 7.4 (300 mOsm). Cells cultured on glass coverslips were placed on the stage of an inverted Zeiss Axiovert 10 microscope and patch-clamp recordings were performed using an AM Systems 2400 amplifier and Clampex 10 software (Molecular Devices, USA) at room temperature. Current signals were low-passed filtered at 2 kHz and digitized at 50 kHz using a Digidata 1200 interface (Molecular Devices, USA). Stimulation protocol consisted of series of voltage steps in 20 mV increments from holding voltage of -50 mV (from -150 to 70mV). Whole cell membrane capacitance along with membrane and access resistance was measured using Membrane Resistance mode in Clampex 10.0 acquisition software. The series resistance compensation was not applied. Statistical analysis was preformed by t-test in Sigmastat software.

Results and Discussion

The morphology of control and LPS-stimulated cells in *in vitro* model of pure culture of microglia is shown in Fig. 1.
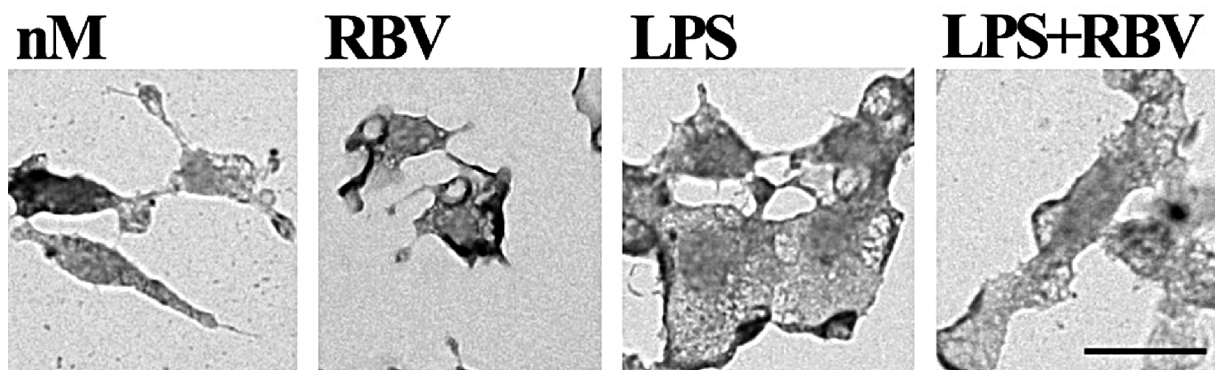

Figure 1. Photomicrographs showing appearance and size of representative cells in following experimental groups: control (nM), ribavirin-treated (RBV), LPS-treated (LPS) and treated with LPS+ribavirin (LPS+RBV). Scale bar is 25 μm.

Many cells in LPS group are large, devoid of long branched processes, with morphological appearance resembling "fried-egg". Only cells with these characteristics were selected for recording in LPS group. Even so, large variation in current properties was found, probably due to different amounts of activation. Similarly, only small, branched cells were chosen for recording in control group, and there too variation in current density was found (Fig. 2b). Overall, the recorded families of currents from cultured microglia corresponded well to published studies, where predominant currents were shown to be carried through inward rectifying K channels (presumably made from Kir 2.1) while outward currents are mostly carried through delayed rectifier potassium channels (having Kv 1.3 subunit)[4] (Fig. 2a).

We found that resting and activated microglia outward currents normalized to cell capacitance differ significantly, activated microglia having almost double current density at 50 mV step (Figure 2b). Inward current density varied between the cells in the same group so no conclusion could be reached as if LPS treatment induces their increase as well, although similar findings were reported[3].

Section S3: Membrane and cell biophysics

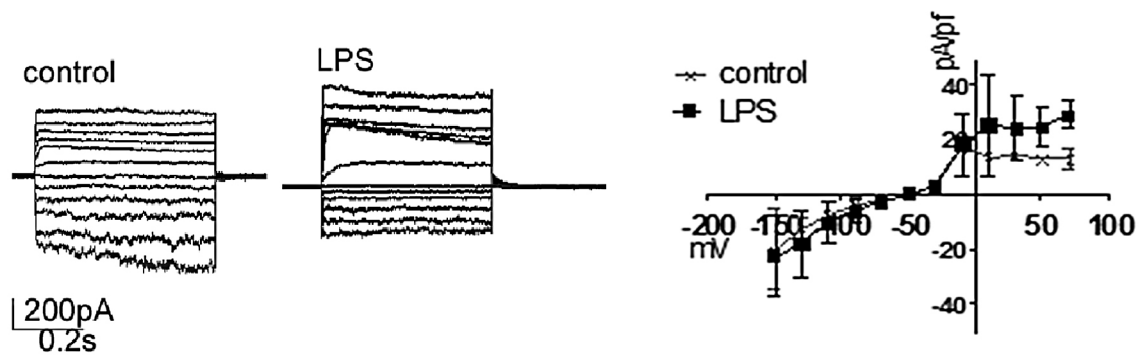*Figure 2. Voltage activated currents in microglia. a. representative examples of recordings of families of voltage activated currents. b. Voltage dependence of current densities (current amplitudes normalized to cell capacitance) from control and LPS-treated microglia. Values presented are mean±SD (n=6). Note large variation of inward current densities in both groups.*

In compliance with the idea of overall suppression of activated phenotype by ribavirin, we found the cell size, measured by cell capacitance in whole-cell patch-clamp is significantly increased from 16±3 pF (n=6) in control, to 36±3 pF (n=9) in cells treated with LPS while reduced to 23±5 pF (n=8) in the cells treated with ribavirin and LPS, not different than control (Fig. 3a)
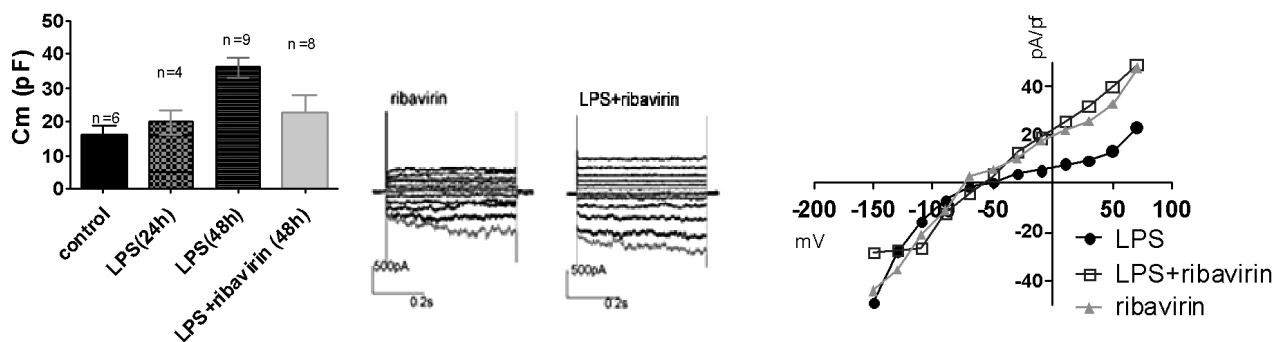
Figure 3. The effect of ribavirin on electrophysiological properties of microglia. a. Ribavirin treatment prevents LPS induction of cell size increase. Cell capacitance from (ribavirin+LPS)-treated cells and 24h LPS-treated cells is not different from control. Values shown are mean±SE. b. Example of recordings of families of voltage activated currents from microglia treated as marked. c. Voltage dependence of cell current densities from LPS-treated and ribavirin- and ribavirin+LPS-treated cells from representative recordings.

Our preliminary findings (n=2 in each group) of the effect of ribavirin on microglia currents show that LPS does not induce an increase of outward currents in ribavirin treated cells, as compared to the cells treated with ribavirin alone (Figures 3b, c). Notably, it seems that ribavirin alone may induce current profile that looks more characteristic for activated than control state of microglia. In the same time, morphology of ribavirin-treated cells (Figure 1c and d) and their size are very different from the properties of activated cells. In summary, our preliminary data suggest that ribavirin treatment might modulate electrophysiological properties of microglia.

References

1. Milicevic et al., J Neurosci Res 2003, 72:268-278
2. Lavrnja et a.l, Int immunopharmacol 2008, 8:1282-1290
3. Giulian D, Baker TJ. J Neurosci 1986, 6:2163–2178
4. Eder C. Am J Physiol. 1998:C327-42.

METABOLISM OF PHOSPHATE COMPOUNDS DURING OXYGEN DEPRIVATION IN FUNGUS PHYCOMYCES BLAKESLEEANUS: POSSIBLE CONNECTION WITH CHANGES IN RESPIRATION

M. Stanić[1]
M. Hadžibrahimović[2]
M. Žizić[1]
J. Zakrzewska[3]
M. Živić[4]

[1] *Institute for Multidisciplinary Research, Kneza Višeslava 1, 11030 Belgrade, Serbia*
[2] *Department of Biology, State University of Novi Pazar, Vuka Karadžića bb, 36300 Novi Pazar, Serbia*
[3] *Institute of General and Physical Chemistry, Studentski trg 12-16, 11000 Belgrade, Serbia*
[4] *University of Belgrade-Faculty of Biology, Studentski trg 16, 11000 Belgrade, Serbia*

P R O C E E D I N G S

Abstract

The effect of oxygen deprivation on phosphate metabolites in *P. blakesleeanus* was investigated by ^{31}P NMR spectroscopy. It caused a reversible decrease of polyphosphate to inorganic phosphate (PPc/Pi) intensity ratio. ATP content decreased less than expected, probably due to ability of PolyP to sustain energy and phosphate homeostasis of the cell under stress conditions. Aplication of azide, a cyt c oxidase inhibitor, also decreased PPc/Pi ratio, but to a lesser extent in oxygen deprived than control and oxygenated specimens. This finding suggests that there could be a connection between this process and relative activity of mitochondrial respiratory enzyme alternative oxidase.

33

Introduction

Phycomyces blakesleeanus is a zygomycetous fungus not easily spotted in nature, it grows on decaying organic matter, and needs humid environment for growth. It is considered to be a strictly aerobic fungus (1), but can be often exposed to unfavorable growth conditions such as hypoxia or even anoxia due to terrain flooding, which is bound to have the effects on cellular energy metabolism, but such effects have been insufficiently studied.

We have previously noticed that oxygen deprivation causes decrease in cyt c oxidase activity but not in the alternative oxidase (AOX) activity, making it prevailing enzyme in respiratory chain during hypoxia and anoxia. Work on *P. membranifaciens, D. hansenii* and *G. graminis* showed that the activity of alternative respiration in fungi can be involved in ATP formation and that it is an essential component of proton motive force generating system (2). There are strong indications that in fungi apart from ATP, inorganic polyphosphates (PolyP) play an important role in energy metabolism (3), and one of its assumed roles is participation in cellular response to unfavorable conditions and stress by hydrolysis to provide the energy for maintenance of cellular processes (4) ^{31}P NMR spectroscopy is uniquely suited for nondestructive *in vivo* studies of ATP and other phosphate molecules involved in cellular energy metabolism.

Material and methods

The wild type strain of the fungus *P. blakesleeanus* (Burgeff) (NRRL 1555(-)) was used in this study. Spores, in concentration of 10^6, were cultivated in modified liquid standard minimal medium (5). Samples of mycelium were incubated for 1.5, 3 and 5 h in hypoxic and anoxic conditions. Anoxic conditions were created according to (6) with nitrogen instead of argon, and hypoxic in the same

manner only without nitrogen bubbling. For reoxygenation measurements, samples were bubbled with air for 20 minutes. ^{31}P NMR measurements were performed using Apollo upgrade, Bruker MSL 400 spectrometer operating at 161.978 MHz for ^{31}P, and samples were prepared according to (7).

Results

Most obvious changes in *P. blakesleeanus* ^{31}P NMR spectra (Fig. 1A) were the decrease in core polyphosphate (PPc) signal intensity in both hypoxic and anoxic conditions, accompanied by the increase in intracellular inorganic phosphate (Pi) signal intensity. These changes result in the decrease of PPc/Pi ratio (Fig. 2C), which has proven to be a good indicator of overall cellular energy status (7). In control conditions, PPc/Pi ratio was 1.90 and in hypoxia it fell to 83.7%, 54.5% and 40.5% after 1.5, 3 and 5 h of treatment, respectively. In anoxia, it fell to 61.1%, 43.2% and 40%. ATP content, i.e. energy status of cell, is represented by βATP signal. βATP/Pi ratio after treatment is almost constant, ranging from 0.29 in control to 0.24, 0.23, 0.21 in hypoxic, and 0.23, 0.21, 0.21 in anoxic conditions (Fig. 2B). PPc/Pi ratio in both hypoxic and anoxic conditions decreases gradually with time which can be interpreted as the ability of PolyP to sustain energy and phosphate homeostasis of the cell (8) for at least a couple of hours under stress conditions. This is further supported by a very small decrease in the βATP/Pi ratio. After 5 h, both treated groups were exposed to 20 minutes of reoxygenation (Fig 2A). After a fall from 1.63±0.14 (n=3) in control conditions to 0.80±0.10 (n=3, p=0.009) in hypoxia, PPc/Pi ratio increased to 1.12±0.20 (n=3). In anoxic conditions PPc/Pi ratio fell to 0.71±0.07 (n=3, p=0.004) and then increased to 1.29±0.12 (n=3, p=0.014) after reoxygenation.
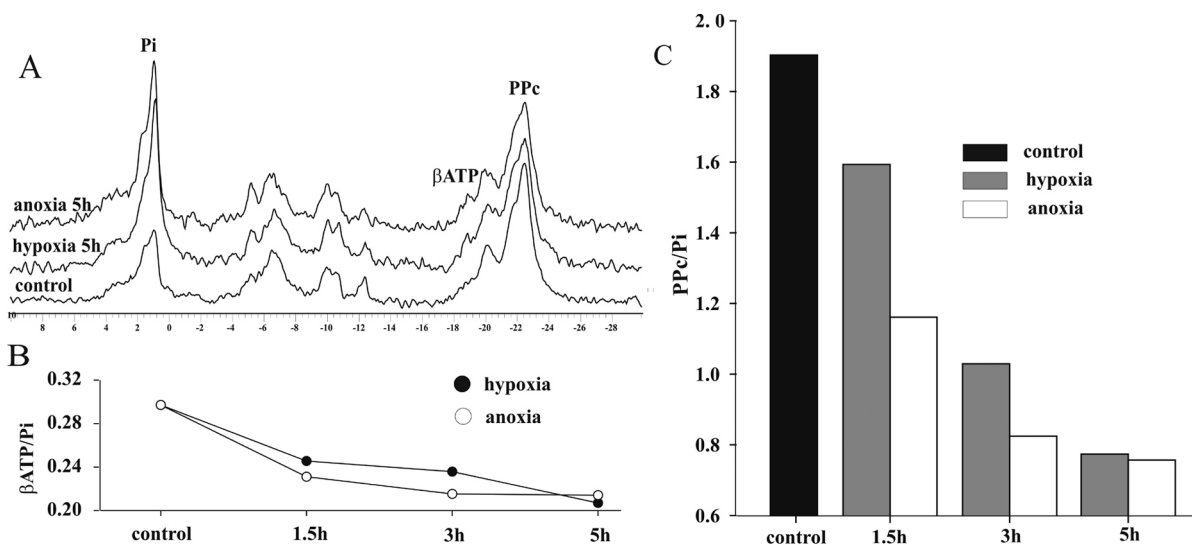
Figure 1. A: ^{31}P NMR spectra of control, hypoxic and anoxic mycelia. B: βATP/Pi ratio in control, and in hypoxic and anoxic mycelia after 1.5, 3 and 5h of treatment. C: PPc/Pi ratio in control, and in hypoxic and anoxic mycelia after 1.5, 3 and 5h of treatment.

Our previous finding that in oxygen depriving conditions AOX activity becomes prevailing, combined with the finding that βATP/Pi ratio decreases only slightly, probably due to direct PolyP involvement (9) motivated us to apply azide, a potent cyt c oxidase inhibitor, to control, treated and reoxigenated mycelia and compare them with spectra without this inhibitor. Azide decreased PPc/Pi ratio in all specimens (Fig. 3B), but the extent of its effect varied and could be distributed into three groups. In control and anoxic/reoxygenated specimens azide had a large effect decreasing PPc/Pi ratio for 27.85% and 29.6%, respectively, while in hypoxia and anoxia its effect was considerably smaller, decreasing PPc/Pi ratio for 9.4% and 10.52%, respectively. In hypoxic/reoxygenated mycelia, the decrease was 15.4%. Since anoxic micelia recovers faster than hypoxic, weaker effect of azide on hypoxic/reoxygenated than on anoxic/reoxygenated mycelia was not so surprising. It seems that mycelia exposed to anoxia exert faster response to changes in environment than that exposed to hypoxia.

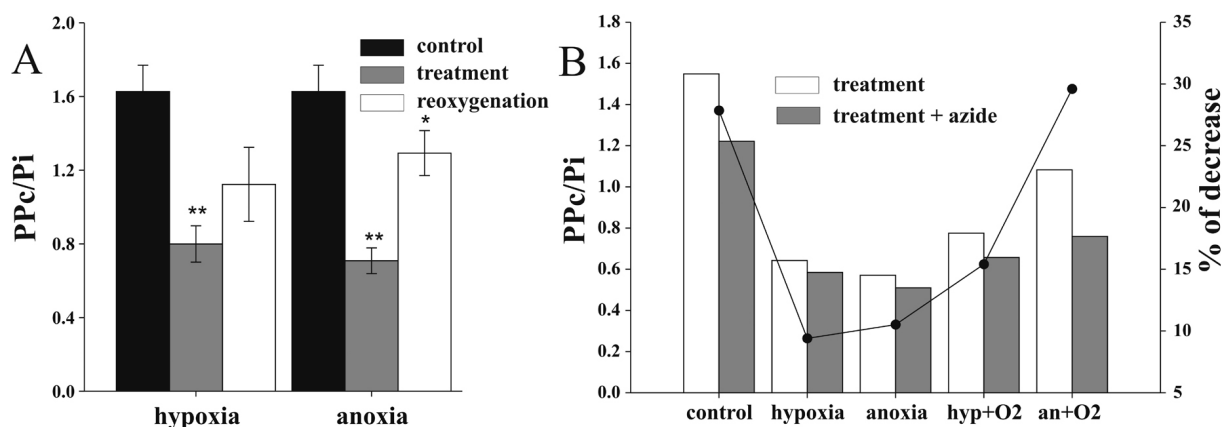**Figure 2.** *A: PPc/Pi ratio in hypoxia and anoxia and after reoxygenation. B: bars – PPc/Pi ratio before and after application of azide, line – percentage of PPc/Pi ratio decrease after application of azide*

Even though no definitive mechanism is determined, it is believed for a while now that mitochondria and cytochrome c oxidase are involved in oxygen sensing and subsequent signal transduction (10). This phenomenon is mostly associated with transcription control of nuclear aerobic and hypoxic genes, but it is unlikely that transcription control plays an important role in changes we observed in phosphate metabolism since they are too rapid.

Acknowledgement

References

1. Cerdá-Olmedo E, Lipson ED (1987). Phycomyces. Cold Spring Harbor Laboratory Press, New York
2. Veiga A, Arrabaça JD, Loureiro-Dias MC (2003) J Appl Microbiol. 95(2):364-71
3. Vagabov VM, Trilisenko LV, Shchipanova IN, Sibeldina LA, Kulaev IS (1998) Microbiol. (Moskow) 67:154-157
4. Kulaev I, Kulakovskaya T. (2000) Annu. Rev. Microbiol. 54:709-734
5. Sutter RP (1975) Proc. Natl. Acad. Sci. USA 72:127-130
6. Shelemekh OV, Heidebrecht OV, Plakunov VK, Belyaev SS (2006) Microbiol. 75:486–493
7. Živić M, Zakrzewska J, Žižić M, Bačić G (2007) A Van Leeuw J Microb. 91(2):169 177
8. Freimoser FM, Hürlimann HC, Jakob CA, Werner TP, Amrhein N (2006). Genome Biology 7(11) Article R109
9. Beauvoit B, Rigoulet M, Guerin B, Canioni P (1989). FEBS Lett 252:17–21
10. Kwast KE, Burke PV, Staahl BT, Poyton RO (1999) Proc. Natl. Acad. Sci. 96:5446–5451

INTERACTION OF CANCEROSTATIC PERIFOSINE WITH DIFFERENT CELL LINES

Rok Podlipec[1]
Tilen Koklič[1,2]
Janez Štrancar[1,2]
Marjeta Šentjurc[2]

[1] Center of excellence NAMASTE, Ljubljana, Slovenia

[2] Jožef Stefan Institute, Ljubljana, Slovenia

Abstract

In this work interaction of an anticancer agent perifosine (OPP) with OPP resistant, estrogen receptor positive MCF7 breast cancer, OPP sensitive, estrogen receptor negative MT-3 breast cancer, and normal mouse fibroblasts (L-929) cell lines was investigated by EPR, using spin labeled derivative of OPP (5P) as a spin probe, which mimics properties of OPP. The results show that OPP increases membrane fluidity of all cell lines at concentrations higher than 50 µM. The effect is less pronounced for OPP sensitive MT-3. From EPR spectra intensity of P5 immediately after labeling and kinetics of nitroxide reduction by oxy-redoxy systems in cells it was concluded that spin labeled OPP (P5) accumulate the most in MT-3 cells and its transport into the cell cytoplasm is faster for MT-3 as for MCF7 cells. It seems that there are some mechanisms in MCF7 cells which prevent transport of P5 into the cell or expel it from the cell before it gets reduced. These mechanisms could be responsible for the OPP resistance of MCF7 cells. The most sensitive to OPP are L-929 mouse fibroblasts. Their sensitivity to OPP might be correlated with the growth rate of cells, which is far higher in this cell line in comparison to both cancer cell lines

Introduction

Perifosine (OPP) belongs to the group of alkyl phospholipids (APLs), a new class of anticancer agents, targeting directly cell membrane and not DNA. They show a selective apoptotic response in tumor cells, sparing normal cells (1). Anti-cancer mechanisms of alkyl phospholipids have been described and extensively discussed in some recent reviews (1,2,3). Alkylphospholipids have shown promising results in several clinical studies (4) and among them perifosine (octadecyl(1,1-di-methyl-4-piperidinium-4-yl)phosphate OPP) seems to be most promising for breast cancer therapy (5). However, there is a class of breast tumors, mainly those with hormone receptors, which are not sensitive to OPP, while those which lack estrogen receptors seem to be more sensitive to the OPP action. The reason for this difference is not yet understood. To contribute to the understanding of the mechanism of OPP action, in this work influence of OPP on the membrane fluidity of OPP resistant and OPP sensitive breast cancer cell lines was investigated by EPR using spin labeled derivative of OPP (P5). P5 was synthesized recently in our group (6) and was used in this work to get information about the transport of OPP into the cell and to measure accumulation of OPP in cell membrane. The results were compared with those obtained on normal mouse fibroblasts.

Material and methods

Cell lines Human breast cancer cell lines MT-3 (OPP sensitive and estrogen receptor negative (ER-)) and MCF7 (OPP resistant and estrogen receptor positive (ER+)) as well as mouse fibroblasts L-929 were used. MT-3 cells were cultured in RPMI-1640 medium, while MCF7 and L-929 cells were cultured

in DMEM media, all supplemented with 4 μmol/ml L-glutamine, Penicillin-Streptomycin (100 U/ml; 100 μg/ml, Sigma) and heat-inactivated fetal calf serum, (10% FCS, PAA). On the day of the measurement cells were trypsinised in the plateau phase. The cell suspension was centrifuged at cca 400·g and the pellet (5-15·10^6 cells dependent on the size of the cell line, cca 20 μl) was mixed with medium without serum (1 ml). Their viability was checked by Trypan Blue Stain 0.4% and was between 70 – 90 %, in absence of OPP. Furthermore the number of cells in a specimen was calculated after counting using Bürker – Türck's plate.

Spin labeling For EPR measurements cells were spin labeled with spin labeled derivative of OPP (P5) which monitors the membrane properties close to water-lipid interface by a thin film method (7). Different final concentrations of OPP (0, 50 and 150 μM) were deposited on the walls of the tube together with the spin probe.

Electron paramagnetic resonance Spin labeled cell suspension with or without OPP was centrifuged at cca 320·g for 2 minutes and cell pellet was transferred into a glass capillary (1 mm diameter), immediately put in an X-band EPR spectrometer (ELEXSYS-II 500 Bruker, Germany) and the EPR spectra were acquired at 23 °C.

Membrane fluidity changes were obtained by measuring changes in the line-shape of EPR spectra. From the spectra, maximal and minimal hyperfine splitting ($2A_{max}$ and $2A_{min}$) were measured as shown in Fig. 1.A. and effective order parameter S_{eff} was calculated (8). By measuring EPR spectra intensity changes with time after labeling information about the transport of P5, which mimic properties of OPP, into the cells was obtained as well as the accumulation of OPP in cells.

Results and discussion

Viability of cells in presence of OPP Cell viability depends on the OPP concentration. At 150 μM OPP viability of MCF7 cells was the same as without OPP (between 70 - 90 %), for MT-3 cells it decreases for about 20%, while for L-929 cells viability was between 10 and 30%.

EPR measurements EPR spectra of spin probe in the membrane of different cell lines in presence and absence of OPP are presented in Fig. 1A. and the corresponding effective order parameters are presented in Table 1.
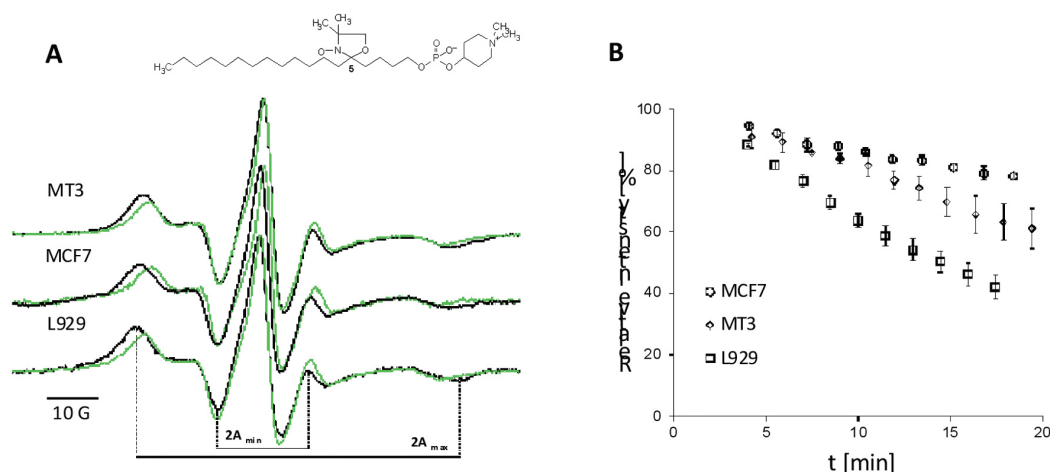
Figure 1. A. EPR spectra of P5 in the membranes of OPP sensitive MT3, OPP resistant MCF7 breast cancer cells and L929 normal mouse fibroblasts in presence of 150 μM OPP (green) and absence of OPP (black) line, measured at room temperature. **B.** EPR spectra intensity decrease of P5 in MCF7, MT-3 and L929 cells measured at room temperature. EPR spectra intensity is presented as a peak to peak height of the middle line of EPR spectra. The data are mean ± standard deviation of three or six measurements.

In presence of 150 mM OPP order parameter decreases in all cell lines. The changes are the highest for L-929 cells and are the less pronounced for OPP sensitive MT-3 cells.

In Table 1 the intensity of EPR spectra measured immediately after labeling are presented as well as

Section S3: Membrane and cell biophysics

the rates of nitroxide reduction due to the oxy-redoxy systems in cells, which reduce nitroxide group of the spin probe to the corresponding hydroxyl amine not visible by EPR (9). The reduction kinetic curves of P5 in the three cell lines are presented in Fig. 1B.

Cell line	S			I_0	Reduction rate $\Delta I/\Delta t$ [%/min]
	0 µM OPP	50 µM OPP	150 µM OPP		
MCF7	0.70 ± 0.01	0.70 ± 0.01	0.61 ± 0.01	2.9 ± 0.3	1.1 ± 0.1
MT3	0.68 ± 0.01	0.67 ± 0.01	0.62 ± 0.01	5.1 ± 0.4	2.1 ± 0.1
L929	0.72 ± 0.01	0.67 ± 0.01	0.64 ± 0.01	2.9 ± 0.2	$3,4 \pm 0.2$

Table 1. *Effective order parameters S of P5 in the membrane of OPP sensitive (ER-) MT-3, OPP resistant (ER+) MCF7 breast cancer cell lines and for mouse fibroblasts L-929 at room temperature for different concentration of OPP and the intensity of EPR spectra of P5 immediately after addition of P5 (Io) and the rates of nitroxide reduction by cells ($\Delta I/\Delta t$).*

One can see that the rate of nitroxide reduction is slower for experimental breast cancer, OPP resistant MCF7 cell as for OPP sensitive MT-3 cells and is the fastest for mouse fibroblasts L929, while the intensity of EPR spectra which is proportional to the amount of P5 in cells show the highest accumulation of P5 in MT-3 cells. It should be stressed that P5 is a spin probe which is structural analogue of OPP. The only difference is the nitroxide group on the alkyl chain. Therefore we assumed that P5 can be used as a model molecule for studying behavior of OPP. Highest accumulation of P5 in MT-3 cell membrane indicates that MT-3 cells are more accessible to OPP as the MCF7 cells. Due to the slower reduction of P5 in MCF7 cell, which is connected with the transport of these molecules into the cell cytoplasm and organelles one can speculate that there are some mechanisms in MCF7 cells which prevent binding of P5 to cell membrane or expel P5 from the membrane before it get reduced. These mechanisms could be responsible for the OPP resistance of MCF7 cells, which show no influence of OPP on their viability. Contrary to our expectations normal mouse fibroblasts are the most sensitive to OPP. The viability of these cells decreases the most and their transport into cells seems to be the fastest. The reason for this still has to be further investigated and might be correlated with the growth rate of cells, which is far higher in these cells in comparison to both cancer cell lies.

References

1. Danker K., Reutter W., and Semini G. 2010, Brit. J. Pharmacol., 160: 36-47.
2. Gills J.J., and Dennis P.A. 2009, Current Oncol. Reports, 11: 102-110.
3. van Blitterswijk W.J., and Verheij M. 2008, 14: 2061-2074.
4. Mollinedo F. 2007, Expert Opin. Ther. Patents, 17: 385-405.
5. Fichtner I., Zeisig R., Naundorf H., Jungmann S., Arndt D., Asongwe G., Double J.A., and Bibby M.C. 1994. Breast Cancer Res. Treat., 32: 269-79.
6. Mravljak J., Zeisig R., and Pecar S. 2005, J. Med. Chem., 48: 6393-6399.
7. Zeizig R., Koklič T., Wiesner B., Fichtner I. and Šentjurc M. 2007, Arch. Biochem. Biophys. 459: 98-106.
8. Marsh D. 1981, in: E. Grell (Ed.) Membrane spectroscopy, Springer, Berlin, 51-142.
9. Swartz H.M., Sentjurc M., Morse P.D. 2nd 1986, Biochim. Biophys. Acta. 888: 82-90.

EPR INVESTIGATION OF FREE RADICAL FORMATION IN RUSTYBACK FERN *(Asplenium ceterach L.)*

Suzana Živković[1]
Ana Popović-Bijelić[2]
Miloš Mojović[2]

[1] *Institute for Biological Research „Siniša Stanković", University of Belgrade, Bulevar despota Stefana 142, 11060 Belgrade, Serbia*

[2] *Faculty of Physical Chemistry, University of Belgrade, Studentski Trg 12-16, 11000 Belgrade, Serbia*

Abstract

Rustyback fern (*Asplenium ceterach* L.) belongs to resurrection plants and may survive long dry periods, passing quickly from anabiosis to full biological activity. The role of phenolic compounds in the ability of these plants to withstand the oxidative stress imposed by free radicals has been investigated by EPR spectroscopy. The level of the reduction of TEMPON free radical has been evaluated showing an increased production of phenolics as a response to higher rates of ˙OH radical formation in fronds. These results implicate an important role of phenolic compounds in the adaptation of the rustyback fern to desiccation process and overall plant resistance to water stress.

Introduction

A group of higher plants known as desiccation tolerant or resurrection plants possess unique effective mechanism to withstand extreme dehydration and rapid rehydration of vegetative tissues without cell damage. Resurrection plants survive the loss of most of their tissue water content until the quiescent stage is achieved. Upon watering, the plants revive and are restored to their former state within 24 h (1). In order to cope with desiccation, resurrection plants have to overcome a number of stresses, among them the most critical being oxidative stress. Plant cells utilize an integrated system of enzymes and a network of low molecular mass oxidants to ensure the efficient protection under stress conditions (2). In our previous investigations we have shown that during the rehydration process ˙OH radicals are produced. In the present study we have tested the possibility of quantifying this production by measuring the rate of the reduction of TEMPONE free radical. The experimental model used in this work were young and old fronds of the rustyback fern (*Asplenium ceterach* L.), one of the rare resurrection species represented in the flora of Serbia.

Material and methods

Plant material Mature sporophytes of rustyback fern (*Asplenium ceterach* L.) were collected in Gornjak, Srbia, and grown in a greenhouse of the Institute for Biological Research "Siniša Stanković", Belgrade, Serbia.

Total phenolics content Plant material was powdered in a mortar with liquid nitrogen and total phenolics were extracted with 80% methanol. After centrifugation at $10000 \times g$ for 10 min at 4^oC, the supernatant was collected and filtered (Econofilter, pore size 0.45 mm, Agilent Technologies, Waldbronn, Germany) before analysis. Determination of total phenolics content was obtained spectrophotometrically at 724 nm, using the Folin–Ciocalteau method (3). The total phenolic content was expressed as gallic acid equivalents (EGA) in mg per g dry tissue weight (DW).

EPR spectroscopy For the EPR spin-trapping measurements, 50 mM nitrone spin-trap 5-diethoxyphosphoryl-5-methyl-1-pyrroline N-oxide (DEPMPO) was added directly on the fronds. For

Section S3: Membrane and cell biophysics

the reduction of the spin-label 2, 2, 6, 6-tetramethyl-4-oxo-piperidin-1-oxyl (TEMPONE), the fronds were incubated in 100 µl of 3.5 µM TEMPONE for various incubation times (1-4 h). The EPR spectra were recorded using a Varian E104-A X-band EPR spectrometer under the following conditions: field center 3410 G, scan range 200 G, microwave frequency 100 kHz, modulation amplitude 2 G (1 G for TEMPONE), microwave power 10 mW, time constant 0.032 s. Experiments were performed at room temperature (22ºC).

Results and Discussion

The production of radical oxygen species during the rehydration of old and young dry fronds (relative water content, RWC ≈ 5%) was investigated by EPR spin-trapping method. Dry fronds in anabiosis (after two weeks of dehydration) give rise to a central EPR signal which could be assigned to the hydroquinone moiety (4). After 1h of rehydration, the central signal has been decreased and the formation of the •OH radical could be detected. Furthermore, after 3h of rehydration time, the most of the central signal was lost and the production of the •OH radical was increased (Fig. 1). The results obtained from the investigated model confirmed that the production of •OH radicals was greater in old compared to the young fronds (results not shown).
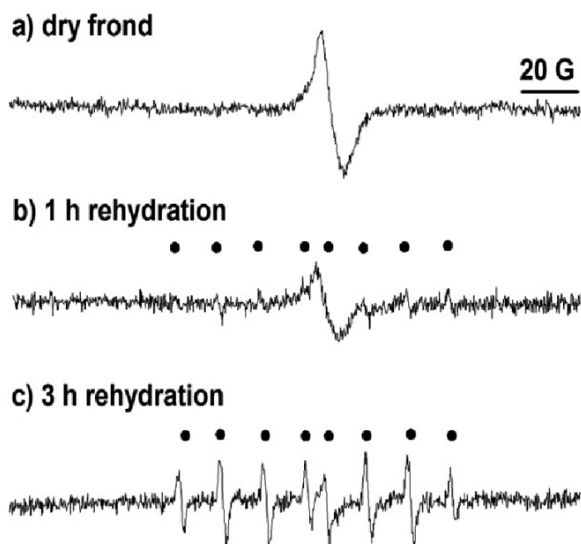
Figure 1. EPR spectra of dry rustyback fronds before rehydration (a), and after rehydration in the presence of the spin-trap DEPMPO (b and c). The characteristic EPR peaks of the DEPMPO/OH adduct are marked with (•).
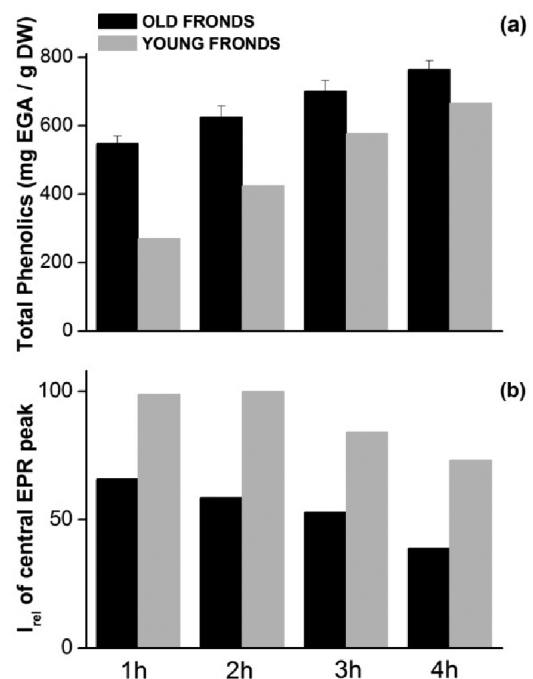

Figure 2. (a) Total phenolics content in fronds of rustyback fern during rehydration; (b) The reduction of spin-label TEMPONE in old and young fronds as a function of rehydration time.

It was shown that the fronds of the rustyback fern sporophyte contain an unusually large amount of phenolics in comparison with other resurrection plants (5, 6, 7). Total phenolics content in fronds significantly increased during rehydration, showing approximately 2.5-fold higher values in young fronds after 4h of rehydration as compared to the first hour of this process. Hence, old fronds generally contained greater amount of phenolic compounds (Fig. 2a). An increase in the synthesis of the phenolics is common response to environmental stress in plants, including water stress (8). Phenolic compounds are excellent antioxidants according to the electron donating activity of the "acidic" phenolic hydroxyl group. They can directly scavenge harmful reactive oxygen intermediates and inactivate them without promoting further oxidative reactions, thus serving specific role in plant protection (9).

The reduction of the hydrophilic spin-label TEMPONE was monitored by EPR spectroscopy as a function of increasing rehydration time in young and old dry fronds (Fig. 2b). The results show decrease of EPR signal intensity with the increasing rehydration time. Moreover, it is observed that the EPR signal of TEMPONE was readily reduced in old compared to young fronds. This confirms the observation that, during the rehydration process, the old fronds produce more phenolics compounds which act as antioxidants, thus reducing the spin-label. The increased production of phenolics as a response to higher rates of ·OH radical formation in fronds implicate an important role of phenolic compounds in the adaptation of the rustyback fern to desiccation process and overall plant resistance to water stress.

Acknowledgements

References

1. Scott P. 2000, Ann. Bot., 85: 159-166.
2. Blokhina O., Virolainen E., Fagerstedt K.V. 2003, Ann. Bot., 91: 179-194.
3. Singleton V.L., Rossi J.A. 1965, Am. J. Enol. Vitic., 16: 144-158.
4. Morina F., Jovanović Lj., Mojović M., Vidovica M., Panković D., Veljović-Jovanovic S. 2010, Physiol. Plant., 140: 209–224.
5. Sgherri C.L.M., Stevanović B., Navari-Izzo F. 2004, Physiol. Plant., 122: 478-485.
6. Farrant J.M., Brandt W., Lindsey G.G. 2007, Plant Stress Glo. Sci., 1:72-84.
7. Živković S., Popović M., Dragišić-Maksimović J., Momčilović I., Grubišić D. 2010, Arch. Biol. Sci., 62 (4): 1071-1081.
8. Dixon R.A., Paiva N.L. 1995, Plant Cell, 7: 1085-1097.
9. Grace S.C. 2005, in Antioxidants and Reactive Oxygen Species in Plants (ed. Smirnoff N.), Wiley-Blackwell, pp. 141-168.

THE MECHANISM OF VANADATE REDUCTION IN PHYCOMYCES BLAKESLEEANUS MYCELIUM

Milan Žižić[1]
Ivan Spasojević[1]
Miroslav Živić[2]
Jelena Bogdanović Pristov[1]
Marina Stanić[1]
Strahinja Križak[1]
Joanna Zakrzewska[3]

[1] *Institute for Multidisciplinary Research, University of Belgrade, Belgrade, Serbia*

[2] *University of Belgrade-Faculty of Biology, Belgrade, Serbia;*

[3] *Institute of General and Physical Chemistry, Belgrade, Serbia*

Abstract

In this study we have investigated the interactions of vanadate (+5) and vanadyl (+4) with mycelium of fungus *P. blakesleeanus* using EPR spectroscopy and biochemical assays. We have determined that *P. blakesleeanus* can reduce V^{5+} to V^{4+} in the extracellular compartment by the cell surface enzyme with ferricyanide reductase activity, containing molybdenum molybdopterin as a cofactor.

42

Introduction

Fungi represent the main route of entrance of vanadium, an essential ultra-trace element (1), into the biotic component of ecosystem (2). They form organic complexes with vanadium, thus reducing its toxicity but retaining vanadium bioavailability (3) that may be particularly important for therapeutic applications of vanadium in treatment of diabetes (4) and cancer (5). In contrary, vanadium may pose an environmental threat due to its toxicity and anthropogenic activity-related increase of its environmental level (6). Surprisingly, data on vanadium metabolism in fungi are scarce and almost exclusively obtained on two ascomycetous yeast species (7). Available data are far from clarifying mechanisms and place of vanadate reduction, vanadium transport, and the active form of vanadium in fungal cells. Another unresolved issue is whether vanadate reduction takes place in the cytoplasm (8) or in the extracellular compartment (9).

The aim of this paper is to provide an insight into the mechanism of vanadium reduction in *P. blakesleeanus*, a filamentous fungus placed near the base of fungal phylogenetic tree, which may have an impact on our understanding of vanadium biological activity. EPR spectroscopy is convenient for such studies as V^{4+} shows characteristic multiple-line spectrum, while V^{5+} is undetectable by this technique.

Material and methods

The wild-type strain of the fungus *P. blakesleeanus* (Burgeff) (NRRL 1555(-)) was used. The mycelium was grown in standard minimal medium (10) in Erlenmeyer flasks which were shaken and aerated, with continuous overhead white fluorescent light of $10W/m^2$, at 20^0C, and ca. 95% relative humidity. In some experiments Fe- or Mo-deficient standard minimal medium was used. For EPR experiments 30mg of 24h old mycelium were treated with sodium orthovanadate at the final concentration of 7 or $35\mu mol/g$ of mycelium fresh weight (FW). For washing experiments 0.3g of mycelium, was centrifuged twice with the experimental medium after V^{5+} treatments, and used in EPR experiments.

SDS or urea was added into mycelium in concentration of 0.5-5% or 6mM, respectively. Potassium ferricyanide was used in concentration of 35µmol/g and $CdCl_2$ of 2 and 20µM/g of FW mycelium. EPR spectra were recorded using a Varian E104-A EPR spectrometer operating at X-band (9.452 GHz): field center 3610 G; scan range 1000 G; modulation amplitude, 10 G; modulation frequency, 100 kHz; microwave power, 10 mW; time constant, 64 ms; scanning time, 4 min, cavity temperature 293K. Mycelium samples were placed on an open Teflon holder allowing free gas exchange. The effects of V^{5+} on ferricyanide reduction were determined using modified method of Baroja-Mazo (11). Mycelium (50mg) was incubated in 1mL of experimental medium with ferricyanide (1mM) and vanadate (0.5 or 1mM) for 20 min at 37^0C. Measurements were performed on supernatants. The level of reduction in V^{5+}-free mycelium was taken to be 100%.

Results and Discussion

The EPR spectrum of *P. blakesleeanus* mycelium supplemented with V^{5+} is presented in Fig. 1A. The signal of V^{4+} has appeared within 5 minutes following vanadate addition, showing lines characteristic for EPR spectrum of vanadyl ions in experimental medium and additional lines which indicate presence of other V^{4+} form(s), *i.e.* bounded V^{+4}. *P. blakesleeanus* mycelium was washed with experimental medium to remove 'free' V^{4+}, making the signal of bounded V^{+4} clearly visible. In this way, it was possible to determine lines in the EPR spectrum that are specific for total (star), 'free' (square) and bounded (circle), V^{4+} (Fig.1).
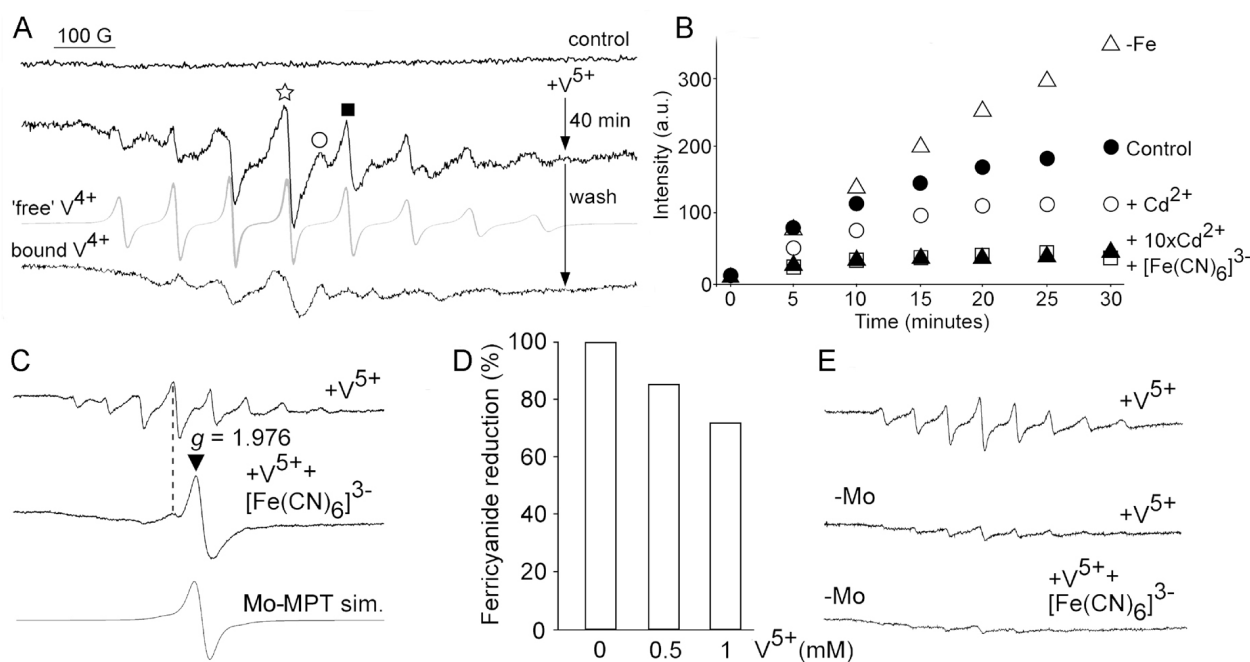
Figure 1. A: EPR spectra of V4+ in the mycelium incubated with V5+ B: time-dependant changes of the amplitude of V4+ signal (star) in V5+ supplemented: mycelium (control), iron-deficient mycelium (-Fe), mycelium with Cd2+ and 10xCd2+, mycelium with ferricyanide. C: comparison of the signal of V4+ in mycelium incubated with V5+ and the signals of mycelium treated with V5+ and ferricyanide and Mo-MPT signal simulation (Mo-MPT sim.). D: the effects of V5+ on ferricyanide reduction. E: V4+ signals in mycelium and Mo-deficient mycelium after incubation with V5+ or V5+ and ferricyanide.

To determine whether the V^{5+} reduction is enzymatic/non-enzymatic process, mycelium was treated with SDS or urea. That results in lost of it ability to reduce V^{5+}, and pointing to enzymatic reduction. Consequently, we have examined the capacities of cell surface enzymes showing ferricyanide reductase activity (FRA) in *P. blakesleeanus* (11) to V^{5+} reduction, by measuring the amplitude of the central line in V^{4+} EPR signal (star, Fig. 1A). The time profiles of V^{5+} reduction clearly imply the involvement of FRA (Fig. 1B). Namely, Fe-deficient mycelium showed two fold higher capacities to reduce V^{5+} than control, which may be related to higher FRA expression (11). In contrast, the

supplementation of Cd^{2+} (FRA inhibitor) provoked concentration-dependant decrease of V^{4+} formation. Almost complete inhibition of V^{5+} reduction was observed at high Cd^{2+} concentrations and in mycelium treated with ferricyanide (the competitor of V^{5+} for reduction). Unexpectedly, mycelium co-supplemented with V^{5+} and ferricyanide showed an additional signal which could not be attributed to V^{4+} or to any organic radical (Fig. 1C). Using MgO/Mn^{2+} external standard, the g-value of the most intensive line was determined to be 1.976, and the signal was identified to originate from Mo^{5+} in Mo-molybdopterin (Mo-MPT) co-factor, according to spectral simulation using parameters: $g = 1.976$ and $A = 33 \cdot 10^{-4}$ cm^{-1} (12). The involvement of FRA with Mo-MPT co-factor in V^{5+} reduction is further substantiated by V^{5+}-provoked inhibition of ferricyanide reduction (Fig. 1D), by drastically decreased capacity of Mo-deficient mycelium to reduce V^{5+} (Fig. 1E), and the lack of Mo-MPT signal in Mo-deficient mycelium exposed to V^{5+} and ferricyanide.

Present study shows that *P. blakesleeanus* has the capability to reduce V^{5+} to V^{4+}. The reduction takes place predominantly in the extracellular compartment and the key enzyme responsible for V^{4+} reduction seems to be FRA containing Mo-MPT as co-factor. The presence of FRA enzyme was shown previously in *P. blakesleeanus* (11), but its biological function remained elusive. This enzyme shows similar features to NAD(P)H nitrate reductase in yeast (13): ferricyanide reduction, NADH as electron donor (11) and Mo-MPT as a co-factor. It is noteworthy that genome of *P. blakesleeanus* has MPT synthase subunit MoaE and oxidoreductase MPT-binding domains. In yeast's NAD(P)H nitrate reductase, cytochrome b transfers one electron at a time to convert the Mo^{6+} of the Mo-MPT cofactor in two 1-electron steps to Mo^{4+} (13). Both of these Mo redox states are EPR-inactive. The presence of EPR-active Mo^{5+} in mycelium co-treated with V^{5+} and ferricyanide implies that the electron transfer to Mo-MPT in the enzyme might be uncoupled under such settings.

Acknowledgement

References

1. Rehder D (2008) Bioinorganic vanadium chemistry. John Wiley & Sons Ltd.
2. Lepp NW, Harrison SCS, Morrell BG (1987) Environ Geochem Health 9: 61-64.
3. Han C, Cui B, Qu J (2009) Biol Trace Elem Res 127:278-283.
4. Thompson KH, Orvig C (2006) J. Inorg Biochem 100: 1925-1935.
5. Bishayee A, et al. (2010) Cancer Lett 294:1-12.
6. Hope BK (1994) Sci Total Environ 141:1-10.
7. Mannazzu I (2001) Ann Microbiol 51:1-9.
8. Zoroddu MA, Masia A (1997) Biochim Biophys Acta 1538:249-254.
9. Bisconti L et al. (1997) BioMetals 10:239-246.
10. Sutter RP (1975) Proc Natl Acad Sci USA 72:127-130.
11. Baroja-Mazo A, et al. (2004) J Bioenerg Biomembr 36:481-492.
12. Burgmayer SJ, et al. (2007) J Inorg Biochem 101:1601-1616.
13. Barbier GG, Campbell WH (2005) J Biol Chem 280:26049-26054.

COMBINED INFLUENCE OF COMPETITIVE BINDING AND MASS TRANSFER ON RESPONSE OF AFFINITY-BASED BIOSENSORS

Ivana Jokić[1]
Katarina Radulović[1]
Miloš Frantlović[1]
Zoran Djurić[2]
Dana Vasiljević-Radović[1]

[1] IHTM – Institute of Microelectronic Technologies and Single Crystals, University of Belgrade, Njegoševa 12, 11000 Belgrade, Serbia

[2] Institute of Technical Sciences SASA, Serbian Academy of Sciences and Arts, Knez Mihailova 35, 11000 Belgrade, Serbia

Abstract

Binding of target and competitor molecules to the functionalized surface of affinity-based biosensors is analyzed, considering also mass transfer processes of both molecular species. It is shown that the mentioned processes have a significant influence on the sensor's transient and equilibrium time response.

45

Introduction

Detection of target biomolecules in solutions is an important task in medicine and environmental protection, while investigation of biomolecular interactions is of great significance for the fundamental biological and pharmaceutical research. One class of biosensors for such applications use surface-based detection methods, where highly specific binding of target analyte to probe molecules (called receptors) immobilized on the sensing surface is converted to the sensor's output signal. The number of bound target molecules determines the sensor's response. Biological samples often contain other molecular species (competitors) which also bind to the same receptors with a certain affinity. For correct interpretation of biosensor response it is necessary to analyze all the processes relevant for generation of the sensor's output signal. The mass transfer (MT) influence on the kinetics of binding of molecules is investigated in (1, 2), while (3) deals with binding of the target and competitor molecules. In this paper we analyze the influence of both competitive binding (CB) and MT on the biosensor response, assuming that the distribution of the analyte concentration in the sensor's reaction chamber can be approximated using the two-compartment model (4). This is typically the case in surface plasmon resonance (SPR), quartz crystal microbalance (QCM) and thin film bulk acoustic resonator (FBAR) sensors (1, 4).

Theoretical considerations

In the affinity-based detection methods it is desirable that only the target molecules bind to the receptors and that transport of the target molecules to the sensing surface is fast compared to the binding reaction speed. Assuming one binding site per receptor and equivalence of all binding sites, a reversible simple one-to-one binding reaction between the target and the receptor molecules is described by the equation:

$$dN_T/dt = k_{fT}\, C_T\, (N_m - N_T) - k_{rT} N_T \tag{1}$$

thus, the number of bound target molecules N_T exponentially reaches the equilibrium value $N_{Te1}=k_{fT}C_T N_m/(k_{rT}+k_{fT}C_T)$ with the time constant $t_T=1/(k_{rT}+k_{fT}C_T)$. Here C_T, k_{fT}, and k_{rT} are the concentration in the sample, the association rate constant and the dissociation rate constant of the target molecules, respectively, and $N_m=n_m A$ is the number of receptors on the surface of area A (n_m is the receptor surface density).

When transport of the target molecules is taken into account, Eq. 1 changes: instead of C_T it contains the concentration of the target molecules in the immediate vicinity of receptors, C_{TS}. In biosensors in which a thin layer depleted of target molecules is formed close to the sensing surface (4), C_{TS} can be determined by the two-compartment model as $C_{TS}=(k_{mT}AC_T+k_{rT}N_T)/(k_{mT}A+k_{fT}(N_m-N_T-N_C))$, where k_{mT} is the MT coefficient of target molecules. Then, the change of the number of bound molecules in time is nearly exponential with the time constant $t_{Tm}=(k_{rT}+k_{fT}C_T+k_{fT}k_{rT}n_m/k_{mT})/(k_{rT}+k_{fT}C_T)^2$ only if $N_{Te1}k_{fT}/(\tau_{Tm}k_{mT}A)<<1$. In other cases, the dependence $N_T(t)$ is determined by the Lambert special function (2).

We analyze the situation when only one species of competitor molecules exists in the sample solution, and we assume: 1) reversible binding reactions between each molecular species (target and competitor) and receptors, without altering any species of reacting molecules, 2) each receptor has one type of binding sites for one molecular species, and all receptors are equivalent, 3) only one molecule can be bound to a receptor at any time. If we include in the consideration the MT of both molecular species through the sample solution to and from the receptor sites, which can be slow compared to the binding reactions, the rates of change of the numbers of bound molecules will then be described by the system of two nonlinear differential equations

$$dN_T/dt = k_{fT}C_{TS}(N_m-N_T-N_C)-k_{rT}N_T \qquad (2)$$

$$dN_C/dt = k_{fC}C_{CS}(N_m-N_T-N_C)-k_{rC}N_C \qquad (3)$$

where N_C, k_{fC}, k_{rC} and C_C are the parameters for competitor molecules, which correspond to previously mentioned target molecules parameters N_T, k_{fT}, k_{rT}, and C_T. Assuming also the validity of the two-compartment model for the competitor concentration, C_{CS} can be expressed as $C_{CS}=(k_{mC}AC_C+k_{rC}N_C)/(k_{mC}A+k_{fC}(N_m-N_T-N_C))$, where k_{mC} is the MT coefficient of the competitor molecules.

If neglecting the mass transfer effect, Eqs. 2 and 3 can be solved analytically, yielding the time evolution of the number of bound target and competitor molecules

$$N_T(t) = N_{Te} + K_I exp(-t/r_I) + K_{II} exp(-t/r_{II}) \qquad (4)$$

$$N_C(t) = N_{Ce} + K_{III} exp(-t/r_I) + K_{IV} exp(-t/r_{II}) \qquad (5)$$

After the transient period, whose duration is determined by the time constants τ_I and τ_{II} ($\tau_{I,II}=2[\tau_T^{-1}+\tau_C^{-1}m((\tau_T^{-1}-\tau_C^{-1})^2+4N_{Te1}N_{Ce1}(\tau_T\tau_C N_m^2)^{-1})^{1/2}]^{-1}$, $N_{Ce1}=k_{fC}C_C N_m/(k_{rC}+k_{fC}C_C)$, $t_C=1/(k_{rC}+k_{fC}C_C)$), the equilibrium is established, characterized by the equilibrium numbers of bound molecules $N_{Te}=N_m k_{fT}C_T/k_{rT}/D$ and $N_{Ce}=N_m k_{fC}C_C/k_{rC}/D$, $D=1+k_{fT}C_T/k_{rT}+k_{fC}C_C/k_{rC}$. The coefficients K_I-K_{IV} are determined by the initial conditions $N_T(0)=N_C(0)=0$ and Eqs. 2-5 must be satisfied for every t. However, if MT is considered, Eqs. 2 and 3 become too complex to be solved analytically. We obtain $N_T(t)$ and $N_C(t)$ by solving Eqs. 2 and 3, numerically.

The biosensor's signal depends on the number of bound molecules of both kind. For example, it can be determined by the total bound mass $m_b=M_T N_T+M_C N_C$ (M_T and M_C are the molecular masses of the target analyte and the competitor, respectively).

Results and Discussion

The presented theory is used for the analysis of the separate influences of CB and MT, and also of their combined effects on the biosensor's response, for the parameter values realistic for biomolecules and biosensors (1-4): $k_{fT}=10k_{fC}=8\cdot10^7$ (Ms)$^{-1}$, $k_{rT}=4k_{rC}=0.08$ s^{-1}, $C_T=C_C/2=1$ nM, $M_T=10M_C=5$ kDa, $k_{mT}=k_{mC}=20$ μm/s, $n_m=1\cdot10^{11}$ Mm, $A=1\cdot10^{-9}$ m^2. Fig. 1a shows the sensor signal (the mass of bound molecules) in time, for four cases. The solid line refers to the case when only the target molecules

exist in the sample and their transport to binding sites is fast ("T only" case). The dashed line corresponds to the binding of two molecular species to the receptors, with neglected mass transfer effects ("CB" case). The dotted line is for the case when only the target molecules bind to the receptors and their MT is taken into account ("MT" case). The dashed-dotted line shows the combined influence of the competitive binding and mass transfer, ("CB+MT" case). The diagram shows that binding of competitor molecules influences both the equilibrium value of the sensor's signal and the transient response. In the "CB" case the total equilibrium bound mass is even lower compared to binding of only the target molecules, and the response rate is also lower. Mass transfer also causes deviation of binding kinetics from the ideal case by decelerating the sensor's response. The combination of CB and MT processes changes the equilibrium value. It also decreases the sensor's response rate more than CB or MT does. Fig. 1b (the parameters that differ from Fig. 1a: $k_{fC}=k_{fC}/100$, $k_{rC}=k_{rT}/8$, $M_C=2M_T$) shows that in "CB" case the equilibrium bound mass can be greater than in the "T only" case. Fig. 1c shows that the time needed for the equilibrium state to be reached is significantly affected by slow mass transfer.
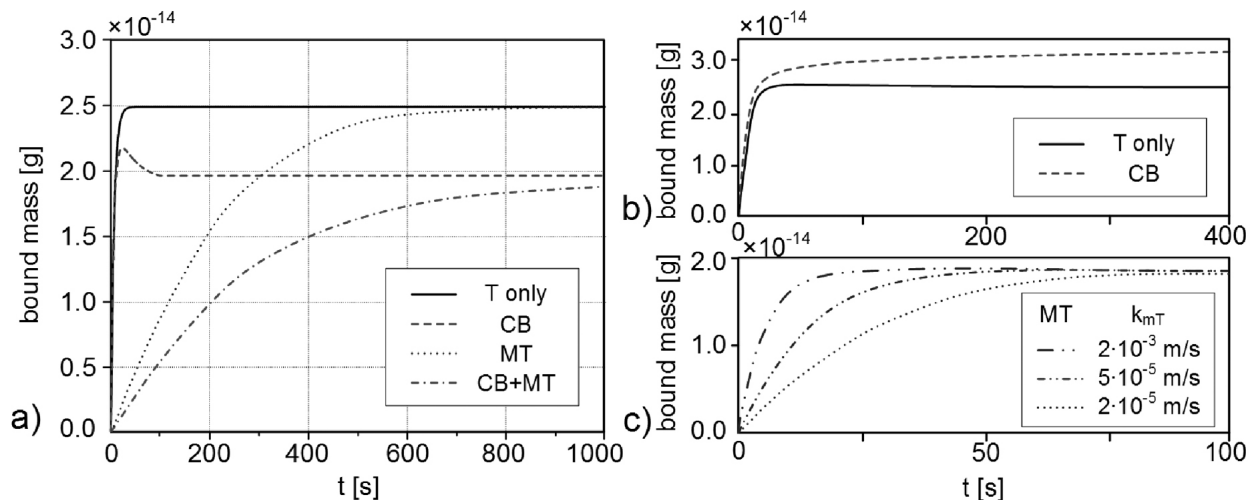
Figure 1. a) *The change of the sensor's signal in time for four different cases,* **b)** *influence of CB on the sensor's response,* **c)** *influence of MT on the sensor's response.*

The presented analysis shows that the influences of CB and MT must be considered in order to correctly interpret the response of affinity-based biosensors when time domain measurements are used for determination of target molecules concentration or for characterization of bimolecular reactions. Apart from its applicability in bimolecular affinity studies and also in investigations of competitive adsorption of biomolecules, the analysis can be used to provide the guidelines for improvement of biosensor sensitivity, selectivity and response rate. It is also useful for development of methods for simultaneous detection of multiple analyte specimens.

Acknowledgment

References

1. Myszka D.G. et al. 1998, Biophys. J., 75: 583-594.
2. Kusznezow W. et al. 2006, Proteomics, 6: 794-803.
3. Karlsson R. et al. 1995, J. Immunol. Methods, 183: 43-49.
4. Jokić I. et al. 2012, Sens. Actuators B, 166-167: 535-543.

47

PERIFOSINE CONTAINING, TRANSCYTOSIS EFFICIENT LIPOSOMES HAVE HIGHER CONTENT LEAKAGE AND RELATIVE PROPORTION OF MICELLES

Tilen Koklic[1,2]
Rok Podlipec[1,2]
Andrea Orthmann[3]
Marjeta Šentjurc[3]
Janez Štrancar[1,2]
Reiner Zeisig[4]

[1] *Jožef Stefan Institute, Ljubljana, Slovenia*

[2] *NAMASTE Center of Excellence, Ljubljana, Slovenia*

[3] *Experimental Pharmakology, Max Delbrück Center for Molecular Medicine, Berlin-Buch, Germany*

[4] *EPO GmbH Berlin-Buch, Germany*

Abstract

Liposomes with high amount of alkylphospholipid perifosine are efficient in transcytotic delivery of liposome encapsulated content. Here we are showing that higher transcytotic efficiency does not depend on increased propensity of liposomes to interact with cells, but is probably the consequence of increased leakage of liposomal content. Perifosine concentration greater than 16 mol % changes liposomal membrane characteristics in a way, which facilitates faster leakage of liposomal content.

Introduction

Transcellular transport of drugs across epithelial or endothelial cells, which form barriers in the vascular systems, glanular tissue or intestine, is of significant importance for drug efficacy in tumor therapy. Designing efficient 'vectors' to deliver therapeutics especially to the disease-affected brain tissue in a controlled and non-invasive manner remains one of the key goals of drug development (1).

It has been shown that membrane characteristics as well as micelle proportion of transcytosis efficient, lysolipid containing liposomal formulations depend mainly on the amount of alkylphospholipid perifosine (OPP). When the amount of OPP is greater than 16 mol% the properties of liposomal membranes change in a way, which should promote leakage of liposomal contents (manuscript sent for publication). On the other hand greater amount of OPP also makes liposomal membrane more fluid, which should promote interaction of liposomes with cells, as it was shown for the interaction of OPP liposomes with breast cancer cells (2). Our main goal was therefore to investigate what distinguishes transcytosis efficient liposomes, either their interaction with cells due to increased membrane fluidity or increased leakage of liposomal content due to different liposomal membrane properties.

Material and methods

The spin probe, (ASL), 4- (N, N - dimethyl-N - (2-hydroxyethyl)) ammonium - 2, 2, 6, 6-tetramethyl piperidine-1-oxyl iodide, were synthesized by Slavo Pečar (Faculty of Pharmacy, University of Ljubljana, Slovenia). Liposomes were prepared by lipid film hydration technology as described before (3). Liposome stability was determined by measuring the leakage of liposome entrapped fluorophore or, in some cases, of a paramagnetic probe, with time after storage of samples at room temperature for several days (4). EPR measurements were performed on an X-band EPR spectrometer Bruker ELEXSYS (2,5).

Results and Discussion

It has been shown previously that transcytosis efficient liposomes L4 have more fluid liposomal membrane than transcytosis inefficient liposomes L3 (4). Although the changers in membrane fluidity were much larger for OPP containing liposomes, which exhibited different propensities of interacting with breast cancer cells (2), it is not unreasonable to expect that L4 liposomes might also more readily interact with barrier forming cells than L3 liposomes. Repeating the experiment of liposome cell interaction by Koklic et al. (2) we have found that there is no difference in interaction of transcytosis efficient versus inefficient liposomes with either MDCK (Fig. 1) or Bend3 cells (results not shown).
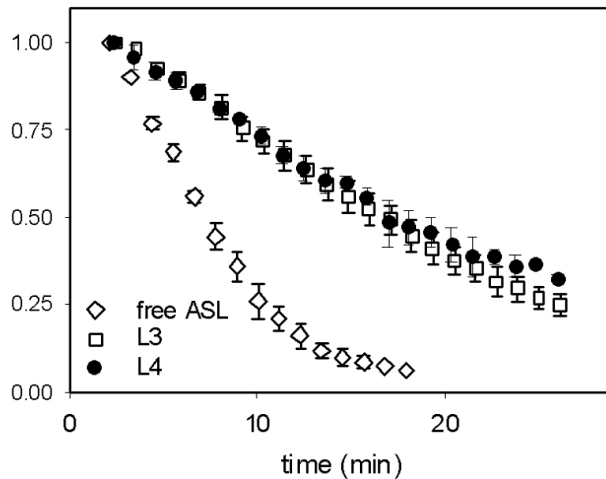

Figure 1. Interaction of liposomes with MDCK cells. Reduction of ASL encapsulated in L3 (open squares) and L4 liposomes (filled circles) and free ASL (open diamonds) measured at 37oC after incubation with MDCK cells. Measurements are the average of 3 (L4) and 5 (L3) independent measurements. Error bars denote standard error of repeated measurements.

On the other side transcytosis efficient liposomes L4 have been shown to leak much more content than liposomes L3 during incubation in serum containing medium (4). We have repeated liposome content leakage experiment in PBS buffer at pH 7.4 at room temperature. Our results show that hydrophilic markers are leaking faster from L4 liposomes (Fig. 2), similarly as it has been shown with solute retention capacity experiments in serum containing buffer (4).
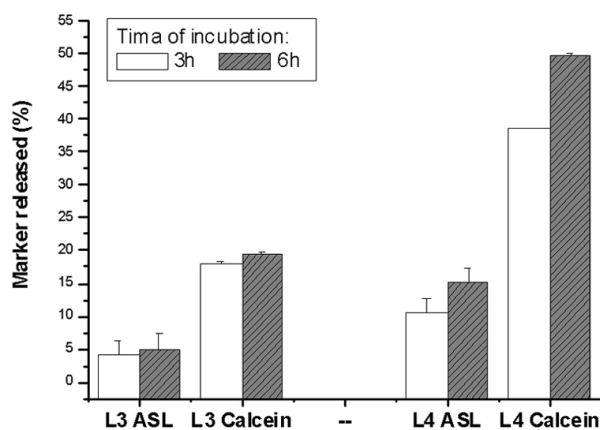

Figure 2. Leakage of liposome contents. Release of ASL or calcein was determined for L3 and L4 liposomes at 2 time points (white – 3 hours, grey – 6 hours) after dialysis at room temperature as described in Material and methods. Given is the mean percentage of released marker +/- S.D. (n=2).

Amount of OPP in liposomal membrane changes liposome membrane properties abruptly at concentrations of OPP higher than about 16 mol%. It was proposed that liposomes with high amounts of OPP should have higher content leakage of liposome encapsulated hydrophilic molecules, since at high concentrations of OPP polarity correction parameter p_A suddenly increases, which reflects more polar environment probably due to deeper penetration of water molecules into liposomal membrane (manuscript send for publication). We have determined leakage of calcein from liposomal formulations with different lipid compositions. It appears that dependence of the leakage of calcein from liposomal formulations on OPP concentration occurs in a similar fashion as liposome membrane characteristics (Fig. 3).
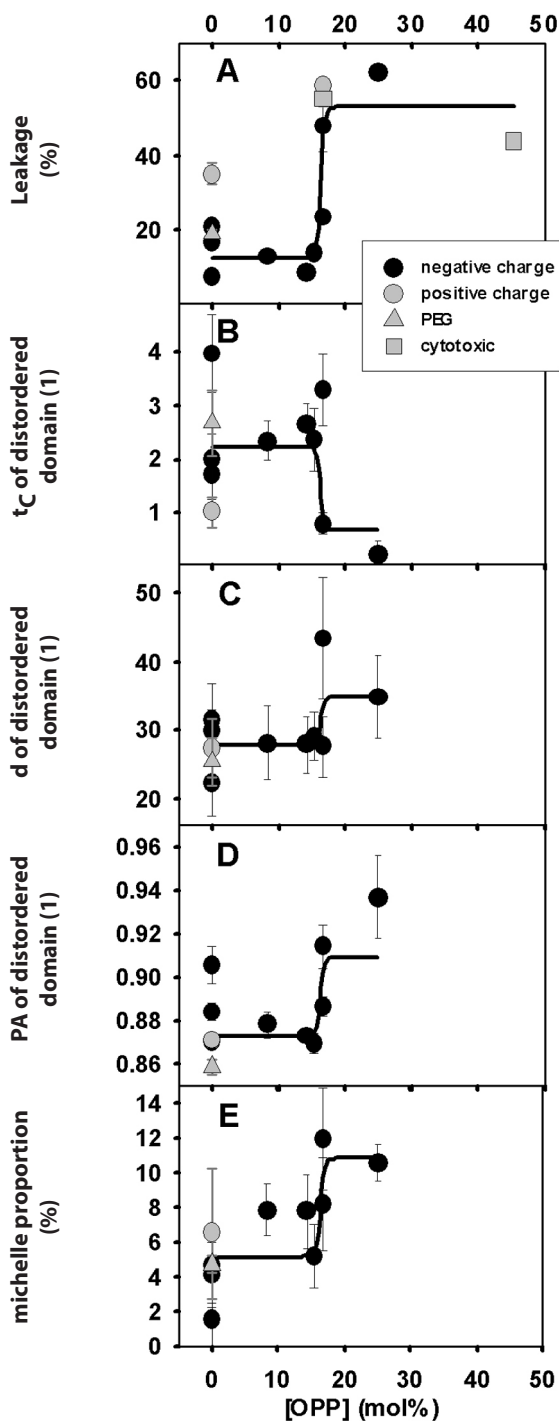
Figure 3. *Dependance of EPR spectral parametres and liposome contents on concentration of perifosine (OPP). A) Liposome content leakage in serum containing medium; B) Rotational correlation time tc of middle domain type; C) relative proportion of disordered domain type; D) Polarity correction parameter of disordered domain; and E) relative proportion of OPP micelles in liposomal formulations. Solid line is global fit of all EPR parameters and the relative proportion of micelles with a sigmoidal function. The global fit (R^2=0.97) yielded two global parameters, the concentration of OPP where transition occurs ($[OPP]_0 = 16.4 \pm 0.5$ mol%).*

Since leaked liposome content doesn't necessarily gets delivered across an endothelial barrier, It remains to be seen whether transcytosis of liposome encapsulated content also correlates with the effect of perifosine on liposome membrane characteristics and liposome content leakage. According to previously published hypothesis free perifosine might simultaneously disturb endothelial barrier integrity as well as promote liposome content leakage (6).

References

1. Karkan D, Pfeifer C, Vitalis TZ, Arthur G, Ujiie M, Chen Q, et al. 2008, PLoS ONE, 3: e2469.
2. Koklic T, Zeisig R, Sentjurc M. 2008, Biochim Biophys Acta, 1778: 2682–2689.
3. Zeisig R, Arndt D, Stahn R, Fichtner I. 1998, Biochim Biophys Acta, 1414:238–248.
4. Orthmann A, Zeisig R, Koklic T, Šentjurc M, Wiesner B, Lemm M, et al. 2010, J Pharm Sci, 99:2423–2433.
5. Koklic T, Šentjurc M, Zeisig R. 2002, J Liposome Res, 2002, 12:335–352.
6. Koklic T, Štrancar J. 2012, BMC Res Notes, 5:e179.

DEPENDENCE OF COLE-COLE IMPEDANCE MODEL PARAMETERS ON GENDER, AGE AND STRATUM CORNEUM LAYERS OF HUMAN SKIN

Jovana B. Simic-Krstic[1]
Srdjan N. Ribar[1]
Mirjana D. Pavlovic[2]
Aleksandar Kalauzi[3]
Lidija R. Matija[4]

[1] University of Belgrade, Faculty of Mechanical Engineering, Belgrade, Serbia

[2] Institute of General and Physical Chemistry,University of Belgrade, Belgrade, Serbia

[3] University of Belgrade, Institute for Multidisciplinary Research, Belgrade, Serbia

[4] University of Belgrade, IC Faculty of Mechanical Engineering, Belgrade, Serbia

Abstract

Individual electrical properties of human skin were determined for 30 women and 30 men aged 23-97 years. Comparative analysis of relationships between Cole-Cole parameters within human population, revealed that: a parameter is strongly related to gender; a is statistically significant higher in women than in men, independent of skin layer and age; parameter R_{∞} (high frequency resistance) is less, but statistically significant related to gender. However, R_0 (low frequency resistance) and t (relaxation time) values are indicative and strongly related to stratum corneum layers.

Introduction

Bioimpedance spectroscopy (BIS) is an elegant and simple non invasive, widely used method for characterizing electrical properties of biological tissue, as well as for medical diagnostics (1, 2). Many of BIS investigations were done on human skin, as an important and easily available organ (2, 5). The most applied model of the electrical impedance properties of human skin is the Cole-Cole model (3), containing four parameters: R_0, low frequency resistance, R_{∞}, high frequency resistance, t, relaxation time and a parameter. Since there are not many data dealing with electrical characteristics of human skin as an object simultaneously dependent on gender, age and layers of stratum corneum, the aim of this paper was to study the distributions of the four Cole-Cole parameters on each of these categories, as well as the differences between them.

Material and methods

Within one experimental method two stainless steel, diameter d=1cm, electrodes are applied. The distance between them was 6 cm. Measurements were performed using Solatron 1255+1280 impedance analyzer at different frequencies ranging between 10 Hz–100 kHz and applying a sinusoidal voltage input of 0.1V. For each of the applied voltage frequencies, impedance amplitude and phase were routinely obtained. Measurements was performed at room temperature (22ºC), within human population of 60 subjects (30 male and 30 female), aged 23-97 years. Removal of three layers of stratum corneum was performed by applying and stripping the adhesive tape three times. BIS measurements were carried out at each frequency in the range 10 Hz – 100 kHz. Cole Cole parameters were calculated as described in ref (4).

Results and Discussion

The influence of each of the categories on each of the four Cole-Cole parameters is statistically analyzed by its mean ± sd and median values. Distributions of α, R_∞, R_0 and τ parameters, related to distinct category subject groups, are shown as box plots in Figs. 1-4, respectively. One-way ANOVA performed on four categories of female groups: older, younger, intact skin (denoted as loc 1) and skin after removal of three stratum corneum layers (loc 3) showed that there were no statistically significant differences of parameter α between them, since $p>0.05$. The same result ($p>0.05$) was obtained when one-way ANOVA was applied to four categories of male skin. However, parameter α was found to be highly significantly different between genders, $p<<0.00001$, $F=234$, when data for each gender were pooled separately (Fig. 1). a values for women and for men were completely separated (higher in females), independent of skin layer or age, visible also from positions of the box plots in Fig.1.
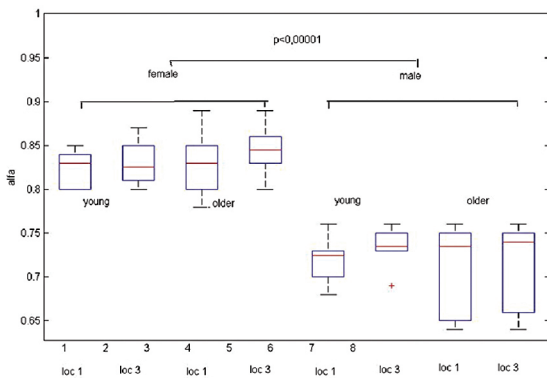

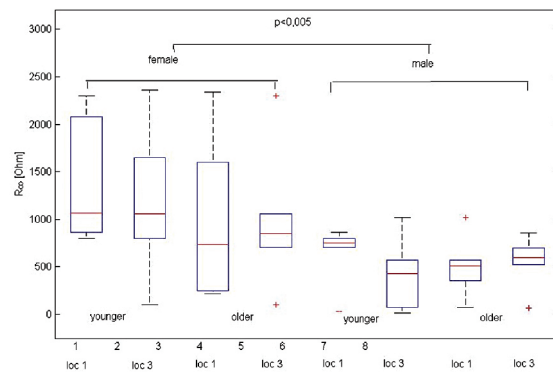**Figure 1.** *The box plot of distribution of α Cole-Cole parameter.*

Figure 2. *The box plot of distribution of R_∞ Cole-Cole parameter.*

Analogous results were obtained for parameter R_∞ - significant difference was found between genders (higher in women, $p<0.005$, $F=13.49$). R_∞ values for women and for men were not completely separated as in case of a (Fig. 2).

Parameter R_0 exhibited a different behavior: one-way ANOVA showed a significant difference when applied on females and males separately (pf=0,040; F=3.27; pm=0,004; F=6,5), while there was not a significant difference between the genders (p=0,052; F=4,1). However, here the R_0 values were significantly different between the intact skin and after stripping of stratum corneum. Post-hoc tests performed on four pairs of data (loc 1 vs. loc 3) for each of the male and female groups resulted in different R_0 values (Fig. 3). Parameter R_0 was found to be decreased after stratum corneum stripping, in both genders and in both age groups. More, when data reffering to loc 1 and loc 3 were separately pooled from all possible groups of tested individuals (female, male, younger and older), the difference was found to be significant: $p<0.0005$, $F=20.62$.
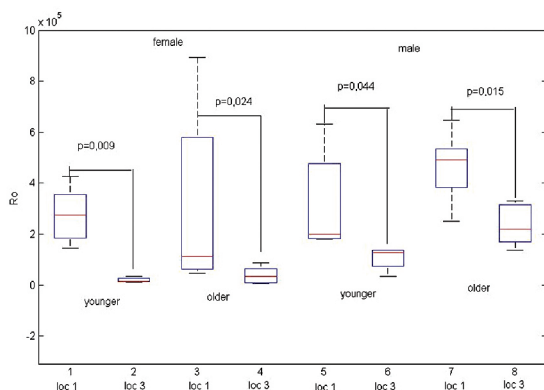

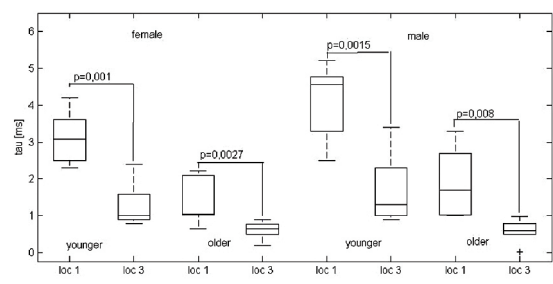**Figure 3.** *The box plot of distribution of R_0 Cole-Cole parameter.*

Figure 4. *The box plot of distribution of relaxation time τ Cole-Cole parameter.*

Finally, parameter τ was also significantly decreased after stripping of three layers of stratum corneum (Fig. 4). Again, separate pooling of data for loc 1 and loc 3 from all groups of individuals

(female, male, younger and older), resulted in significantly different values of the parameter: $p < 0.00009$, $F = 24.88$.

Our measurements of parameters α, R_∞, R_0 and τ, yielded values in the range reported by other authors (1,2,5). In our view, we are the first to report the distribution of the four model parameters within the studied categories of human population. More, we report a grouping of these parameters according to their statistical behavior: α, and R_∞ depended on gender, while R_0 and τ were strongly related to skin layer. Although it is difficult, at this point, to link our results to actual underlying biophysical and biochemical processes, it would be interesting to determine or mathematically model a quantitative relationship between the grouped parameters, which may in turn, if found to be different, be used for detecting various pathological states.

In perspective, our results could serve as a basis for potential noninvasive and low cost diagnostic methods, since determining of the corresponding electrical properties of human skin in a healthy population must preceded such future developments.

Acknowledgements

References

1. Kyle, U. G., Genton, L., Lukaski, C., Dupertuis, Y. M., Slosman, D. O., Hans, D. And C. Pichard, 2005, Nutrition, 21: 161-169.
2. Grimnes, S., and OG. Martinsen, 2008. Bioimpedance and bioelectricity basics. Academic Press.
3. Cole, K. and R. Cole, 1941, J. Chem. Phys, 9: 341-351.
4. Elwakil, A. S., and B. Maundy, 2010, Electronic Letters, 46: 1367-1368.
5. Qiao, Z. G. and L. Merkrid, 1995, Med Bio Eng Comput., 33: 464-470.

BIOINFORMATICAL AND MATHEMATICAL COMPARATIVE ANALYSIS OF CLPP EXONS AND PROTEIN SEQUENCE

Stefan Prekovic[1*]
Dragana Lovren[2]
Bojan D. Petrovic[1]
Uros Lukic[3]

[1] *Faculty of Biology, University of Belgrade*

[2] *Faculty of Mathematics, University of Belgrade*

[3] *Innovational centre of Faculty of Mechanical engineering, University of Belgrade*

* *stefan.prekovic@gmail.com*

Abstract

Much attention has been focused on the study of heat shock response as it is one of the most important features for cell survival. A total of five ClpP gene sequences with the complete coding regions (CDS) and corresponding amino acids belonging to five different species were analyzed, and the differentiation among the species was also studied. The results showed that there are major variations present when it comes to stop codons. The length of the ClpP complete CDS varies greatly, from 588 to 834 bp, due to deletion, insertion, and stop codon mutation resulting in elongation. We determined that much of the gene sequence is conserved among species, with a total of four conserved regions (which is reasonable due to an important function of the gene product, exposed to a strong selective pressure). On the other hand, differentiation of the ClpP gene was obvious among species, and the clustering result was consistent with the taxonomy available in the National Center for Biotechnology Information. Amino acid frequency analysis showed that ClpP are Ser-Arg rich proteins. Overall, our research showed that ClpP CDS can be used as a strong diagnostic marker for species cognation.

Introduction

ATP-dependent Clp protease (ClpP) proteolytic subunit is an enzyme that in humans is encoded by the ClpP gene. Found in mitochondria, it serves to hydrolyze proteins into small peptides in the presence of ATP and Mg^{2+} (1). The protein itself is transported into mitochondrial matrix and is associated with the inner mitochondrial membrane (2). This protein is very important in mitochondrial unfolded protein response. To our knowledge there was no research conducted to determine protein sequence divergence and convergence. In this work we analysed sequences of 5 species of Animals, since there is no sequence data available for any other representative of another kingdom. *Homo sapiens*, *Mus musculus*, *Drosophila melanogaster*, *Danio rerio* and *Ciona savignyi* were analysed for similarity in: DNA sequence, conserved regions, site entropy, substitutions, as well as amino-acid sequence.

Matherial and methods

A total of 5 sequences with the complete CDS of the ClpP gene and the amino acid sequences belonging to 5 species were obtained from GenBank and Ensemble (Table 1). All the sequences were aligned using the Clustal W program implemented in BioEdit (version 7.0.5). DnaSP software (version 4.0) was used to analyze the haplotype diversity (H_d), the average number of nucleotide differences (Tajima 1983), the nucleotide diversity (p), synonymous nucleotide diversity (p_s), nonsynonymous nucleotide diversity (p_a) with the Jukes and Cantor correction, the polymorphic site (S), the singleton

variable sites (SP), and the parsimony informative sites (PIP) for each species, and the average number of nucleotide substitutions per site between species (D_{xy}) [3]. The phylogenetic tree among species based on the D_{xy} was constructed using the unweighted pair group method with the arithmetic mean (UPGMA) implemented in Mega 3.1 software.

Species	Sequence length [bp]	Acccession #
H. sapiens	834	GenBank 12162.1
M. musculus	819	GenBank 28920.1
D. melanogaster	726	Ensemble FBtr0080000
D. rerio	801	Ensemble ENSDARG00000020679
C. savignyi	588	Ensemble SINCSAVT00000002070

Table 1. *ClpP sequence data for all the species analysed.*

Results and Discussion

Polymorphic sites Polymorphic site analyses gave these results: there is a total number 893 sites and there are 305 sites with alignment gaps or missing data. From those remaining, 261 are invariable (monomorphic) and 327 are polymorphic sites, including the parsimony-informative sites, counted at 124 overall.

DNA polymorphisms Variance of H_d (V_{Hd}) was calculated to be 0.016 with standard deviation of H_d (SD_{Hd}) being 0.126. Average number of nucleotide difference (K) is 190.9, while stochastic variance of K ($V_{st}K$) is 5973,773 (without recombination), but with free recombination total V_{Hd} was calculated to be 95.45, while total $V_{st}K$ was 63.633.

Conserved DNA regions Net number of sites analysed was 752 with the sequence conservation (C) being 0.383. Minimum window length was 73 bp and conservation threshold 0.48. Four regions were found to be conserved (Table 2).

Region frame [start-end]	Sequence [AA]	C	H	P
160-236	YNYGVRVYHKYMMVCTSRTHCCHWTNGTKRTVGARCARACBGG NMGMGGNGAGCGBRCHTAYGAYATHTWYTCRMGD	0.481	0.680	0.0425
165-272	RVYHKYMMVCTSRTHCCHWTNGTKRTVGARCARACBGGNMGM GGNGAGCGBRCHTAYGAYATHTWYTCRMGDYTGYTKMRRGARM GHATHRTBTGYBTHATGGSHMMB	0.481	0.690	0.0157
201-280	GGNMGMGGNGAGCGBRCHTAYGAYATHTWYTCRMGDYTGYTK MRRGARMGHATHRTBTGYBTHATGGSHMMBRTHRMYGA	0.496	0.708	0.0163
354-631	TAYWWYAAYWSSMCHRGHGGTRYDGTNACNKCKGGHYTKGCVA TMTAYGAYACNATGCARTWMRTCMWVHVHCCSRTHKSHACNTG GKKHGTKGGNCARGCHDSCWSBATGGGMWSYYTSCTBCTVKCB GCHGGHRVHSCNGGMMTKMGVHAYKCVCTVCCBAAYKCSMGD ATHATGRTVCAYCARCCYTYWGGWGGHGCVMRDGGCCARGCV WCAGAYATHSYHATHCADGCWRAKGARATYMWVAARVTVAARV RVMAGMTVWMYAAMWTSTAYDB	0.500	0.709	0.0010

Table 2. *Conserved regions. C – conservation, H – homozigosity, P – nucleotide diversity.*

Substitution analysis Substitution analysis was done using the methods provided by Nei and Tamura [4, 5] (results are not shown but are later discussed).
*Amino acid frequency:* Amino acids appear at different frequencies among species (Table 3).
Position entropy: Position entropy analysis (PE) was given in Graph 1.
Phylogenetic tree Phylogenetic tree obtained with UPGMA method is shown in Figure 1.

All frequencies are given in percent.	AMINO ACID																			TOTAL
SPECIES	Ala	Cys	Asp	Glu	Phe	Gly	His	Ile	Lys	Leu	Met	Asn	Pro	Gln	Arg	Ser	Thr	Val	Trp	Tyr	
H. sapiens	12.22	4.82	0	0.37	1.48	4.44	0.74	0.74	0.74	5.93	1.48	1.48	13.7	4.07	13.7	17.4	9.26	2.59	4.44	0.37	100
M. musculus	10.23	5.3	0.76	2.65	0.76	3.79	1.14	1.89	1.89	8.33	1.52	1.14	9.47	3.4	12.12	15.53	8.33	4.17	5.68	1.89	100
D. rerio	6.32	2.77	1.98	4.35	4.35	3.16	3.56	3.16	1.98	11.86	2.37	2.37	7.12	4.74	9.49	13.04	7.51	4.35	5.14	0.4	100
D. melanogaster	9.92	5.37	1.65	0.83	2.07	1.65	1.24	2.89	4.13	9.09	0.41	2.07	10.33	2.89	12.4	12.81	9.92	4.13	3.72	2.48	100
C. savignyi	3.93	5.62	1.69	3.37	3.93	3.93	3.93	7.3	8.43	13.48	2.81	5.62	5.62	5.06	5.62	3.93	6.18	4.49	3.37	1.69	100
AVERAGE	8.86	4.72	1.22	2.24	2.4	3.4	1.99	2.9	3.07	9.44	1.66	2.32	9.53	3.98	11.02	13.17	8.37	3.89	4.56	1.33	100

Table 3. Amino acid frequency analysis.
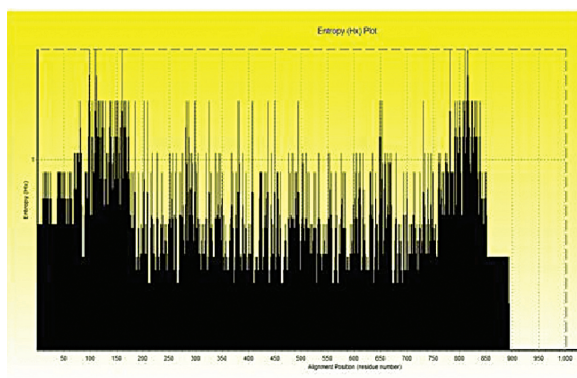
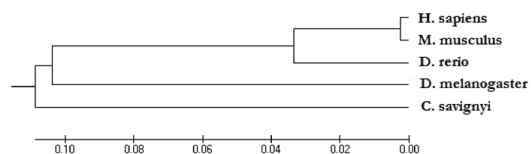**Graph 1.** PE. X-axis – alignment position, Y-axis – entropy (H_X).

Figure 3. The phylogenetic tree.

It is quite obvious that taxa with close relationships according to the classification in NCBI have a similar length of the ClpP gene CDS. The variation in length among species possibly results from evolution and differentiation by accumulating diverse mutations. We could not mathematically determine and characterize distinct differentiation of the species based on the genetic diversity of the ClpP gene, but conventional UPGMA-based phylogenetic tree can be constructed based on the differences in ClpP gene CDS (Figure 1), showing a sharp congruence with the NCBI taxonomy data. It would be interesting to do an analysis of genetic diversity within species and compare those results to the ones of the diversity among species, as in the work of Kang et al [6]. Among all the possible nucleotide substitutions, data obtained by 24 different models (results not shown) confirm that the rates were distinctively higher for the following types of substitutions: A→T/T→A, C→G/G→C, C→A/T, G→A/T. Furthermore, some of these models suggest that of all the particularized, C→G/G→C is the most evolutionary significant nucleotide substitution type. There are four conserved regions within the ClpP CDS (Table 2), with last one (which spans between 354 and 361 nt) having the greatest degree of conservation and least degree of deviation from the consensus. It must be emphasized that all the conserved regions detected share a similar conservation level, probably because all of them equally contribute to the function of the gene product. ClpP peptides are richest with Ser and Arg (Table 3). This is in accordance with the localization ClpP (mitochondrial matrix) but most likely not in support to the specific function of the ClpP (none of these amino acid residues is required for proteolysis). Reasons why ClpP is Ser-Arg rich are to be further examined. Chaos analysis (PE by H_X) as a measure of significance of amino acid appearance at a specific position within the peptide showed that almost all disorder is clustered in C- and N-termini, while the middle of the amino acid sequence is less chaotic.

References

1. Kang SG, Dimitrova MN, Ortega J, et al. (2005) J. Biol. Chem. 280(42): 35424–32.
2. Kang SG, Maurizi MR, Thompson M, et al. (2005) J. Struct. Biol. 148(3): 338–52.
3. Lynch M, Crease TJ (1990) Mol Biol Evol. 7: 377–94.
4. Nei M. and Kumar S. (2000). Molecular Evolution and Phylogenetics. Oxford University Press, New York.
5. Tamura K, Peterson D, Peterson N, et al. (2011) Mol Biol Evol. 28: 2731-9.
5. Kang J, Li X, Zhou R, et al. (2008) Biochem. Genet. 46: 312-22.

ANALYSIS OF REAL-TIME PCR KINETICS BASED ON SINGLE CHANNEL FLUORESCENCE AND FACTOR ANALYSIS

Aleksandar G. Savić[1]
Katarina K. Jovanović[2]
Radmila Janković[2]
Siniša Radulović[2]
Slađana Z. Spasić[1]
Ksenija Radotić[1]

[1] Institute for Multidisciplinary Research, Department for Life Sciences, University of Belgrade, Kneza Višeslava 1, Belgrade, Serbia

[2] Institute for Oncology and Radiology of Serbia, Department of Experimental Oncology, Pasterova 14, Belgrade, Serbia

Abstract

Older Real-Time PCR devices are often equipped with single channel excitation/emission filter and single fluorescent kinetics curves are obtained for each reaction. These results could be analyzed by application of factor analysis with oblique promax rotation and high kappa values. Small differences in reaction efficiency can be successfully detected in such manner. It is also possible to recognize multiple mutation events by comparing the coefficients of linear combinations of factor scores. As the example for diagnostics improvement based on described method, deletions in EGFR gene were analyzed. Analysis of mutations in EGFR is important for proper choosing of therapy for patients with lung adenocarcinomas because treatment depends of presence or absence of mutations.

57

Introduction

Chemical background of the presented method lays in property of Real-Time PCR kinetics which is different for each multiplied sequence. Kinetic curves can be considered as exponential curves with the different basis. Shape of such curves requires factor analysis with oblique rotation. After testing on simulations and real data, promax rotation with high kappa values (k>14) was the best possible solution. Factor analysis is also capable to detect multiple mutations, which is observable from matrix of coefficients of linear combinations.

Material and methods

Detection of EGFR mutations was performed by using DxS EGFR Mutation Test Kit. This kit enables the detection of the 28 different mutations in a Real-Time PCR Assay based on DxS Scorpions® technology. The most prevalent somatic mutations in the EGFR gene are exon 19 deletions, with 19 different deletions type. By using this kit, it is possible to detect presence of a deletion; however, it is not possible to distinguish different deletions. PCR device used in this paper was ABI PRISM® 7500 PCR instrument (Applied Biosystems Inc., Foster City, CA).

Simulation data set for factor analysis testing was created by using the simple exponential equation which simulates Real-Time PCR kinetics:

$$x_n = x_0 E^n \tag{1}$$

where, denotes the initial concentration of cDNA, is the reaction product quantity in cycle , and is a parameter in the exponential model that defines kinetics. Parameter E has values that differ in real experiments from theoretically supposed value 2.

S4: Modeling and instrumental techniques in biophysics

Four exponential curves were calculated, and vectors x_n were used to build source matrix S. The input data matrix A for factor analysis was calculated according to equation:

$$A = SC \tag{2}$$

where C represents the matrix of coefficients of linear combinations. Matrix size was chosen according to the number of patients used in analysis. Aim of the analysis was to decompose the matrix A to source matrix S_{est} and complementary concentration matrix C_{est}[1].

Promax rotation has been proposed by Hendrickson and White [2]. Main advantage of promax rotation compared to other algorithms is fast computation speed achieved by first rotating to an orthogonal varimax solution in the first step and then the orthogonality of the factors was relaxed for the better fit. Proper settings of parameter kappa directly affect analytical results.

Results and Discussion

Reliability of described method was first tested on simulated data set. Method had proved high reliability in estimation of number of components and the shape of components. Results of analysis performed on simulated data set are presented in Fig. 1.
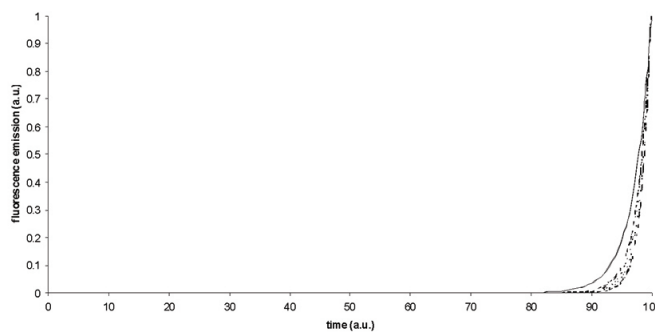

Figure 1. *Factor analysis with promax rotation applied to simulated data set. 3 of 4 components are completely overlapped, and one estimated component is almost overlapped with source component*

After the method has proved the efficiency and reliability on simulated data set, real experimental data were analyzed. Analyzed data matrix has contained 100 Real-Time PCR curves obtained from 100 patients. It was found that 5 types of deletions can be recognized. Without application of described analytical procedure, all 19 deletion types are considered as the single deletion type (Fig. 2).
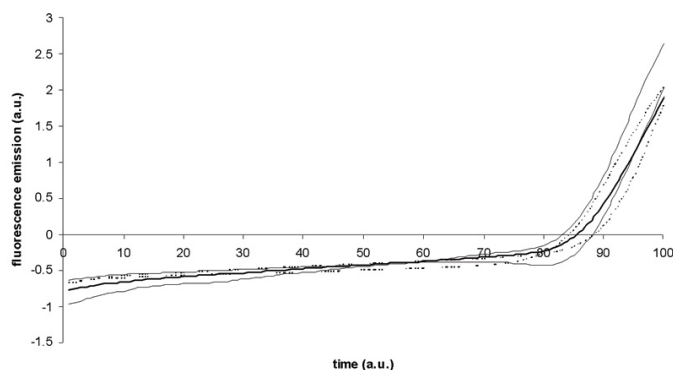

Figure 2. *Factor scores of 5 extracted components from real experimental data for 100 patients*

Conclusion

Factor analysis with promax rotation and high kappa value is an efficient analytical tool which provides distinguishing of real-time PCR kinetics curves. It is possible to use described method both for clusterization of curves with single deletions and decomposition of multi component kinetics curves. In further clinical implementation, patients with different deletions could be monitored during therapy process. Mathematical approach is applicable to any Real-Time PCR kit capable for simultaneous detection of multiple mutations, and it will be tested on other kits.

References

1. Radotić K, Kalauzi A, Djikanović D, Jeremić M, Leblanc RM, Cerović ZG. J. Photochem. Photobiol. B. 2006, 83:1-10
2. Hendrickson EA, White OP. Brit. J. Math. Psy. 1964;17:65-70

ADVANCED ANALYSIS OF MULTI CHANNEL REAL-TIME PCR FLUORESCENCE KINETICS

Katarina K. Jovanović[1]
Aleksandar G. Savić[2]
Radmila Janković[1]
Siniša Radulović[1]
Slađana Z. Spasić[2]
Ksenija Radotić[2]

[1] Institute for Oncology and Radiology of Serbia, Department of Experimental Oncology, Pasterova 14, Belgrade, Serbia

[2] Institute for Multidisciplinary Research, Department for Life Sciences, University of Belgrade, Kneza Višeslava 1, Belgrade, Serbia

Abstract

Real-Time PCR devices equipped with multiple excitation/emission filter sets provide novel possibilities for detection and identification of mutations. Property of fluorophores, that micro environment affects fluorescence spectrum was used for fluorescence emission intensity ratio calculations and clusterization of obtained values. Such method dramatically improves PCR kit capabilities for mutation identification. Method was tested on EGFR gene deletion characterization, and clinical implementation may significantly improve diagnostics and treatment.

Introduction

Development of novel Real-Time PCR kits for mutation detection has provided that multiple mutations could be detected in a single Real-Time PCR run. As the experimental example, in this paper DxS EGFR Mutation Test Kit able to detect 28 different mutations (19 deletions) in a Real-Time PCR Assay was used. Human epidermal growth factor receptor (EGFR/HER1/ErbB1) is mutated in a 10-15% of primary lung adenocarcinomas, and patients harboring EGFR mutations are candidates for targeted therapy, thus described mathematical approach is easy for implementation in clinical studies.

Mathematical approach consider micro environment of the fluorophore. Even small changes in nucleic acid sequence affect the excitation and consequently the emission spectra of the fluorophore. Kinetic curves of Real-Time PCR reactions represent the integrals of emission spectra recorded in time. Ratio calculations of curves obtained with different filter sets provides results similar to ordinary fluorescence experiments performed on spectrofluorimeter [1].

Materials and methods

Detection of EGFR mutations was performed by using DxS EGFR Mutation Test Kit. This kit enables the detection of the 28 different mutations in a Real-Time PCR Assay based on DxS Scorpions® technology. The most prevalent somatic mutations in the EGFR gene are exon 19 deletions, with 19 different deletions type. By using this kit, it is possible to detect the presence of a deletion; however, it is not possible to distinguish between them.

PCR device used in this paper was ABI PRISM® 7500 PCR instrument (Applied Biosystems Inc., Foster City, CA) equipped with 5 excitation/emission filter sets. Three of them were suitable for application in detection of mutations in described kit.

Let's consider kinetic curves for each filter set as the integral of fluorescence emission after passing through the filter F_i defined by:

60

$$F_i = \int_a^b f_i(t)dt \tag{1}$$

where f_i are emission spectra recordings, *a* and *b*, lower and upper bound respectively. After subtraction of baseline, ratios $R_{1/2}$, $R_{2/3}$, $R_{1/3}$ for all filter sets, at the same time moment, were calculated:

$$R_{1/2} = \frac{F_1(t_1,t_2)}{F_2(t_3,t_4)}, \qquad R_{2/3} = \frac{F_2(t_3,t_4)}{F_3(t_5,t_6)}, \qquad R_{1/3} = \frac{F_1(t_1,t_2)}{F_3(t_5,t_6)} \tag{2}$$

where F_1, F_2, F_3 are filters defined by equation (1), and t_j, $j=1,\ldots, 6$ are boundaries.

In further analysis, we observed every sample as triplet $(R_{1/2}, R_{2/3}, R_{1/3})$. Therefore, such obtained ratios namely triplets were clustered, and each cluster should represent one mutation type, or the group of similar mutations (5).

K-means algorithm was applied for clusterization of obtained triplets of ratios. The task of k-means algorithm is to classify *N* objects into *K* classes, with the condition $K \leq N$ according to minimization of cost function defined as:

$$J = \sum_{j=1}^{N} \sum_{i=1}^{c} \left\| x_j - v_i \right\|^2 \tag{3}$$

x_j – specified patient, v_i – is the centroid of ith cluster, N – total number of patients, c – number of clusters, and $\|\cdot\|$ denotes the norm.

Similar approach is to construct joining tree clusters. For linkage rule, single linkage was chosen, and for distance measurement, Euclidean distances in E^3 were defined according to equation:

$$d(x,y) = \sqrt{\left[\sum_i (x_i - y_i)^2 \right]} \tag{4}$$

where $i=1,2,3$.

Results and Discussion

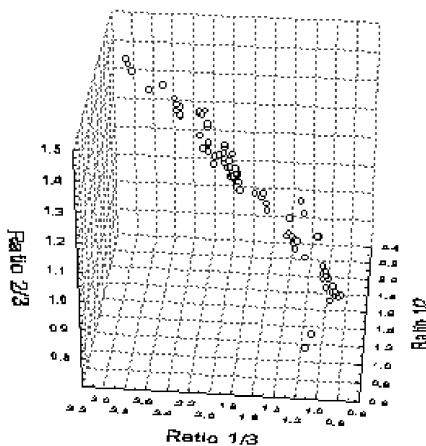Calculated ratio values of fluorescence emission kinetic curves are presented as 3D scatter plot in Fig. 1.

Figure 1. *3D scatter plot with calculated ratio values. It is easy to see that certain values show the tendency to group.*

Analysis of joining tree confirms that the calculated ratio values have the tendency to group. After the joining tree was examined, k-means clustering algorithm was applied to data set. Results have showed that it is possible to resolve at least 9 deletion types. There are no data available from literature what is the rate of occurrence for individual deletions, due to lack of efficient analytical procedure and

availability of patients with mutations in EGFR gene, but some deletions certainly occurs more often than the other. Results of clustering are presented in Fig. 2.
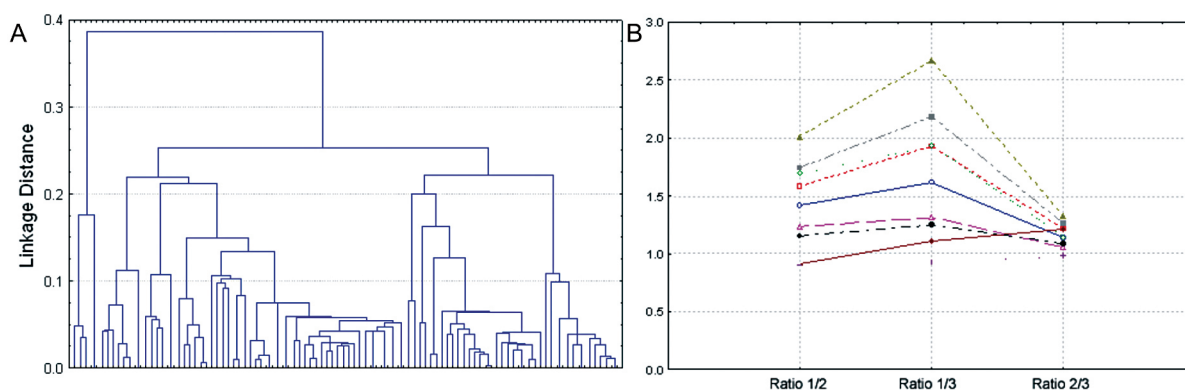

*Figure 2. Clustering results for data set of calculated ratio values. **A:** Joining tree, according to equation 3 **B:** Graph of means after k-means algorithm was applied to the same data set according to equation 2.*

Conclusion

Clustering of kinetics curves ratios enables that full possibilities of Real-Time PCR device and a kit are examined. Described method requires data set that is already recorded during the measuring procedure, and should work well with any other kit capable for multiple mutation detection.

Deletions in EGFR gene were clustered in distinctive groups, unobservable from classically interpreted kinetic curves. In daily medical practice, Real-Time PCR results interpretation is just qualitative, mutations are present or absent. Number of patients was limited to 100 (testing results collected during the period of 2 years), thus method could provide even better clusterization in more groups if the test sample was larger.

References

1. Ladokhin AS. Fluorescence spectroscopy in peptides and protein analysis, in Encyclopedia of Analytical Chemistry, R.A. Mayers, ed., John Willey&Sons Ltd, Chicester, 2000, pp. 5762-5779
2. Djikanovic D, Simonovic J, Savic A, Ristic I, Bajuk-Bogdanovic D, Kalauzi A, et al. J. Polym. Environ. 2012;20:607-17

CALCIUM CHANGES AND CONTRACTIONS OF HUMAN ANTERIOR LENS EPITHELIAL CELLS

S. Andjelić[1]
G. Zupančič[2]
K. Drašlar[2]
D. Perovšek[1]
M. Hawlina[1]

[1] *Eye Hospital, University Medical Centre, Ljubljana, Slovenia;*

[2] *University of Ljubljana, Biotechnical Faculty, Department of Biology, Ljubljana, Slovenia.*

Abstract

The purpose of the study was to characterize the contractions of human anterior lens epithelial cells, which create gaps between cells, and to assess the physiological mechanisms and a possible association of the contractions with free intracellular calcium concentration ($[Ca^{2+}]_i$) changes. Lens capsules obtained during cataract surgery were stained with fluorescent dye Fura-2. Its fluorescence, upon excitation at 360 and 380 nm, was imaged to monitor changes in cell morphology and $[Ca^{2+}]_i$ in response to pharmacological stimulation by acetylcholine (ACh) and to mechanical stimulation by flow of saline or direct contact. Contractions were also studied by scanning electron microscope. Epithelial cells contracted in about a third of preparations after stimulation. Contractions started either before or at best simultaneously with the rise in $[Ca^{2+}]_i$. Contractions also occurred when there was hardly any change in $[Ca^{2+}]_i$ upon application of physiological saline alone. The contractions of the anterior lens epithelial cells occur in significant portion of human lens anterior capsule postoperative preparations. They can be mechanically induced, are localized and reversible, have a fast response and did not differ among different types of cataract. Contractions are at least partially independent of changes in $[Ca^{2+}]_i$.

63

Introduction

Calcium is universal intracellular messenger involved in essential cellular functions and is a key mediator of signalling within lens cells (1). Ca^{2+} homeostasis has a fundamental importance in lens pathophysiology (2). Contractions of lenses and lens epithelial cells were described in isolated chick embryo lenses with coincidence of Ca^{2+} release and contraction (3). Regulation of contractility in non-muscle cells has been assumed to be similar to the smooth muscle cell paradigm – by events leading eventually to a rise in $[Ca^{2+}]_i$ and the activation of myosin via Ca^{2+}-calmodulin mechanism (4). Contractions are often described to be induced by ACh or mechanical stimulation in non-muscle cells. In human anterior lens epithelial cells ACh binds to M1 muscarinic receptors and induces a rise in $[Ca^{2+}]_i$ (1,5).

We have studied the contractions of human adult lens epithelial cells (6) as the lens epithelium is the first physical and biological barrier in the lens and the major role of lens epithelial cells is to act as a regulating barrier between the aqueous humour and the lens fibre cells, protecting the inside of the lens.

Material and methods

Experiments were done on the anterior lens capsule preparations consisting of the monolayer of epithelial cells attached to the basement membrane. The capsules were obtained routinely during cataract surgery and were stained by Fura-2 that is a ratiometric fluorescent dye which binds to free

Ca^{2+}_i. The fluorescence was imaged upon excitation at 360 and 380 nm as the ratio of the emissions at those wavelengths is directly correlated to the amount of Ca^{2+}_i. Stimulation was pharmacological by ACh or mechanical by flow of saline or direct contact. The method was explained in detail previously (7).

Results

Upon the capsule preparations stimulation by the application of ACh, cells from all preparations responded with an increase in $[Ca^{2+}]_i$, while about a third of preparations exhibited epithelial cell contractions. All the observed cells responded to the ACh stimulation with an increase in $[Ca^{2+}]_i$. In most cases the rise in $[Ca^{2+}]_i$ was monophasic, however, we have also observed more complex responses as the one presented in Fig. 1B.
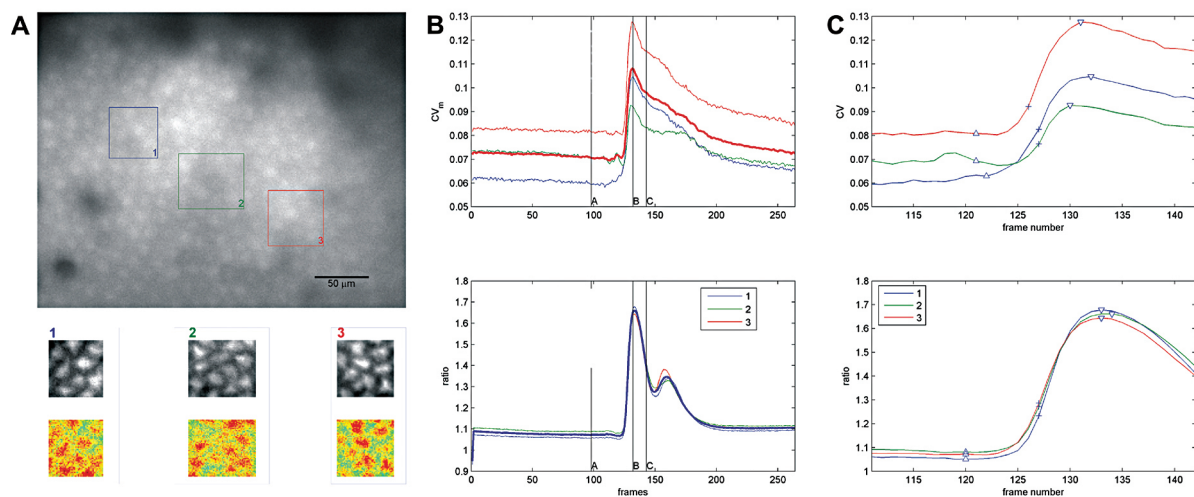

*Figure 1. An example of the human lens epithelial cells contractions upon ACh stimulation. **A:** Human anterior lens epithelial capsule with the epithelial cells stained with Fura-2. Three selected regions of interest (ROI) are shown in different colors and numbers on the top image. The same ROIs are shown on the bottom presenting the contracted cells at the time point B of Figure B, with 360 nm fluorescence in top row and ratio images in bottom row. The values for ratio are color coded with green representing low ratio values and red representing high ratio values. **B:** The colored traces correspond to ROI shown on the Figure A. The time courses of the coefficient of variation, CVm, indicate the changes in morphology and the time courses of the 360/380 ratio are proportional to [Ca2+]i. **C:** Increased region of **B**. Both in **B** and **C**, there are 2 frames per sec.*

When physiological solution was applied alone, without ACh, cell contractions were also induced in about a third of preparations. In these cases there was hardly any change in $[Ca^{2+}]_i$. Direct glass micropipette mechanical stimulation also induced epithelial cells contractions. Although bigger than with physiological saline, the amplitudes of the rise in $[Ca^{2+}]_i$ were smaller than with ACh stimulation. In our experiments, contractions started either before or at best simultaneously with the rise in $[Ca^{2+}]_i$. Contractions also occurred when there was hardly any change in $[Ca^{2+}]_i$ upon application of physiological saline alone. Contractions are localized and reversible and have a fast response.

Discussion

The fact that contractions could be induced not only pharmacologically by ACh but also by the application of the physiological solution and by direct mechanical stimulation suggests that the contractions are, at least in part, induced mechanically and not by the agonist action of ACh. The type of contraction of the lens epithelial cells that we were studying is a fast phenomenon that occurs in the range of few seconds rather than days. Calcium response occurs in the same time range but contractions are at least partially independent of changes in $[Ca^{2+}]_i$. The contractions, which preceded the Ca-responses, were an unexpected finding. The reversibility of the contraction suggests that this is an intrinsic property of lens epithelial cells rather than a defect. It also shows that the epithelial

cells, attached to the capsules, remain functional and that the contractions are not just a consequence of over-stimulation leading to the cell death.

It is currently difficult to determine the actual mechanism behind the observed phenomenon of contractions but there are some important clues. Even though the cytoskeleton of lens epithelial cells includes actin and myosin (8,9), both of which are known to be involved in Ca^{2+}-triggered contractions in other cell types, we can, with some confidence, say that $[Ca^{2+}]_i$ is not directly involved in the changes of the shape of epithelial cells described here. However, antagonist studies will be needed to conclusively confirm this observation.

The functional significance of contractions is not clear but the fact that capsule exhibits functional ACh M1 receptor system and elaborate contraction response to mechanical stimulation is interesting.

References

1. Rhodes J.D., Sanderson J. 2009, Exp. Eye Res., 88:226–234.
2. Andjelic S., Zupančič G., Hawlina M. 2011, J. Clinic. Experiment. Ophthalmol., S1:002. DOI:10.4172/2155-9570.S1-002.
3. Oppitz M., Mack A., Drews U. 2003, Invest. Ophthalmol. Vis. Sci., 44:4813-4819.
4. Goeckeler Z.M., Wysolmerski R.B. 1995, J. Cell. Biol., 130: 613-627.
5. Collison D.J., Duncan G. 2001, Invest. Ophthalmol. Vis. Sci., 42:2355-2363.
6. Andjelic S., Zupančič G., Perovšek D., Hawlina M. 2011, Acta Ophthalmol., 89:e645-e653, 2011.
7. Andjelic S., Zupančič G., Perovšek D., Robič T., Hawlina M. 2010, Zdrav. Vestn. 79:I-123-130.
8. Yeh S., Scholz D.L., Liou W., Rafferrty N.S. 1986, Invest. Ophthalmol. Vis. Sci. 27:1535-1540.
9. Rafferty N.S., Scholz D.L., Goldberg M., Lewyckyj M. 1990, Exp. Eye Res., 51:591-599.

MECHANICS OF INTERACTION BETWEEN CELLS AND TITANIUM NANOSTRUCTURED IMPLANT SURFACE

Doron Kabaso[1,3]
Roghayeh Imani[1]
Samo Penič[2]
Mateja Erdani Kreft[4]
Kristina Eleršič[1]
Ekaterina Gongadze[1]
Šarka Perutkova[1]
Peter Veranič[2]
Robert Zorec[3]
Aleš Iglič[1]

[1] Laboratory of Biophysics, Faculty of Electrical Engineering and Laboratory of Clinical Biophysics, Faculty of Health Studies, University of Ljubljana, Ljubljana, Slovenia

[2] Institute of Cell Biology, Faculty of Medicine, University of Ljubljana, Ljubljana, Slovenia

[3] Laboratory of Neuroendocrinology-Molecular Cell Physiology, Faculty of Medicine, University of Ljubljana, Celica Biomedical Center, Technology Park, Ljubljana, Slovenia

[4] J. Stefan Institute, Jamova 39, 1000 Ljubljana, Slovenia

Abstract

A computational model of the cell attachment is presented in order to study the impact of geometrically structured Titanium surfaces on the cells attachment. Recently, it was demonstrated that the differentiation, adhesion, and spreading of different types of cells like osteoblasts were more favorable on vertically aligned TiO_2 nanotube surface of smaller diameter when compared to larger diameter and to smooth amorphous surface. We propose that the long membrane exvaginations observed on the 100 nm nanotube surface could be due to the small number of focal adhesions. To explain the facilitated osteointegration on the small diameter nanotube surface, a coarse-grained model was constructed, demonstrating the interplay between the negative binding energy of integrin molecules to the edges of nanotubes and the positive membrane bending energy required for membrane protrusive growth. The aggregation and binding of integrins were possible only above the edge regions of the nanotube surface. Using numerical simulations, we revealed that the cell membrane growth and adhesion to the surface occurred only on the small diameter TiO_2 nanotube and not on the large diameter TiO_2 nanotube surface.

Introduction

Orthopedic implants are of immense importance at the end stage of destructive joint diseases like osteoporosis, osteoarthritis and bone tumors. The functional activity of cells like osteoblasts in contact with the biomaterial is determined by the material characteristics of the surface as well as by the surface topography (1-3). Modification of the implant surface is one way to maximize the osseointegration as it involves the growth of bone tissue providing a strong attachment. The surface of the Titanium implant was also modified by a self-assembled layer of vertically
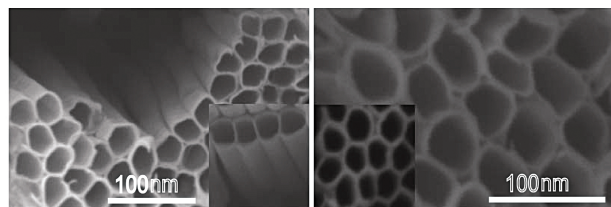

Figure 1. *Electron microscope images of surface of layers of self-assembled vertically aligned TiO2 nanotubes synthesized by anodization method. In preparation we used ethylene glycol solution with 0.3 wt % NH4F and 1% volume water. We used the high-resolution scanning electron microscopy FEG-SEM 7600F from JEOL. Images were taken at 100,000 x magnitude using low accelerating voltage of 2kV.*

oriented TiO$_2$ nanotubes (Fig. 1) with diameters between 15 nm and 100 nm. It was revealed that adhesion, spreading, growth and differentiation of cells depend on the diameter of the nanotubes (4-5). The differentiation of osteoblasts, endothelial cells and smooth muscle cells was greater on a nanotube diameter of 15 nm in comparison to 70-100 nm nanotubes and to amorphous (smooth) TiO$_2$ surfaces. In particular, the formation of focal adhesions was numerous on the 15 nm surface, whereas, the growth on the 100 nm surface lead to the formation of very long membrane exvaginations and weak adhesion. In the present study, we propose that the formation of focal adhesions on the 15 nm surface could be due to the interplay between the negative adhesion energy and the positive bending energy of the plasma membrane. In addition, the long membrane exvaginations on the 100 nm surface could be due to the disassembly of actin filaments and the retraction of the plasma membrane.

Material and methods

To elucidate the dynamics of cell membrane growth on nanorough titanium surfaces (e.g. TiO$_2$ nanotubes), we constructed a model based on the generalized Helfrich membrane free energy, which included the binding energy of integrin molecules to the titanium surface as well as the nearest-neighbour attractive interaction energy between integrin molecules. The intrinsic shape of integrin molecules was taken into account in the spontaneous curvature in Helfrich expression for membrane bending energy. The integrin molecules were assumed to have a positive spontaneous curvature. The free energy expression was employed to derive the equations of motion of an osteoblast membrane contour and integrin density distributions. The present model is an extension of previous theoretical models (6-7). The membrane free energy in our dynamical model was:

$$F = \int \left(\frac{1}{2}\kappa\left(H - \overline{H}n\right)^2 + \sigma_t + \varphi_s h^2 - \omega n_s n - n_s \frac{c\Omega}{2}n^2 + k_B T n_s n \ln(n) + k_B T n_s (1-n)\ln(1-n) \right) dA, \quad (1)$$

where the first term gives the bending energy due to the mismatch between the membrane curvature and the membrane spontaneous curvature due to embedded integrin molecules, κ is the bending modulus, H is the local membrane mean curvature, is the intrinsic mean curvature due to embedded integrins and n is the area fraction density of integrins (relative density). The second term σ_t is Lagrange multiplier (having the units of membrane surface tension) for the conservation constraint of the total membrane area. The third term gives the energy due to force of the cytoskeleton inside osteoblasts, φ_s is the restoring cytoskeleton spring constant. The fourth term is the negative binding potential of integrin molecules (>0). The fifth term describes the direct interaction Bragg-Williams term between neighboring integrin molecules. The sixth and seventh terms are the entropic energies, which take into account the finite areas of integrin molecules.
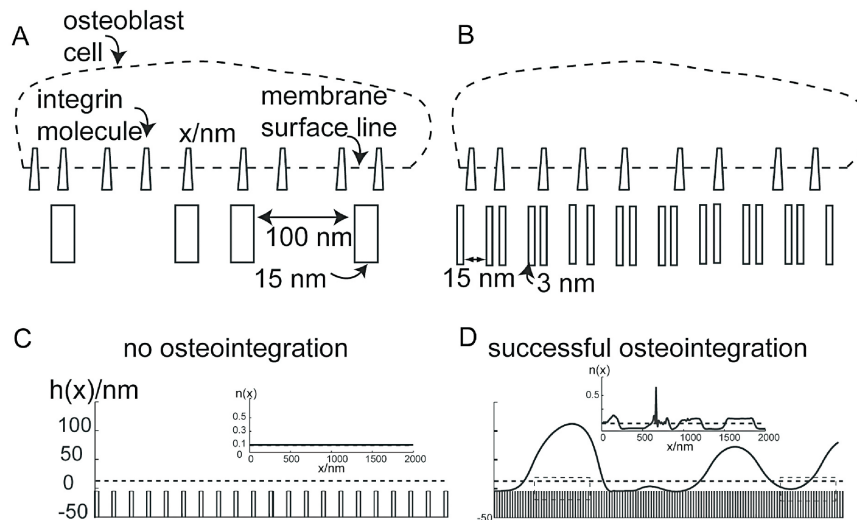

Figure 2. *The effects of nanotube surfaces of 15 nm and 100 nm diameter on membrane adhesion. The modeled membrane segment distributed with curvature membrane components (ie. integrin molecules) is positioned above the 100 nm diameter (A) and the 15 nm diameter (B) nanotube surfaces. Steady state membrane shapes h(x) and integrin density distributions n(x) (see inset) for the adhesion of a n osteoblast membrane to the 100 nm diameter (C) and the 15 nm diameter (D) nanotube surfaces are plotted.*

Our aim was to investigate the effects of TiO_2 surface shape on osteointegration. The TiO_2 surface was modeled explicitly by including a vertical intersection of the 15 nm diameter and the 100 nm diameter nanotube surfaces. The membrane was initially flat, modeled as a segment of the cell (osteoblast) outer contour.

Results

The vertical cross-section of the nanotube is modeled explicitly as a rectangular edge-like profile (Fig. 2). The binding and interaction energies facilitated by the nanotube surface are incorporated into the free energy by having a non-zero integrin binding and interaction potentials above the nanotube edge regions, while above the void regions (i.e. across the nanotube diameter) the binding and interaction potentials are zero. We assumed that the aggregation and binding of integrins could occur only at the top surface of the rectangular profile (i.e. above the edge regions of the nanotube surface). Therefore, the binding constant w and the interaction constant W were of positive value only in membrane regions above the edges of the nanotube surface. Furthermore, it was assumed that membrane regions adhered to the nanotube surface could not be detached to the end of the simulation. According to the diameter of the nanotube surface, the corresponding distances between the edges of consecutive rectangular units were 15 nm and 100 nm. In the following numerical simulations, a random perturbation of small amplitude <1% in the integrin density was added around the initial uniform density of integrin molecules. This perturbation lead to exponential growth only on the 15 nm nanotube surface, whereas, no growth was observed on the 100 nm diameter nanotube surface (Fig. 2).

Discussion

A dynamic model of membrane binding on TiO_2 nanotube surface was constructed to explain the successful osteointegration of cells on vertically oriented TiO_2 nanotubes of 15 nm diameter when compared to 100 nm diameter surface (Fig. 2). The membrane shape dynamics and integrin density distributions were derived from the system free energy (Eq. 1). Results of simulations revealed that the larger number of edges in TiO_2 nanotube surface of 15 nm diameter could be sufficient to drive the membrane protrusive growth, whereas, the small number of edges and the large void regions might restrict the membrane growth on the 100 nm diameter nanotube surface (Fig. 2).

Assuming that the total number of short actin filaments does not change significantly, the anchoring of the reassembled actin filaments to smaller number of focal adhesions could drive the formation of long membrane exvaginations (Fig. 3). To conclude, the present study provided an interesting perspective on the interplay between binding energy and bending energy in osteointegration on nanorough implant surfaces.
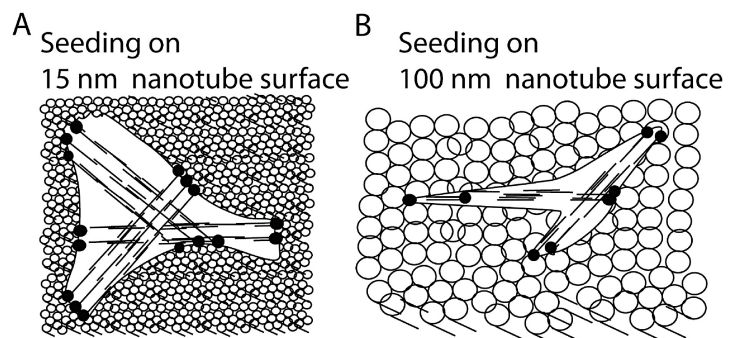

A Seeding on 15 nm nanotube surface

B Seeding on 100 nm nanotube surface

Figure 3. A possible model for the formation of long cell membrane exvaginations on a 100 nm nanotube surface. Note the greater number of focal adhesions (black dots) and stress fibres (broken lines) in a cell on 15 nm (A) than 100 nm (B) nanotube surfaces.

References

1. Stevens MM, George JH. 2005, Science, 310:1135—1138.
2. Matschegewski C, Staehlke S, Loeffer R, et al., 2010, Biomaterials, 31:5729–5740.
3. Gongadze E, Kabaso D, Bauer S, Slivnik T, Schmuki P, van Rienen U, Iglič A. 2011, Int. J. Nanomed. 6:1801-1816.
4. Park J, Bauer S, von der Mark, K, Schmuki P. 2007, Nano Lett., 7: 1686-1691.
5. Park J, Bauer S, Schmuki P, von der Mark K. 2009, Nano Lett., 9: 3157-3164.
6. Kabaso D, Gongadze E, Perutková S, Kralj-Iglič V, Matschegewski C, Beck U, van Rienen U, Iglič A. 2011, Comput. Meth. Biomech. Biomed. Eng., 14:469-482.
7. Kabaso D, Shlomovitz R, Schloen K, Stradal T, Gov NS. 2011, PLoS Comp. Biol., 7:1-13.

THERMAL ANALYSIS OF ACTINIDIN

Sanja Ostojić[1]
Milica M. Grozdanović[2]
Marija Gavrović-Jankulović[2]

[1] *Institute of General and Physical Chemistry, University of Belgrade, Studentski trg 12, Belgrade, Serbia*

[2] *Faculty of Chemistry University of Belgrade, Department of Biochemistry, Studentski trg 12, Belgrade, Serbia*

PROCEEDINGS

Abstract

The digestive properties of kiwifruit extract have generally been attributed to its cysteine protease actinidin. Therefore actinidin could potentially be utilized as a suplement for enhacement of food digestion. The aim of this study was to evaluate the thermal stability of actinidin. Actinidin was isolated from kiwifruit under native conditions. The differential scanning calorimetry of actinidin was carried out on a MicroCal MC-2 (Micro Cal Inc.,USA) differential scanning calorimeter. Thermodynamic parameters of protein unfolding: temperature of transition maximum (T_m), calorimetric enthalpy (DH^{cal}), and van't Hoff enthalpy (DH^{VH}) were estimated. Thermal denaturation experiments showed that native actinidin represents a compact protein structure, with one transition maximum temperature (T_m) at 73.9°C. Due to its thermal stability actinidin can be considered for suplementation of certain food products.

69

Introduction

Actinidin (EC 3.4.22.14) belongs to the family of cystein proteinases and has a wide pH activity range (4-7) and wide substrate specificity. It hydrolyzes most strongly the amide and ester bonds at the carboxyl side of lysine residues (1-3,5). Actinidin shows sequence homology with cysteine proteases such as papain, chymopapain, ficin, and stem and fruit bromelain and is accumulated to very high concentrations in the fruit, where it constitutes up to 60% of soluble protein. Actinidin is encoded as a pre-proprotein with an endoplasmatic reticulum targeting signal peptide and N- and C- terminal propeptides (NTPP, CTPP). The enzyme is likely to be synthesized as a zymogen and further processed into an active form after secretion or sequestration in the cell (6). It consists of a single polypeptide chain made up of 220 residues and has a molecular weight of 23 kDa. The 3D structure revealed that its polypeptide chain is folded into two domains of approximately equal size. Amino acid residues Cys25 and His162 constitute the catalytic ion pair (a cysteinyl thiol-histidinyl imidazole dyad) and are located in the L-domain (residues 19-115 and 214-220), mostly helical in its secondary structure, and the R-domain (residues 1-18 and 116-213), built around a twisted b-sheet, respectively (2,4). The protein is folded in such a manner that a cleft is settled at the surface of the enzyme.

The aim of this work was to ivestigate the thermal stability of actinidin isolated from kiwifruit.

Material and methods

Isolation of actinidin

Actinidin was isolated from the pulp of fresh kiwifruit (*Actinidia deliciosa*, Hayward cv) purchased at a local store, as previously described (7). In brief, a total protein extract was obtained by homogenization of kiwifruit (50 g) in 100 mL of 0.1 M sodium-citrate buffer, pH 5.0. Following extraction (2h at 4°C), the slurry was centrifuged (3000 ´ g, 30 minutes) and dialyzed overnight against the extraction buffer. Purification of actinidin from the obtained protein extract (120 ml) was achieved by a two step ion-exchange chromatography procedure. The first step consisted of step ion-exchange

chromatography on QAE-Sephadex A-50 column (100 mm ´ 27 mm) (GE Healthcare, Uppsala, Sweden), pre-equilibrated with 0.1 M sodium citrate buffer, pH 5.0. The unbound fraction was collected, concentrated and dialyzed against 20 mM TRIS-HCI buffer, pH 8.0. In the second step ion-exchange chromatography on a SP-Sephadex C-50 ion-exchange column (125 mm × 15 mm) (Pharmacia-Biotech, Uppsala, Sweden) was applied. The column was equilibrated in the dialysis buffer and eluted by a pH gradient (from pH 5 to 2.5). A total of 10 mg of actinidin was isolated from 120 ml of the extract. The purity of the protein was estimated to be >97% by N-terminal amino acid sequencing. Following isolation and prior to further analysis, the enzyme was activated in the presence of L-cystein.

Thermal analysis

The differential scanning calorimetry of actinidin was carried out on a MicroCal MC-2 sensitive differential scanning calorimeter (Micro Cal Inc., Northampton MA, USA), using a standard DA – 2 software package for data acquisition and Origin software for DSC data analysis. The non-two-state curve fitting model for estimating thermodynamic parameters of protein unfolding: temperature of transition maximum (T_m), calorimetric enthalpy (DH^{cal}), and van't Hoff enthalpy (DH^{VH}) was used. Scans were performed in the temperature range of 20-90°C with a scan rate of 90°C h^{-1}. To check the reversibility of denaturation, samples were cooled and then reheated with the same scanning rate. Reference baseline, obtained by the buffer-buffer scan, was subtracted from sample endotherm. Protein solutions were degassed with gentle stirring before loading into the calorimeter to prevent bubble entrapment in the cells. For all the experiments a protein concentration of 1mg/ml was used, in 20 mM KH_2PO_4, 52 mM L-Cys, 2 mM EDTA, pH 6.5 buffer solution (buffer A) used for actinidin activation.

Results and discussion

DSC curves obtained for activated actinidin are shown in Fig. 1a and b.
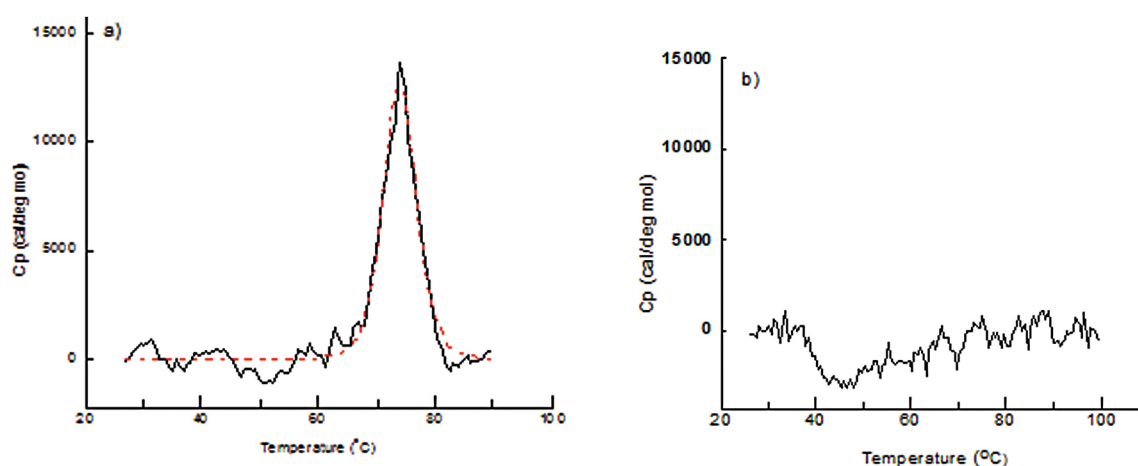

Figure 1. *DSC curves of **a**: activated actinidin (first scan) and **b**: second scan „reversibility". The solid curves represent experimental endotherms while the dashed curves represent the component two-state transitions obtained by deconvolution*

Thermal denaturation of actinidin was studied in buffer A, used for actinidin activation. The obtained temperature of transition maximum (T_m), calorimetric enthalpy (ΔH^{cal}) and Van't Hoff enthalpy (ΔH^{VH}) were: T_m=73.9°C, ΔH^{cal}=94.90 kcal/mol, and ΔH^{VH}=126.77 kcal/mol. The thermal unfolding of activated actinidin, as shown by the DSC endotherm (Fig. 1a), is a highly cooperative process (H^{cal}/H^{VH}=0.75) in the 65°C to 85°C temperature range. This suggests that the L and R protein domains thermodynamically undergo one process (8,9). The process of thermal denaturation of activated actinidin was found to be irreversible, as indicated by the complete absence of an endothermic effect in the second scanning of the sample after rapid cooling (Fig. 1b).

Conclusion

DSC scans of protein thermal denaturation indicated that active actinidin represents a compact protein structure, which according to employed experimental conditions, exibits the temperature maksimum (T_m) of denaturation at 73.9°C. Simple two-state transition can be observed for unfolding of the L and R domains, with the H^{cal}/H^{VH} ratio being close to 1, suggesting that process is a highly cooperative (8, 9) with dominant domain-domain interactions (9).

Actinidin may find an application in the creation of novel functional food products.

Acknowledgements

References

1. McDowall, M.A. 1970, Eur J. Biochem. 14 (2):214-21.
2. Boland, M.J; Hardman, M.J. 1972, FEBS Lett. 27(2):282-4.
3. Baker, E.N. J. Mol. Biol. 1977, 115, 263-277.
4. Varughese, K.I., Su, Y., Cromwell, D., Hasnain, S., Xuong, N.H. 1992, Biochemistry. 31: 5172-5176.
5. Arcus, A.C. 1959, Biochim. Biophys. Acta. 3.3(1): 242-4.
6. Nieuwenhuizen, N.J., Beuning, L.L., Sutherland, P.W., Neelam, N.S., Cooney, J.M., Bieleski, L.R., Schroder, R., MacRae, E.A., Atkinson, R.G. 2007, Functional Plant Biology, 34: 946-961.
7. Grozdanovic, M., Popovic, M., Polovic, N., Burazer, L., Vuckovic, O., Atanaskovic-Markovic, M., Lindner, B., Petersen, A., Gavrovic-Jankulovic, M. 2012, Food and Chemical Toxicology. 50:1013-1018
8. Privalov, P.L. 1980, Pure Appl. Chem. 52 (2):479-49.
9. Sathish, H.A.; Kumar, P.R.; Prakash, V. 2009, Process Biochem. 44:710–716.

POSITIVE EFFECTS OF PHYSICAL AND CHEMICAL PROCESSES ON THE CONTENT OF BIOACTIVE COMPONENTS IN BERRY FRUITS

Mladen Simonović
Miroslava Dojcinović
Sava Hranisavljević
Branislav Simonović

Institute of General and Physical Chemistry, University of Belgrade, Studentski trg 12-16, 11000 Belgrade, Serbia

Abstract

The aim of this work was to introduce some physical processes during the fruit processing in order to obtain the higher content of bioactive compounds in the final products. As the final products, the fruit jellies were chosen, whereby their production was done on two different manners. The first type of jellies was produced with traditional procedure, which included high temperatures and long cooking, and the comparative products described in this paper were made on the contrary in the low temperatures regime and short time intervals. After the jellies were prepared, the polyphenols were extracted with methanol and its content was measured with Folin-Ciocalteau reagent. The results obtained for three kinds of fruits clearly showed the enhancement of total polyphenols content in the new developed products.

Introduction

The berry fruits are thought to be one of the most important sources of phenolic antioxidants (1,2). The health benefits of consuming fruits and vegetables correlate with their high level of phytochemicals, where the phenolic compounds have the greatest ratio. It is now well known, that a diet high in fruit and vegetables reduced risk of some diseases such as cancer, cardiovascular and neurological diseases (3).

The new developed technological concept for fruit processing includes physical and chemical processes, which arise in the operation of freezing and unfreezing of fruits. In the process of freezing, by destructing of cell walls, the contact of biological components is allowed which enter into reaction and give new products. These could be enzyme, non-enzyme reactions and other types of reactions. This reaction system is very complex and cannot allow the complete explanation either theoretical or in praxis. The compounds present in such biological systems are a large number flavonoids, anthocyanins, carotenoides, vitamins, mineral complexes. The content of these compounds is kept in native conditions and is enlarged by using the named biophysical processes.

Material and methods

The fruit used in this paper was raspberry, blackberry and strawberry coming from the regions of Čačak and Arilje, West Serbia. The basic processes used in this technology are spontaneous freezing and unfreezing, separation of native juice from pulp, separation of seeds from pulp, extraction of bioactive components from seed, and concentrating of native juice. The beneficial effects of such procedure were investigated by the measurement of the polyphenols content both in our new products and in traditional made jams. 1 g of each product was mixed with 5 ml methanol and vigorous shaken 10 min at room temperature, 20 µl of extract was taken for the polyphenol analysis. The extract was mixed with 1.58 ml distilled water and 100 µl of Folin–Ciocalteu reagent. Then, 300 µl of 20% Na_2CO_3 solution was added and the mixture was allowed to stand for 30 min at 40 °C. The absorbance was measured at 765 nm. Standard solutions of gallic acid (0-5 mg/L) were similarly

treated to prepare the calibration curve. The amount of total phenolic compounds in the jelly extracts was determined in mg gallic acid equivalent (GAE)/g of original sample, using the obtained standard gallic acid graph (4). The spectral measurements were recorded on Evolution 600 UV-VIS Spectrophotometer, Thermo Corp., USA.

Results and discussion

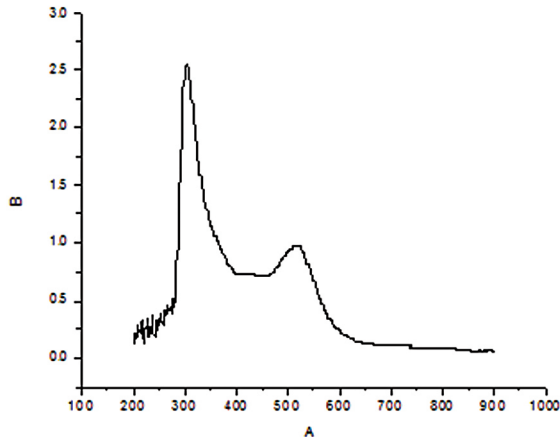First, the methanol extracts jellies were recorded to obtain their absorption spectra (Fig. 1).

Figure 1. *Typical UV-VIS spectra of the methanol extract of one strawberry jelly*

The spectrum yielded most peaks at the wavelengths of 280 nm, 360 nm and 520 nm, which are typical for phenolic compounds, including flavonols, flavanols and anthocyanins. Anthocyanins are the glycosides of anthocyanidins responsible for the attractive colors of fruits and vegetables and have a characteristic absorption wavelength of approximately 500–530 nm (5).

The results obtained from the measurement of the polyphenols content are shown in the Table 1 and Table 2.

Product name	Polyphenols content (mg/g)
Strawberry jelly	2.56
Raspberry jelly	2.09
Blackberry jelly	3.42

Table 1. *The content of the total polyphenols in the products obtained with the new technology*

Product name	Polyphenols content (mg/g)
Strawberry jelly	1.77
Raspberry jelly	1.49
Blackberry jelly	2.55

Table 2. *The content of the total polyphenols in the products obtained with the traditional technology*

From the results shown in these tables one can see, that the new introduced physical processes enhance the content of biological valuable components in the fruit products. The information given in this study should underline the importance of keeping the biological compounds in native conditions. The further investigations can be focused on the impact of physical processes on the biochemical reactions in such biological systems.

References

1. M. P. Kahkonen, A. I. Hopia, M. Heinonen. 2001, Journal of agricultural and food chemistry, 49, 4076-4082.
2. M. R. Williner, M. E. Pirovani, D. R. Guemes. 2003, Journal of the science of food and agriculture, 83, 842-845.
3. B. Halliwell. 1994, The Lancet, 344, 721-724.
4. K. Slinkard, V.L. Singleton. 1977, American Journal of enology and viticulture, 28: 49-55.
5. N. Seeram, R. Lee, H. Samuel Scheuller, David Heber. 2006, Food chemistry, 97: 1-11.

THERMAL BEHAVIOR OF RASPBERRY AND BALACKBERRY SEED FLOUR FOLLOWED BY MDSC

Darko Micić

Sanja Ostojić

Mladen Simonović

Lato Pezo

Milja Dojčinović

Sava Hranisavljević

Branislav R. Simonović

Institute of General and Physical Chemistry, University of Belgrade, Studentski trg 12, 11000 Belgrade, Serbia

Abstract

Modulated Differential Scanning Calorimetry (MDSC) is used to characterize red raspberry (*Rubus ideaus*) and blackberry *(Rubus fruticosus)* seed flours. It is shown that by splitting the total heat flow into reversing (related to heat capacity) and non-reversing contributions (kinetics components), overlapping thermal events in the low temperature region can be separated. It was shown that overlapping thermal events in the low temperature region are not water dependent thermal transitions. Thermal stability from room temperature to 700ºC was followed by Thermo gravimetric analysis (TGA).

74

Introduction

Modulated DSC (MDSC) offers a solution to overcome many of the analytical limitations of conventional DSC. MDSC differs from conventional DSC wherein the sample is subjected to a more complex heating program incorporating a sinusoidal temperature modulation accompanied by an underlying linear heating ramp. It provides the total heat flow, the non-reversible (kinetic component) and the reversible (heat capacity component) heat flows. MDSC nonreversing signal may contain important information on irreversible processes, such as slow chemical reactions (oxidation, curing, evaporation, etc.) and nonequilibrium phase transitions (crystallization and reorganization); it may even enable to separate the complicated simultaneous fusions, glass transitions and annealings, common in many macromolecules and complex mixtures (1, 2) Raspberries and blackberries belong to a diverse group of species and hybrids in the genus *Rubus*, therefore, it is highly likely that their phytochemical composition and associated bioactive properties may vary due to this genetic diversity (3). Recent study showed that black raspberry seed flour obtained from the cold-pressing procedure may contain a significant level of antioxidants (4). These data suggest the potential of developing novel uses of fruit seed flours as food ingredients rich in beneficial food factors for improving human diets. Additional research is required to investigate fruit seed flours for their contents of health beneficial factors to promote their value-added utilization as beneficial food ingredients. The present study was conducted to investigate the seed flours of red raspberry (*Rubus ideaus*) and blackberry *(Rubus fruticosus)* for their thermal characteristics and influence of water content on overlapping thermal events in the low temperature region by mean of Modulated Differential Calorimetry (MDSC).

Material and methods

Fruit seed flour preparation Fruit seed were the solid residues from the cold-pressing fruit pulp. Seeds were dried at room temperature, to the constant moisture of 6-7% and grinded immediately before thermal analysis.

Thermal analysis MDSC of blackberry and raspberry seed flours have been performed on TA Instruments DSC Q 1000, Differential Scanning Calorimeter and TGA measurements on TA Instruments TGA Q 500 Thermogravimetric Analyzer under N_2 purge flow of 50 ml/min and 60 ml/min respectively. MDSC scans were conducted in temperature range from -90^{0}C to 150^{0}C, with heating rate Hr = 5^{0}C/min with modulation of ±0.50 ^{0}C amplitude and 40 s period of modulation, and TGA scans were performed in temperature range of 25^{0}C to 700^{0}C with heating rate Hr = 5^{0}C/min.

Results and discussion

In Fig. 1 and 2 MDSC curves of blackberry and raspberry seed flours are presented. Complete DSC curve is characterized with overlapping effect in low-temperature region caused by the freezing and unfreezing of large-amplitude motion (5). It was shown (Fig. 3 and 4) that thermal transitions, observed in the range of −80 to −10^{0}C were independent on water content, as isothermal treatment of the samples on 90^{0}C/5 min, did not affect low temperature thermal transitions and they were mainly attributed to lipid melting transitions; Fig. 3 and 4 (6). Isothermal treatment at 90^{0}C/10 min affected transition at 93^{0}C. That broad endothermic peak with T_m at about 93^{0}C corresponds to water evaporation and protein denaturation (6). From TGA results it was shown that by isothermal tretment 90^{0}C/5 min sample water loss was about 6%.
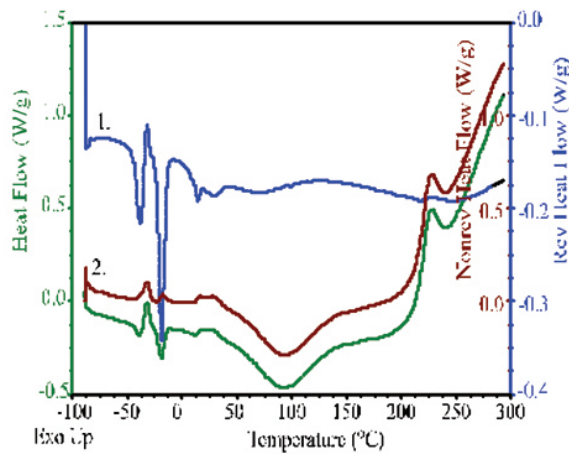
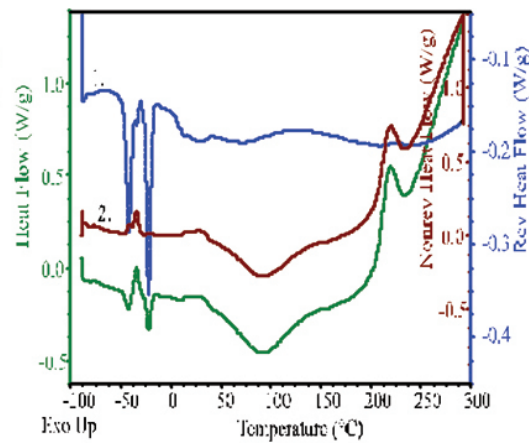**Figure 1.** MDSC curves of blackberry seed flour

Figure 2. MDSC curves of raspebrry seed flour

Using MDSC, the reversing (curve 1) and nonreversing (curve 2), thermal events in the low temperature region of seed flour have been approximately separated (4), reversing (curve 1), suggesting that there are two independent thermal processes.
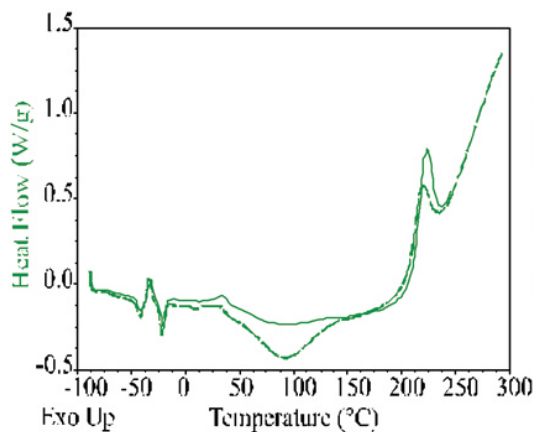

Figure 3. MDSC curves (total heat) of raspberry flour seed (dashed line) and isothermaly treated 900C/5 min (solid line)

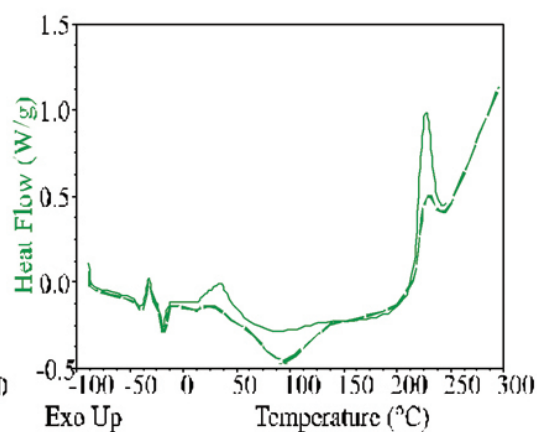**Figure 4.** MDSC curves (total heat) of blackberry flour seed (dashed line) and isothermaly treated 900C/5 min (solid line)

Section S6: Miscellanous

Results obtained from DSC and TGA curves indicated similarity in thermal behavior of raspberry and blackberry seed flour.

Conclusion

Using MDSC, thermal events in low temperature region (MDSC curve) of seed flour have been approximately separated (reversing curve 1), suggesting that there are two independent thermal processes. It was shown, by isothermal treatment of raspberry and balckberry seed flour that low temperature transitions are not affected by water content, and that broad endothermal transition at 93^0C corresponds to water evaporation and protein denaturation. Similarity of thermal behavior of blackberry and raspberry seed flours suggesting on composition resemblance.

Acknowledgements

76

References

1   B. Wunderlich, Y. Jin, A. Boller (1994) Thermochimica Acta, 283, 277-293.
2   Lai & Lii, 1999; TA Instruments, 1996
3   J.Parry, L. Su, J. Moore, Z. Cheng, M. Luther J.N.. Rao, J-Y Wang, L. L. YuJ. (2006), Agric. Food Chem. 54, 3773-3778.
4   M. Pyda, B. Wunderlich, (2005) Macromolecules, 38, 10472-10479
5   S. B. Matiacevich, M. L. Castelli´on, S. B. Maldonado, M. P. Buera Thermochimica Acta (2006), 448, 117–122.
6   L. Zhang, J. Li, S. Hogan, H. Chung, G. E. Welbaum, K. Zhou, (2010) Food Chemistry, 119, 592–599

THE RASPBERRY DRYING MATHEMATICAL MODEL

Lato Pezo[*]
Sanja Ostojić
Snežana Zlatanović
Aca Jovanović
Sanja Stanojlović,
Olgica Kovačević
Danijela Šuput

Institute of General and Physical Chemistry, University of Belgrade, Studentski Trg 12, 11000 Belgrade, Serbia

[*] *latopezo@yahoo.co.uk*

Abstract

The drying kinetics of raspberry in a laboratory dryer was studied. The logarithmic model was found to be the best model for describing the characteristics of raspberry, regarding correlation coefficient (r^2). The changes of color on raspberry's surface were determined by digital camera. A mathematical model to predict the shrinking of geometrical bodies was proposed, assuming unidirectional drying and two-dimensional shrinkage. The model was numerically solved by finite differences, taking into account a convective term in the mass balance equation, which appears as a consequence of non-unidirectional shrinkage. Thermal analysis, by means of differential scanning calorimetry (DSC) and thermogravimetry (TGA) of fresh and dried raspberries have been performed. DSC scans were conducted in temperature range from -90°C to 400°C, with heating rate Hr=5C°/min, and TGA scans were performed in temperature range of 25°C to 900°C with heating rate Hr=5C°/min. From results obtained differences in thermal stability of fresh and dried raspberries were shown.

Introduction

Mathematical modeling is widely used in developing kinetics models to predict the mass transfer of drying process at atmospheric pressure (1). The main objective of this study was to determine the effects of process parameters: drying air temperature, air velocity and sample surface on the diffusion model coefficients and the values of moisture diffusivity and heat transfer coefficients by using multiple regression analysis, and to test the most appropriate drying model for understanding the drying behavior of raspberry.

Material and methods

The raspberries (aver. diameter 11.4 mm, and aver. weight 2.9 g for single fruit), were carefully placed on the trays. The initial and final moisture contents of the products were determined at 105°C. Raspberries of average initial moisture content 85.7% (wb), were dried, at temperatures of 50°C, relative air humidity of 50-55%, at the velocities of drying air of 1.2 m/s. The kinetics models were selected regarding r^2 values to determine the quality of that fitting function (2). Color images of raspberries during drying process were captured in triplicate, by a common home camera. All the acquired images were 24 bit RGB (16.8 millions of colors). The macro function of the digital camera has been used, to cover a scene area of approximately Ø10 cm. The dimensions of raspberries were measured by a digital micrometer. The kinetics models were selected with the correlation coefficient (r^2), used to determine the quality of fitting functions. Analysis of variance (ANOVA) was performed using StatSoft Statistica, for Windows, ver. 10 program. The model was obtained for each dependent variable where factors were rejected when their significance level was less than 95%. Differential

scanning calorimetry (DSC) and thermo gravimetry (TGA) of fresh and dried raspberries have been performed under N_2 purge flow of 50ml/min and 60ml/min respectively. DSC scans were conducted in temperature range from -90°C to 400°C, with heating rate Hr=5C°/min, and TGA scans were performed in temperature range of 25°C to 900°C with heating rate Hr=5C°/min.

Results and discussion

The moisture content data at the given drying conditions and drying time were fitted, using thin-layer drying models of Newton-Lewis, Henderson and Pabis, logarithmic, Page, Wang and Singh evaluated based on coefficient of determination (r^2). The logarithmic model was found to be the best model for describing the characteristics of raspberry. The best model describing the thin layer-drying characteristic was chosen as the one with the highest r^2. It was determined that the best fitting results were obtained with logarithmic model, .
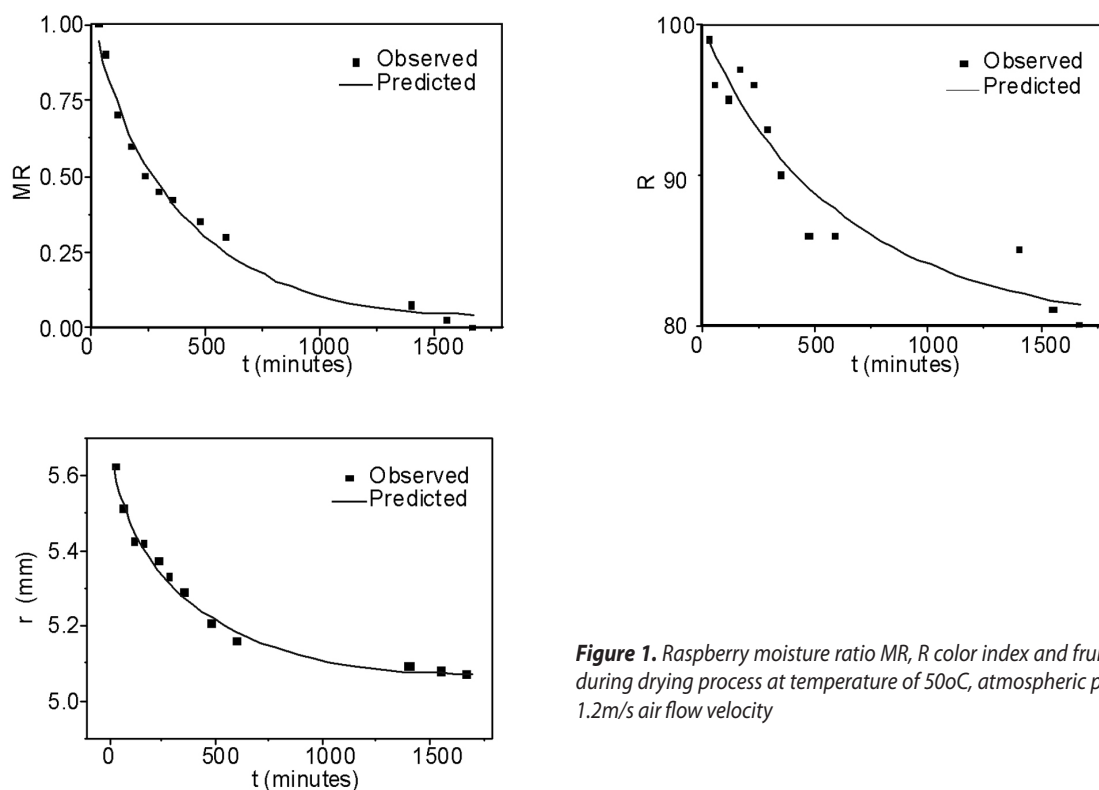
Figure 1. *Raspberry moisture ratio MR, R color index and fruit radius during drying process at temperature of 50oC, atmospheric pressure, 1.2m/s air flow velocity*

The best model describing the color changes characteristic was logarithmic model, . Calculated effective diffusion coefficient was 3.2E-10m^2/s, and activation energy 20 to 40 kJ/mol was in accordance to literature values (3). The obtained prediction results of fruit radius correspond very well to those achieved by experimental measurement. Pearson correlation coefficients and triplicate sample paired t-test on R (red) color index frequency were calculated during the experiment. The obtained results for prediction of fruit radius (4), corresponds very well to those achieved by experimental measurement. The moisture ratio (MR), as well as the R color index and overall fruit diameter changes during the drying experiment are presented in Fig. 1.

Obtained DSC and TGA curves of fresh and dried raspberries, (Fig 2.) show differences of thermal stability between fresh and dried fruits caused by water loss during drying process (5). It can be seen, from DSC curve that phase transition of ice melting and water evaporation are dominant thermal events, as the sample water content is high. High water content (85.7%) is also observed from corresponding TGA curve of fresh raspberries. DSC curve is characterized by three endothermal peaks with maximums at T_{m1}=-40.7°C, T_{m2}= -20.23 °C and T_{m3}=114.0°C respectively and one glass transition T_g= 42.3 °C. Results are in agreement with (5), which showed that glass transition temperatures of raspberries are influenced by water content, (6), as it was found that dried food material has similar thermal properties of semi-crystalline polymers. Water content of dried sample obtained from TGA curve, dashed curve was 19.3%.
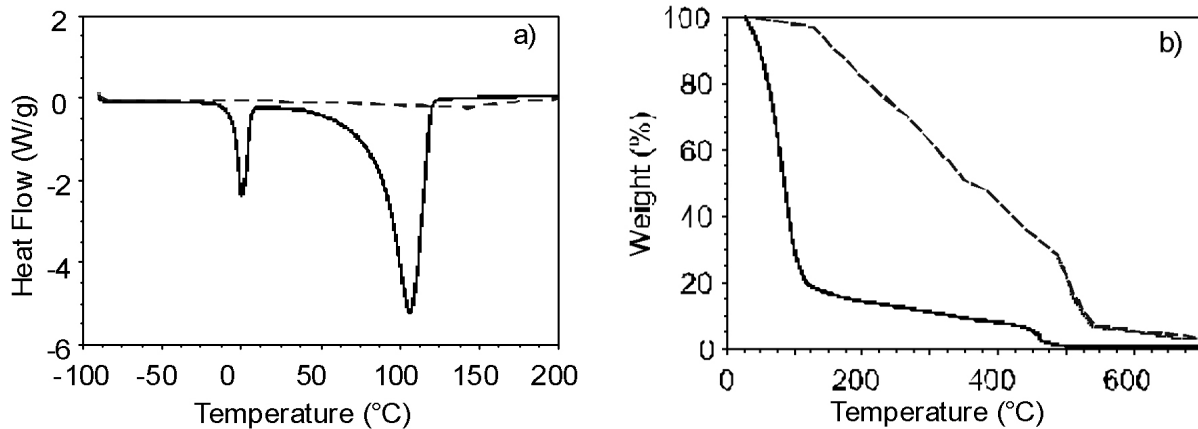
Figure 2. a) DSC curves of dried (dashed curve) and fresh (solid curve) raspberries and *b)* TGA curves of dried (dashed curve) and fresh (solid curve) raspberries

Conclusion

The best model adequately describes the drying behavior of raspberry fruit, with gained r^2 of 0.937. Statistical analysis, including comparison tests, showed that the model adequately represent the browning process, showing $r^2=0.958$. Finally, a mathematical model to predict the shrinking of geometrical spherical bodies was proposed, assuming unidirectional drying and two-dimensional shrinkage with accuracy of $r^2=0.934$. Thermal analysis shows differences of thermal stability between fresh and dried fruits caused by water loss during process of drying.

Acknowledgement

References

1. A.Kaya; O.Aydın; C. Demirtas, Biosystems Engineering, 2007, 96 (4), 517–524
2. E.K. Akpinar, Journal of Food Engineering, 2006, 73, 75–84
3. P. P. Lewicki; E. Jakubczyk, Journal of Food Engineering, 2004, 64, 307–314
4. P. E. Viollaz, C. O. Rovedo, Journal of Food Engineering, 2002, 52,149–153
5. R. M., Syamaladevi, S. S., Sablani, J. Tang, J. Powers, B. G. Swanson, Journal of Food Engineering, 2009, 91 460–467
6. S. Shyam, S.Roopesh, R. M. Syamaladevi, B. G. Swanson, Food Eng Rev, 2010, 168–203

THERMAL ANALYSIS OF FRESH AND OSMOTICALLY DEHYDRATED PORK MUSCLE PROTEINS

Sanja Ostojić[1]
Snežana Zlatanović[1]
Lato Pezo[1]
Darko Micić[1]
Danijela Šuput[2]
Branislav R. Simonović[1]
Ljubinko Lević[2]

[1] *Institute of General and Physical Chemistry, University of Belgrade Studentski trg 12, 11000 Belgrade, Serbia*

[2] *University of Novi Sad, Faculty of Technology, Bulevar Cara Lazara 1, 21000 Novi Sad, Serbia*

Abstract

The advantage of the DSC method is that it can be used in complex mixtures and at high concentrations of proteins, which is the situation occurring in muscle. Thermal stability of osmotically dehydrated pork meat have been compared to thermal behavior of fresh meat and post-dried pork meat. Water content of fresh, osmotically dehydrated and post dried meat has been obtained by TGA. As a consecvence of the water loss evident are differences in thermal behavior of meat (DSC). Results suggesting that destabilization of meat proteins and conformational changes have been induced by process of osmotic dehydratation, as enthalpy (ΔH) and temperature maximum (T_m) of protein denaturation of osmotically dehydrated meat decreased. Post-dried meat thermal behavior significaly differed from fresh and OD meat, with apparence of characteristic glass transition (T_g).

Introduction

A particular advantage of DSC technique is the possibility to examine proteins in the natural state and medium, as proteins need not be extracted or isolated (1).

A typical curve from thermal transitions found in a muscle is composed of three major transition zones. The first transition displays its maximum between 54ºC and 58ºC and has been attributed to myosin (2,3) the second transition, which occurs between 65ºC and 67ºC, was assigned to collagen (3.4) and to sarcoplasmic proteins (5). The third transition has been assigned to actin and is found between 80ºC and 83ºC (6). For the second transition it has also been shown that both isolated actomyosin and myosin and its sub-units undergo transitions in the same temperature range (5). Most of the water in muscle is held within the cell structures; inside myofibrils and inter-myofibrillar spaces, between myofibrils and cell membranes, between muscle cells and between bundles of muscle cells. It has been estimated that about 85% of the water in muscle cells is held within the myofibrils mainly by capillary forces arising from the arrangement of the thick and thin filaments within the myofibril. There are three types of water in muscle; each differing in the degree of its freedom. The bound water is that which strongly interacts with hydrophilic sites of proteins to form monolayers, and water that forms several additional layers around hydrophilic groups. This water has reduced mobility and is very resistant to freezing and being evaporated by heat. The bound water makes up less than 10% of the total water in muscle, and changes very little in post-rigor muscle. Another type of water found in muscle is called entrapped or immobilized water. These water molecules may be held either by steric effects and/or attraction to bound water. This water is held within the structure of the muscle but is not bound to proteins.

This work examines effects of water content on the fresh, osmotically dehydrated (OD) and post-dried meat protein thermal behavior.

80

Material and methods

Sample preparation Fresh pork (Musculus brachii) of normal pH (6.05) was bought in local butcher store and transported to the laboratory where it was held about 4°C for 1–2 h. The muscles were trimmed of external fat and connective tissues and manually cut into approximately 1x1x1 cm (1cm³) cubes.

Osmotic dehydration Meat samples were osmotically treated in solutions of sugar beet molasses (81.95 °Brix) at 22°C for 5 hours. Osmotically dehidrated meat have been post-dryed at room temperature to the moisture 3.4%.

Thermal anaysis DSC and TGA of fresh and osmotically dried and post-dryed pork meat have been performed on TA Instruments DSC Q 1000, differential scanning calorimeter and TGA measurements on TA Instruments TGA Q 500, thermogravimetric analyzer under N2 purge flow of 50ml/min and 60ml/min respectively. DSC scans were conducted in temperature range from 3°C to 150°C, and from -80°C to 180°C with heating rate Hr=5C°/min, and TGA scans were performed in temperature range of 25°C to 900°C with heating rate Hr=5C°/min.

Results and discussion

Thermal behavior of pork meat samples is shown in Figs 1, 2, 3 and 4 and in Table 1. Fig. 1 shows DSC curve of fresh pork meat with peaks at about -0.3°C, 69°C and 93°C, and total denaturation enthalpy of 970J/g.
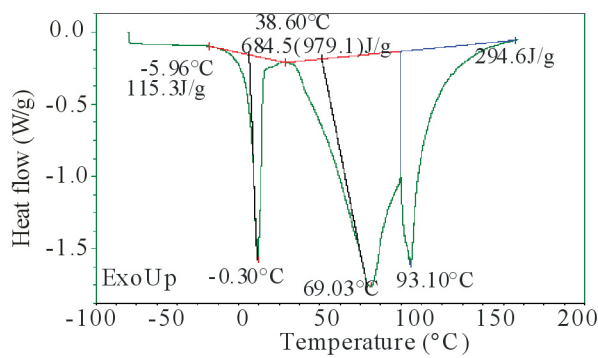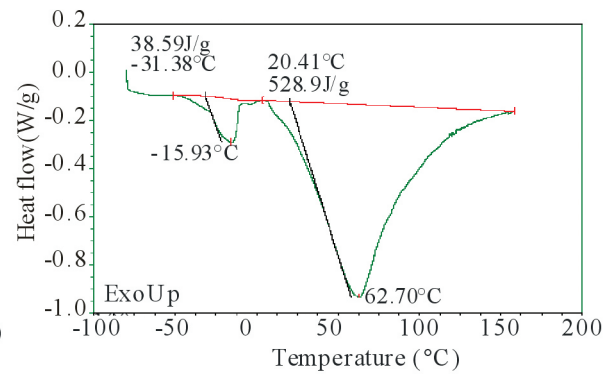
Figure 1. DSC curve of fresh pork meat

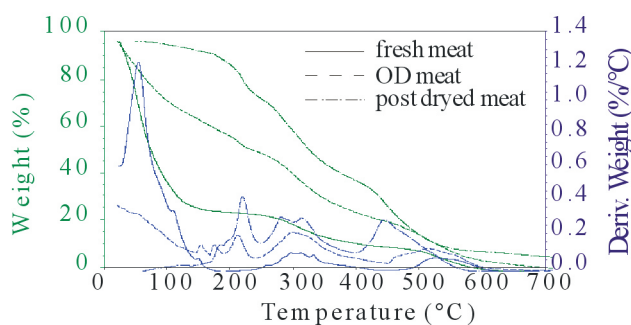*Figure 2.* DSC curve of OD meat

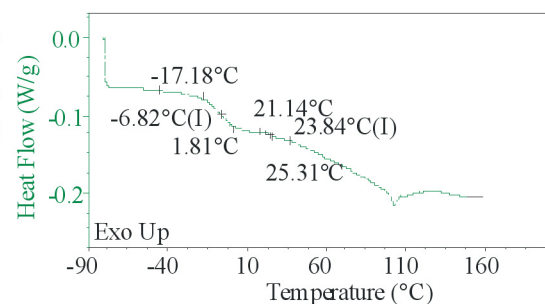*Figure 3.* TGA and dTGA curves of fresh and OD and post-dryed meat

Figure 4. DSC curve of post-dried OD meat at room temperature

First transition corresponds to water melting (T_m=-0.3°C), second transition, which occurs at 69°C, was assigned to collagen (6) and the third transition has been assigned to actin (5). In Fig. 2 DSC curve of osmotically dehydrated pork meat are presented, where first transition is water melting (T_m=-15.9 °C) and the process of protein denaturation is represented by one broad endothermal peak with temperature maximum T_m=57°C and total denaturation enthalpy (ΔH) of 430J/g. Unfrozen water (g/g solids) content for fresh and osmotically dehydrated meat obtained by method of Levine is 0.90g/g and 0.49g/g, respectively (6). In Fig. 3 are presented TGA curves of fresh, OD and post-dryed

osmotically dehydrated meat. Glass transition (T_g) at -6.8 ºC is evident (Fig. 4), as a consequence of low water content in the sample (6).

Sample	Onset temp. T_o(ºC)	Peak temp. T_m (ºC)	Enth ΔH (J/g)	Moisture (%)	Res. 700 ºC (%)	T_g (ºC)
OD meat	20.4	60.7	652.3	37.70	5.65	-
Post-dryed	-	-	-	3.77	7.59	6.8
Fresh meat	27.56	81.92	979.1	70.90	1.45	-

Table 1. *Thermodynamic parameters of protein transition for osmotically dried and fresh pork meat and temperature of glass transition (Tg) of post–dryed meat obtained from DSC Water content and residue at 700 ºC obtained from TGA curves.*

Conclusion

It was shown that sugar beet molasses solution affects thermal stability (DSC results), and water loss (TGA results) of dehydrated pork meat compared to fresh pork meat. As a result of water loss (TGA) post-dryed meat thermal behavior significaly differed from OD meat, with apparence of characteristic glas transition T_g

Acknowledgements

82

References

1. J. Tomaszewska-Gras, P. Konieczny (2010) Acta Sci. Pol., Technol. Aliment. 9(4), 413-423.
2. S. A. Anglea, V. Karathanos, M. Karel (1993), Biotechnol. Prog. 9, 204.
3. E. Stabursvik, H. Martens (1982). J. Texture Stud. 13, 291–309.
4. E. Stabursvik, H. Martens (1980). J. Sci. Food and Agric. 31, 1034–1042.
5. E. Tornberg (2005) Meat Sci. 70, 493–508.
6. M. S. Rahman, G. Al-Saidi, N. Guizani, A. Abdullah (2010)Thermochimica Acta. 509 111–119.

PORK MEAT OSMOTIC DEHYDRATION EFFICIENSY FOR DIFFERENT OSMOTIC SOLUTIONS

Lato L. Pezo[1]
Vladimir S. Filipović[2]
Milica R. Nićetin[2]
Biljana Lj. Ćurčić[2]
Nevena M. Mišljenović[2]
Gordana Koprivica[2]
Ljubinko B. Lević[2]

[1] Institute of General and Physical Chemistry, University of Belgrade Studentski trg 12-16, 11000 Belgrade, Serbia,

[2] University of Novi Sad, Faculty of Technology, 21000 Novi Sad, Bulevar cara Lazara 1, Serbia

Abstract

Pork meat (*M. triceps brachii*) was dehydrated in three different osmotic solutions (sugar beet molasses, ternary solution and combination of these solutions in a 1:1 ratio) under atmospheric pressure, at room temperature T (20ºC), with manual stirring on every 15 minutes, in order to analyze the efficiency of mass transfer kinetics during osmotic dehydration (OD). The most significant kinetic parameters observed were: water loss, solid gain, weight reduction, and also rate of water loss, rate of solid gain, rate of weight reduction and dehydration efficiency index. All parameters were determined after 1, 3 or 5 hours of treatment. Also, final dry matter content and water activity were measured. The optimum osmotic solution seems to be sugar beet molasses, and the dehydration conditions were determined by response surface method, by superimposing the contour plots of each process variable.

Introduction

Osmotic dehydration (OD), process is a well known method for preserving solid food, which involves partial water removal from food stuff immersed in hypertonic aqueous solutions. Due to low energy consumption and mild temperatures, which is considered minimal processing, OD is suitable as a pretreatment for many processes, to improve nutritional, sensorial and functional properties of food without changing its integrity (1). Mass transfer is induced by a difference in osmotic pressure: water outflow from product to solution, solute transfer from solution into the product, and leaching out of the products own solutes. Working temperature, concentration of osmotic solution and immersing time are the most important variables in osmotic process. Increasing the osmotic solution concentration induces an increase in the mass transfer. Great influence on the kinetics of water removal and solid gain has the type of osmotic agent. Ternary aqueous solutions containing salt and sugar are usually used as osmotic agents for meat dehydration. Research has shown that sugar beet molasses represents an excellent osmotic medium for dehydration process, primarily due to the high content of dry matter (80%), which provides high osmotic pressure in the solution as well as the specific chemical composition, characterized by high contents of vitamins, minerals, antioxidants and betain (3). Increasing the osmotic solution concentration induces an increase in the mass transfer.

Material and methods

Three different solutions were used as hypertonic mediums. Solution 1, ternary osmotic solution, was made from sucrose in the quantity of 1.200g/kg water, NaCl in the quantity of 350g/kg water and distilled water. Solution 2 was combination of the first and third in ratio 1:1. Solution 3, sugar beet molasses, with initial dry matter content of 80.00%, was obtained from the sugar factory Pećinci. The material to solution ratio was 1:5 (w/w). Samples from all three solutions after 1, 3 and 5 hours were

83

taken out to be lightly washed and gently blotted, to remove excess water. Dry matter content of the fresh and treated samples was determined by drying at 105°C for 24h in a heat chamber (Instrumentaria, Sutjeska) until constant weight. To follow mass transfer kinetics of the OD, three key process variables were measured: moisture content, change in weight and change in the soluble solids. Using these values, water loss (WL), weight reduction (WR), solid gain (SG), rate of water loss (RWL), rate of solid gain (RSG), rate of weight reduction (RWR) and dehydration efficiency index (EI) were calculated (2).

Analysis of variance (ANOVA) was performed using StatSoft Statistica, for Windows, ver. 10 program.

Results and discussion

The increase of immersion time during the process and/or the agitation resulted in increased DM. The highest DM obtained in Solution 2 after 5 hours of immersion was 60.08%, with agitation, while the highest value was achieved in solution 3 after five hours, without agitation (58.01%). ANOVA showed that there was no significant difference for DM, WL and WR between values of the OD meat in Solutions 1, 2 and 3, in contrast to DM for 1, 3 and 5 hours with or without agitation. The highest values of WR parameter were obtained after 5h in Solution 3 when process was performed with (0.39 g/g initial sample weigh-i.s.w.) and without agitation (0.33 g/g i.s.w.). The lowest SG after 5 hours of process was obtained in in solution 2 (0.26 g/g i.s.w.). When OD was performed with agitation, SG was slightly higher OD was without agitation (the lowest SG after five hours was 0.27 g/g i.s.w. for samples OD in solution 1). ANOVA showed that there was a significant difference between SG of the meat OD in Solutions 1, 2 and 3, and also of the meat samples dehydrated for 1, 3 and 5 hours. The amount of the solute penetration from the osmotic solution into the sample can be reduced by applying starch edible coatings (3). The highest WL values were noticed in samples dehydrated 5h in Solution 3 (with 0.52 g/g i.s.w. and without agitation 0.47 g/g i.s.w.). The highest EI (2.42) was achieved by using Solution 1, after 3h of the treatment performed with agitation. ANOVA showed that process time, type of osmotic solution and agitation has a significant influence on the EI of the meat samples. RWL and RSG were higher during the first hour of the process. The mass transfer rate was slightly more intensive when meat samples were immersed in solution 3, due to greater difference between the osmotic pressures of the hypertonic medium and the animal tissue. Higher values of the mass transfer rate were obtained when process was performed with agitation, due to already mentioned recovering of thick diffusion layer of water. In this way forming of concentration gradient in solution is avoided. Response surface method was used, introducing second order polynomials (SOP) to predict WL, SG, DM, and water activity (a_W). The optimum osmotic drying conditions for pork meat cubes, dehydrated in solution 1 are as follows: soaking time of 4 h, Solution 1 concentration and temperature of 72% and 45°C. According to SOP model, the optimum osmotic drying conditions for pork meat cubes, dehydrated in solution 2 should be: treatment time of 3 h, solution 2 concentration 57% w/w, and temperature of 40°C. Coordinates of optimized point in temperature, time and concentration graph, for solution 3,
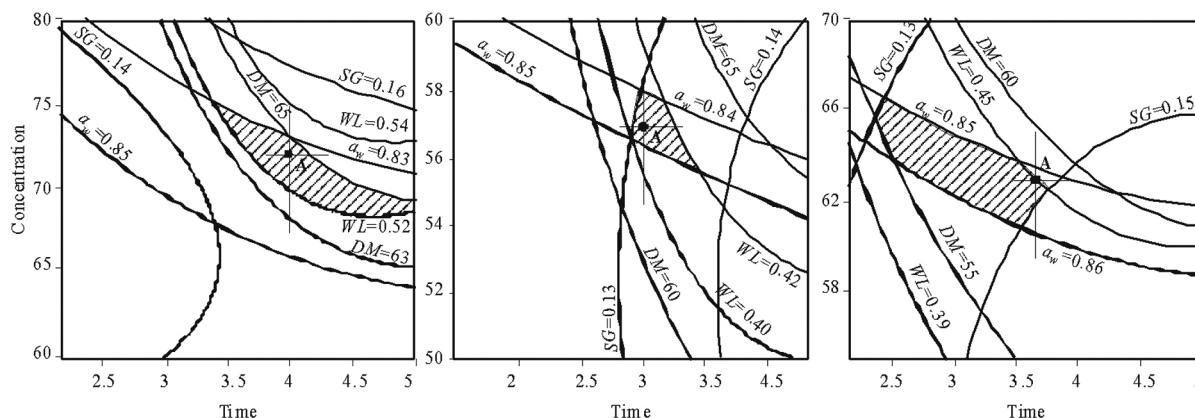

Figure 1. Optimum contour plots of the system responses for Solution 1, Solution 2, and Solution 3 (from left to right)

were: 40°C, 3.7 h and 63% w/w. The desired responses for the optimum drying conditions in solution 1 were: DM of 64.5%, WL in the close vicinity of 0.53, SG about 0.15 and aw in the range of 0.83 to 0.84. Water loss was much lesser for OD process in solution 2 and 3: 0.41 and 0.45. Other process parameters (SG and aw) were very similar, and alike to OD in solution 1, for solution 2 and 3, but DM were significantly smaller. DM for OD of pork meat in solution 2 was approximately 62%, and in solution 3 was about 58%, in contrast to 65% achieved using solution 1. The rate of mass reduction, the rate of water loss and the rate of solid gain were the highest during the first hour of the process. Higher values of the mass transfer rate were obtained when process was performed with agitation, due to already mentioned recovering of thick diffusion layer of water. In this way forming of concentration gradient in solution is avoided. Mass transfer rate decreased continuously from the first to the third hour, and after the third hour showed a tendency of slowing down.

Conclusion

According to presented results it can be concluded that all three solutions are satisfying osmotic mediums, especially when agitation was employed, due to better homogenization of osmotic medium. The best results regarding DM were achieved using Solutions 2 and 3. At the end of treatment SG were the lowest in samples immersed in Solutions 1 and 2. While, the best results considering WL, WR, and EI were achieved using solution 1, which is economy reasonable, considering that molasses is by-product of sugar industry. During OD of pork meat, in all three osmotic solutions, water removing process was most intensive at the beginning and after 3 hours had tendency of slowing down, and can be limited to 3 hours.

Acknowledgement

85

References

1. Silva, M. A. C. , Silva, Z. E., Mariani, V. C., Darche, S.(2012), Food Sci. Technol. 45, 246-252.
2. Koprivca, G., Mišljenović, N., Lević, Lj., Jevrić, L. (2010): Journal on Processing and Energy in Agriculture, 14, 27-31.
3. Mišljenović, N., Koprivica, G., Pezo, L., Kuljanin, T., Bodroža Solarov, M., Filipčev, B. (2011): APTEFF, 42, 91-100.

ARTIFICIAL NEURAL NETWORK MODEL FOR PORK MEAT OSMOTIC DEHYDRATATION PROCESS

Lato L. Pezo[1]
Biljana Lj. Ćurčić[2]
Milica R. Nićetin[2]
Vladimir S. Filipović[2]
Gordana B. Koprivica[2]
Nevena M. Mišljenović[2]
Danijela Šuput[2]

[1] *Institute of General and Physical Chemistry, University of Belgrade, Studentski trg 12-16, 11000 Belgrade, Serbia,*

[2] *University of Novi Sad, Faculty of Technology, 21000 Novi Sad, Bulevar cara Lazara 1, Serbia*

Abstract

Mass transfer of pork meat cubes *(M. triceps brachii),* shaped as 1x1x1 cm, during osmotic dehydration and under atmospheric pressure was investigated in this paper. The effects of different parameters, such as concentration of sugar beet molasses (60–80%, w/w), temperature (20–50ºC), and immersion time (1-5 hours) in terms of water loss (*WL*), solid gain (*SG*), final dry matter content *(DM)* and water activity *(a_W)* were investigated, using experimental results. An artificial neural network (ANN) model was developed for the prediction of *WL*, *SG*, *DM* and a_W in OD of pork meat cubes. These models were able to predict process outputs with r^2 of 0.952 for *SG* and r^2 0.980 for *WL*. The wide range of processing variables considered for the formulation of these models, and their easy implementation in a spreadsheet calculus make it very useful and practical for process design and control.

86

Introduction

Meat represents a cellular system with great biochemical and structural complexity, created by a network of muscular fibers surrounded by connective tissue. One of the most important constituent of meat is water (1, 2). Physicochemical, sensory and technological properties of fresh meat are related with water content. Water is held in myofibrils, functional proteins of meat, but also it may exist in the intracellular space between myofibrils and sarcoplasm (3). One of the potential preservation techniques for producing products with low water content and improved nutritional, sensorial and functional properties is osmotic dehydration (OD). In OD process, mass transfer is caused by a difference in osmotic pressure: water outflow from product to solution, solute transfer from solution into the product, and leaching out of the products own solutes (4). Sugar beet molasses is known as an excellent medium for OD, primarily due to the high dry matter (80%) and specific nutrient content. (4).

Materials and methods

Pork meat was purchased at the butcher shop "Mesara Štrand" in Novi Sad, just before use. Initial moisture content of the fresh meat was 72.83%. Sugar beet molasses solution, with inital dry matter content of 85.04%, was obtained from the sugar factory Pećinci. Distilled water was used for dilution of solutions. The sample to solution ratio was 1:5 (w/w). The process was performed in laboratory jars at solution different temperature with manual agitation on every 15 minutes. After OD, the samples were taken out from osmotic solutions to be lightly washed with water and gently blotted to remove excessive water. Dry matter content was determined by drying the material at 105 ºC in a heat chamber until constant mass was achived (Instrumentaria Sutjeska). a_W of the OD samples was measured using TESTO 650, with an accuracy of ±0.001 at 25ºC. Soluble solids content of the molasses

solutions was measured using Abbe refractometer, at 20ºC. In order to describe the mass transfer kinetics of the OD, experimental data from three key process variables are usually obtained: moisture content, change in weight and change in the soluble solids. Using these, WL, SG, were calculated for different solutions and processing times (4). The mean values of the experimentally measured process variables and desired outputs are given in Table 1. StatSoft Statistica ver. 10 was used, to randomly divide collected data into three groups: training data (60%), cross validation (20%) and testing data (20%). The cross-validation data set was used to test the performance of the network while training was in progress as an indicator of the level of generalization and the time at which the network has begun to over train. Coefficients associated with the hidden layer (both weights and biases) are grouped in matrices W_1 and B_1. Similarly, coefficients associated with the output layer are grouped in matrices W_2 and B_2. If Y is the matrix of the output variables, f_1 and f_2 are transfer functions in the hidden and output layers, respectively, and X is the matrix of input variables, it is possible to represent the neural network, by using matrix notation, as follows: $Y = f_1(W_2 \cdot f_2(W_1 \cdot X + B_1) + B_2)$

Results and discussion

Analysis for variance (ANOVA) was conducted for linear model of process variables, and response variables were tested against the impact of these variables. A significant effect $p<0.05$ of all variables, and r^2 for DM and WL were found to be very acceptable. All four variables considered in the ANOVA analysis, were used for the ANN modeling, in spite of the fact that some works have been carried out by changing one of these variables and finding some effect over WL or SG. The optimum number of hidden nodes was chosen upon minimizing the difference between predicted ANN values and desired outputs, using SOS (sum of squares) during testing as performance indicator. Results of WL, SG, a_W and DM during testing with five to nine PE (processing elements) in the hidden layer are presented in Table 1. Used MLPs (multi-layer perceptron models) are marked according to StatSoft Statistica's notation, MLP followed by number of inputs, number of neurons in the hidden layer, and the number of outputs. According to SCORE, from Table 1 (sum of r^2 for all variables in one ANN), it was noticed that the optimal number of neurons in the hidden layer is seven (network MLP 3-7-4), when obtaining high values of r^2 and also low values of SOS. Output variables are calculated by applying transfer functions f_1 and f_2 in the hidden and output layers, respectively, onto the matrix of input variables X. The algebraic system of equations is easily evaluated in a spreadsheet (i.e. Microsoft Excel) to predict WL, SG, a_W and DM of OD of pork meat cubes. The mean and the standard deviation of residuals have also been analyzed. The mean of residuals were in the range of 0.00-0.02 for WL; 0.00-0.01 for SG; 0.00 for a_W and 0.08-1.06 for DM, while standard deviation were in the range 0.02-0.04 for WL; 0.01-0.02 for SG; 0.01-0.02 for a_W, and 1.58-3.64 for DM. These results show a good approximation to a normal distribution around zero with a probability of 95% (2·SD) to find residuals below 0.04-0.08 for WL; 0.02-0.04 for SG; 0.02-0.04 for a_W, and 3-7.5 for DM, which means a good generalization ability of ANN model for the range of experimental values of WL, SG, a_W and DM. In order to assess the effect of each input variables changes, on the output variables a sensitivity analysis was performed. The white noise signals were incorporated by adding or subtracting a Gaussian error of SD=5% and zero mean with

No.	Network name	Hidden activation function	Output activation function	WL	SG	a_W	DM	SCORE
1	MLP 3-6-4	Identity	Logistic	0,988	0,956	0,891	0,960	3,795
2	MLP 3-7-4	Identity	Identity	0,991	0,963	0,942	0,988	3,884
3	MLP 3-5-4	Tanh	Exponential	0,989	0,940	0,915	0,983	3,827
4	MLP 3-5-4	Logistic	Identity	0,988	0,976	0,929	0,986	3,879
5	MLP 3-9-4	Logistic	Identity	0,916	0,865	0,829	0,920	3,530

Table 1. *Effect of the number of hidden nodes on r during testing*

Section S6: Miscellanous

98% probability, i.e. 2.576·SD to each input variable. Due to the large number of combinations (three variables in three levels) a full central composite experimental design (5) was used for testing the best performance developed ANN model, which seems to be MLP 3-7-4. The complete database (27 points) was used, for a total of 27x27=729 cases. *SOS* was calculated and compared with the base case which is comprised of the unperturbed points (i.e., without applying any noise). All output variables are most affected by processing time, while the impact of temperature and concentration were also notable.

Conclusion

ANN-based model was developed for prediction of *WL*, *SG*, a_w and *DM* of OD of pork meat cubes for a wide range of experimental conditions. Model was able to predict successfully experimental OD kinetics, with ease of implementing it for design and control of OD processes and also the effective use for predictive modeling and optimization of OD processes. As compared to multiple regression models, ANN models yield a better fit of experimental data.

Acknowledgement

88

References

1. Castro-Giraldez, M., Fito, P. (2010), J.Food Eng., 99, 24-30.
2. Puolanne, E., Halonen, M. (2010), Meat Sci., 86, 151-165.
3. Barat, J., Alino, M., Fuentes, A., Grau, R., Romero, J. B. (2009), J.Food Eng., 93, 108-113.
4. Koprivca, G., Mišljenović, N., Lević, Lj., Jevrić, L. (2010), Journal on Processing and Energy in Agriculture, 14, 27-31.
5. Box G.E.P. and Behnken D.W. (1960), Technometrics, 2, 455–475.

ANTIMICROBIAL PROPERTIES OF MUSHROOM JUICE

Mladen Simonović
Aleksandra Radulović
Miroslava Dojčinović
Sava Hranisavljević
Branislav Simonović

Institute of general and physical chemistry, University of Belgrade, Studentski trg 12-16, 11000 Belgrade, Serbia

Abstract

The antibacterial activity in some kinds of mushrooms is thought to be due to the high content of beta-glucans. The aim of this work was to obtain the shiitake mushroom juice and to show its long stability due to absence of microorganisms. The basic separation operation was just freezing and unfreezing at room temperature, with complete absence of heating, whereby a large quantity of native juice was formed and separated from pulp using filter press and centrifuge. The identification of characteristic groups for beta-glucans was done with FT-IR. Both the native juice and the pulp had a high content of antimicrobial components, which was confirmed by standard microbiological analysis. On agar plates with shiitake juice and pulp respectively, the absence of bacteria *Salmonellae, Coagulase positive staphylococcae, Sulphite reducing clostridia, Proteus specia* and *Escherichia coli* was confirmed. Further, there was no need to pasteurize or sterilize them to obtain a final product. As the microbiological stability of these products has been confirmed, they could be applied as a dietary product or a functional food component.

Introduction

The immunomodulatory, anticancer [1] and antibacterial activity in some kinds of mushrooms are thought to be due to the high content of beta-glucans. Among the most studied mushroom beta-glucans is lentinan from Shiitake (*lentinus edodes*). In the numerous studies it was demonstrated that lentinan has not only the mentioned functions, but also the cholesterol and lipid-lowering as well as glucose-regulatory activity. Due to its anti carcinogenic [2] activity, lentinan is approved in Japan for clinical use in the patients with gastric [3] and colorectal cancers [4]. Further, lentinan was shown to have antibacterial substances against *Streptococcus spp*. and *Actinomyces spp*. They were less effective against *Enterococcus spp*. and *Staphylococcus spp*. Diverse compounds of shiitake have been shown to have cardio protective effects. Dietary shiitake lower plasma-free cholesterol and inhibit platelet aggregation. Finally, an anticaries effect of shiitake was demonstrated [5]. There were no reports of over dosage of any of the shiitake products, which are normally available in Japan. Dietary supplements containing extracts of mushrooms (e.g. shiitake) are available and are underlined to have significant beta-glucan content.

Material and methods

The shiitake mushrooms used in this work were bought in the local market in Belgrade, Serbia. First, the mushrooms were cleaned and washed, after what they were spontaneously frozen and unfrozen. Then, the separation of native juice from pulp followed using filter press or centrifuge. The filtered native juice and the separated pulp were regarded as the final product (stable without temperature treatment). The obtained shiitake juice and shiitake pulp were brought to a standard microbiological analysis on agar plates. They were also analyzed with FT-IR to detect characteristic functional groups. FT-IR spectra were recorded on MIDAC FT-IR M4000, Midac, USA.
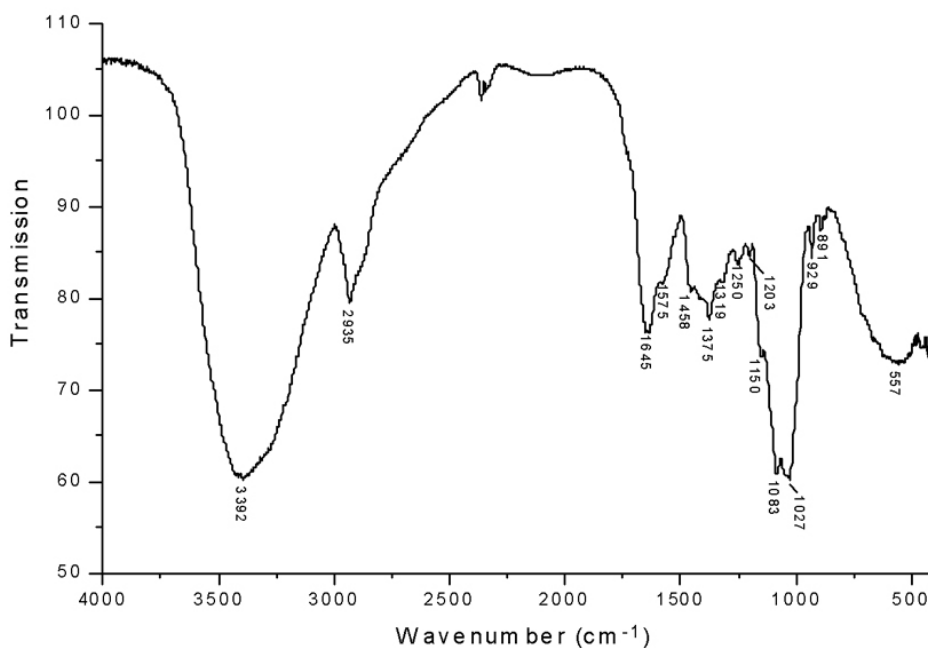
Results and discussion

Figure 1. *FT-IR spectrum of shiitake-juice*

In the FT-IR spectrum both of pulp and juice, the bands corresponding to polysaccharide functional groups were detected. The position of the O-H stretching occurred as a broad peak at 3200-3500 cm^{-1}. The strong peak at 2800-3000 cm^{-1} came from C-H stretching. The carbonyl stretching was at 1600-1680 cm^{-1}. The bands at approx. 900 cm^{-1} showed C-O-C stretching of D-glucopyranose rings.

Also, some peaks have been detected coming from the sulphurous compounds which gave a characteristic smell. The peak at 1083 came form the C=S groups and the peak at 1027 correlated with S=O groups.

The results of microbiological analysis are shown in the tables.

Microorganisms	Measured value	Referent value
Salmonellae in 25 g	Not found	0
Coagulase positive staphylococcae in 0,1 g	Not found	0
Sulphite reducing clostridia in 0,1 g	Not found	0
Proteus specia in 0,1 g	Not found	0
Escherichia coli in 0,1 g	Not found	0
Yeasts in 1,0 g	0	< 500
Number of microorganisms in 1,0 g	1000	< 50.000
Other microorganisms	Saprophytic coccae Bacillus sp.	/

Table 1. *The results of microbiological analysis of shiitake juice*

Table 2. The results of microbiological analysis of shiitake pulp

The analyzed probes are in accordance with paragraph 4 and 32 of the directive Of. Gazeta FRY Nr. 26/93 and can be used as dietary supplements.

The native juice can be further concentrated at low temperature regime for the purpose of obtaining some dietary products, supplements and a component of functional food. The separated pulp could further be dried and also applied as a dietary product as a functional food component (e.g. as food additive in diverse meals).

References

1. P. Kidd. 2000, Altern Med rev, 5: 4-27.
2. A. Ladanyi, J. Timar, K. Lapis. 1993, Cancer Immunol Immunother, 36: 123-126.
3. H. Nakano, K. Namatame, H. Nemoto et al. 1999, Hepatogastroenterology, 46: 2662-2668.
4. T. Mitamura, S. Sakamoto, S. Suzuki et al. 2000, Oncol rep, 7: 559-601.
5. N. Shouji, K. Takada, K. Fukushima, M. Hirasawa. 2000, Caries res, 34: 94-98.

Authors Index

S

Savić A.G. 14, 57, 60
Savic D. 20, 30
Simić-Krstić J.B. 8, 51
Simonović B.R. 17, 72, 74, 80, 89
Simonović M. 17, 72, 74, 89
Spasić S.Z. 57, 60
Spasojević I. 42
Stanić M. 26, 33, 42
Stanojlović S. 77
Stojiljkovic M. 20, 30

Š

Šentjurc M. 36, 48
Šetrajčić I.J. 5
Šetrajčić J.P. 5
Štrancar J. 36, 48
Šuput D. 77, 80, 86

T

Todorović N. 26, 30

V

Vasiljević-Radović D. 45
Veranič P. 66
Vučinić Ž. 26

Z

Zakrzewska J. 33, 42
Zeisig R. 48
Zlatanović S. 77, 80
Zorec R. 66
Zupančič G. 63

Ž

Živić M. 26, 30, 33, 42
Živković S. 39
Žižić M. 26, 33, 42

Regional Biophysics Conference 2012
Kladovo-Belgrade, Serbia
September 03-07, 2012

Relax-**Be** snooping-**Carpe diem**